

NAVAL POSTGRADUATE SCHOOL MONTEREY, CALIFORNIA



THESIS

**THE EFFECT OF VARYING THE MnO
CONTENT OF THE FLUX USED FOR THE
SUBMERGED ARC WELDING OF NAVY
HY-100 STEEL**

by

Allen L. Clark

December, 1995

Thesis Advisor:

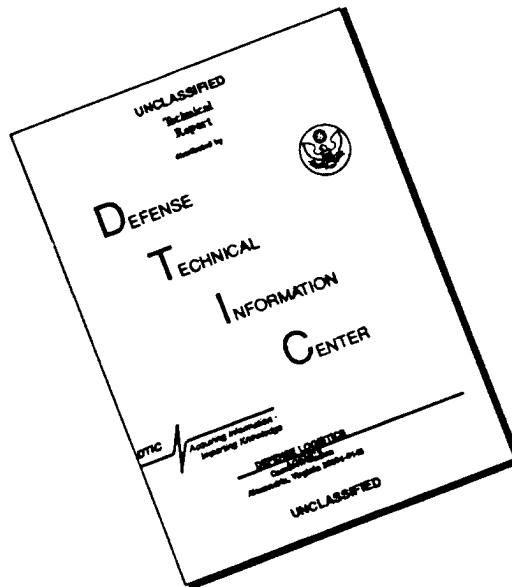
Alan G. Fox

Approved for public release; distribution is unlimited.

19960520 031

DTIC QUALITY INSPECTED 1

DISCLAIMER NOTICE



THIS DOCUMENT IS BEST QUALITY AVAILABLE. THE COPY FURNISHED TO DTIC CONTAINED A SIGNIFICANT NUMBER OF PAGES WHICH DO NOT REPRODUCE LEGIBLY.

REPORT DOCUMENTATION PAGE			Form Approved OMB No. 0704-0188	
Public reporting burden for this collection of information is estimated to average 1 hour per response, including the time for reviewing instruction, searching existing data sources, gathering and maintaining the data needed, and completing and reviewing the collection of information. Send comments regarding this burden estimate or any other aspect of this collection of information, including suggestions for reducing this burden, to Washington Headquarters Services, Directorate for Information Operations and Reports, 1215 Jefferson Davis Highway, Suite 1204, Arlington, VA 22202-4302, and to the Office of Management and Budget, Paperwork Reduction Project (0704-0188) Washington DC 20503.				
1. AGENCY USE ONLY (Leave blank)	2. REPORT DATE December 1995	3. REPORT TYPE AND DATES COVERED Master's Thesis		
4. TITLE AND SUBTITLE THE EFFECT OF VARYING THE MnO CONTENT OF THE FLUX USED FOR THE SUBMERGED ARC WELDING OF NAVY HY-100 STEEL		5. FUNDING NUMBERS		
6. AUTHOR(S) Clark, Allen L.				
7. PERFORMING ORGANIZATION NAME(S) AND ADDRESS(ES) Naval Postgraduate School Monterey CA 93943-5000		8. PERFORMING ORGANIZATION REPORT NUMBER		
9. SPONSORING/MONITORING AGENCY NAME(S) AND ADDRESS(ES)		10. SPONSORING/MONITORING AGENCY REPORT NUMBER		
11. SUPPLEMENTARY NOTES The views expressed in this thesis are those of the author and do not reflect the official policy or position of the Department of Defense or the U.S. Government.				
12a. DISTRIBUTION/AVAILABILITY STATEMENT Approved for public release; distribution is unlimited.			12b. DISTRIBUTION CODE	
13. ABSTRACT (maximum 200 words) Weld metal strength and toughness are determined by its microstructure, which is in turn determined by the concentration of various alloying elements and impurities as well as the welding thermal cycle. This study investigated the effects of systematically varying the manganese oxide content in the flux used for HY-100 submerged arc welds. A trial addition of cerium oxide was also performed. Specimens were compared using mechanical properties, weld metal chemistry, inclusion chemistry, and microstructural analysis. It was found that cerium oxide addition and the correct amount of manganese oxide resulted in improved toughness. These improved properties were determined to arise from a low proportion of bainite in the fully reaustenitized region of the weld metal HAZ in these multipass welds. In the MnO series welds, the bainite is replaced by a fine low carbon martensite due to the increased weld metal hardenability. In the CeO ₂ weld it is replaced by acicular ferrite due to the lowering of the austenite grain boundary energy by the cerium. The production of a series of welds with different manganese contents also resulted in the extension of existing theories of weld metal deoxidation.				
14. SUBJECT TERMS HY-100 steel, submerged arc welding, non-metallic inclusions, acicular ferrite, weld metal deoxidation.			15. NUMBER OF PAGES 167	
			16. PRICE CODE	
17. SECURITY CLASSIFICATION OF REPORT Unclassified	18. SECURITY CLASSIFICATION OF THIS PAGE Unclassified	19. SECURITY CLASSIFICATION OF ABSTRACT Unclassified	20. LIMITATION OF ABSTRACT UL	

Approved for public release; distribution is unlimited.

**THE EFFECT OF VARYING THE MnO CONTENT OF THE FLUX USED
FOR THE SUBMERGED ARC WELDING OF NAVY
HY-100 STEEL**

Allen L. Clark
Lieutenant, United States Navy
B.S., Pennsylvania State University, 1986

Submitted in partial fulfillment
of the requirements for the degree of

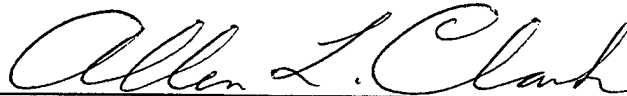
MASTER OF SCIENCE IN MECHANICAL ENGINEERING

from the

NAVAL POSTGRADUATE SCHOOL

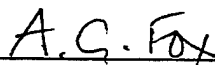
December 1995

Author:

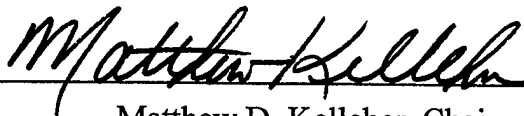


Allen L. Clark

Approved by:



Alan G. Fox, Thesis Advisor



Matthew D. Kelleher, Chairman
Department of Mechanical Engineering

ABSTRACT

Weld metal strength and toughness are determined by its microstructure, which is in turn determined by the concentration of various alloying elements and impurities as well as the welding thermal cycle. This study investigated the effects of systematically varying the manganese oxide content in the flux used for HY-100 submerged arc welds. A trial addition of cerium oxide was also performed. Specimens were compared using mechanical properties, weld metal chemistry, inclusion chemistry, and microstructural analysis. It was found that cerium oxide addition and the correct amount of manganese oxide resulted in improved toughness. These improved properties were determined to arise from a low proportion of bainite in the fully reaustenitized region of the weld metal HAZ in these multipass welds. In the MnO series welds, the bainite is replaced by a fine low carbon martensite due to the increased weld metal hardenability. In the CeO₂ weld it is replaced by acicular ferrite due to the lowering of the austenite grain boundary energy by the cerium. The production of a series of welds with different manganese contents also resulted in the extension of existing theories of weld metal deoxidation.

TABLE OF CONTENTS

I. INTRODUCTION	1
II. BACKGROUND	3
A. HY-100 STEEL	3
B. THE SUBMERGED ARC WELDING (SAW) PROCESS	4
C. INCLUSION FORMATION IN THE WELD POOL	6
D. WELD POOL SOLIDIFICATION AND THE δ -FERRITE TO AUSTENITE TRANSFORMATION	8
E. TRANSFORMATIONS ON COOLING AUSTENITE TO ROOM TEMPERATURE	10
1. Grain Boundary (Allotriomorphic) Ferrite	11
2. Side Plate (Widmanstätten) Ferrite	11
3. Bainite	11
4. Acicular Ferrite	12
5. Martensite	12
F. ACICULAR FERRITE NUCLEATION	14
G. MULTI-PASS EFFECTS	17
H. SUMMARY	18

III.	EXPERIMENTAL PROCEDURES AND RESULTS	27
A.	SAMPLE PRODUCTION	27
1.	Flux Preparation	27
2.	Welding Parameters	28
B.	WELD METAL CHEMISTRY	29
C.	MECHANICAL TESTING	29
D.	SCANNING ELECTRON MICROSCOPY	29
E.	OPTICAL MICROSCOPY	31
F.	MICROHARDNESS MEASUREMENTS	33
G.	INCLUSION CHEMISTRY	33
IV.	DISCUSSION	89
A.	WELD METAL CHEMISTRY	89
B.	INCLUSION CHEMISTRY	91
C.	INCLUSION SIZE AND DISTRIBUTION	96
D.	MICROSTRUCTURES	98
1.	Weld Acicular Ferrite	98
2.	Individual Areas	100
E.	MECHANICAL PROPERTIES	101
1.	Relationships Between Mechanical Properties	101

2.	Mechanical Property - Microstructure Relationships	103
3.	Mechanical Property - Chemistry Relationships	103
F.	CERIUM OXIDE ADDITION	105
G.	SUMMARY OF RELATIONSHIPS	106
1.	Weld Metal Deoxidation	106
2.	Microstructure and Mechanical Properties	107
V.	SUMMARY	135
A.	CONCLUSIONS	135
B.	RECOMMENDATIONS	136
	LIST OF REFERENCES	139
	INITIAL DISTRIBUTION LIST	145

LIST OF TABLES

2-1. HY-100 and HY-100 SAW Filler Wire	
Required and Actual Chemical Compositions	20
2-2. HY-100 Plate and Submerged Arc Weld	
Mechanical Property Specifications (Partial)	21
3-1. "Best Guess" Flux Chemistries in Weight Percent.	36
3-2. Welding Parameters	37
3-3. Weld Metal Chemistry in Weight Percent.	38
3-4. Average Mechanical Test Results.	39
3-5. Inclusion Statistics Summary.	40
3-6. Quantitative Optical Microscopy Results (%).	41
3-7. Vickers Microhardness Test Results.	42
3-8. F292 (Commercial Flux) Inclusion Chemistry	43
3-9. F326 (Base) Inclusion Chemistry.	44
3-10. F327 (1% MnO) Inclusion Chemistry.	45
3-11. F328 (2% MnO) Inclusion Chemistry.	46
3-12. F329 (3% MnO) Inclusion Chemistry.	47
3-13. F330 (0.5% CeO ₂) Inclusion Chemistry.	48

4-1. IIW Equation and Calculated Hardenabilities.	109
4-2. Areas Under the Impact Energy Curves (N•m•°C) by Trapezoidal Rule.	109

LIST OF FIGURES

2-1. The Submerged Arc Welding Process	22
2-2. Schematic diagram of Layered Structure of Inclusions Due to Sequential Oxidation Reactions	23
2-3. A CCT Curve Similar to That of HY-100, Except it Shows No Martensite Region	24
2-4. CCT Curve Variation With Region of the Weld	25
3-1. Charpy Impact Test Results.	49
3-2. Fracture Appearance Test Results.	50
3-3. Sample F292 Inclusion Distribution.	51
3-4. Sample F326 Inclusion Distribution.	52
3-5. Sample F327 Inclusion Distribution.	53
3-6. Sample F328 Inclusion Distribution.	54
3-7. Sample F329 Inclusion Distribution.	55
3-8. Sample F330 Inclusion Distribution.	56
3-9. F292 SEM Microstructure.	57
3-10. F292 SEM Microstructure	58
3-11. F328 SEM Microstructure.	59

3-12. F328 SEM Microstructure.	60
3-13. Representative F292 Microstructure for Acicular Ferrite Count.	61
3-14. Representative F326 Microstructure for Acicular Ferrite Count.	61
3-15. Representative F327 Microstructure for Acicular Ferrite Count.	62
3-16. Representative F328 Microstructure for Acicular Ferrite Count.	62
3-17. Representative F329 Microstructure for Acicular Ferrite Count.	63
3-18. Representative F330 Microstructure for Acicular Ferrite Count.	63
3-19. Baseplate Microstructure.	64
3-20. F292 Last Pass Microstructure.	65
3-21. F326 Last Pass Microstructure.	66
3-22. F327 Last Pass Microstructure.	67
3-23. F328 Last Pass Microstructure.	68
3-24. F329 Last Pass Microstructure.	69
3-25. F330 Last Pass Microstructure.	70
3-26. F292 Weld Metal Coarse HAZ Microstructure.	71
3-27. F326 Weld Metal Coarse HAZ Microstructure.	72
3-28. F327 Weld Metal Coarse HAZ Microstructure.	73
3-29. F328 Weld Metal Coarse HAZ Microstructure.	74
3-30. F329 Weld Metal Coarse HAZ Microstructure.	75
3-31. F330 Weld Metal Coarse HAZ Microstructure.	76

3-32. F292 Prior Pass Reheated Microstructure.	77
3-33. F326 Prior Pass Reheated Microstructure.	78
3-34. F327 Prior Pass Reheated Microstructure.	79
3-35. F328 Prior Pass Reheated Microstructure.	80
3-36. F329 Prior Pass Reheated Microstructure.	81
3-37. F330 Prior Pass Reheated Microstructure.	82
3-38. F292 Typical HAZ Macrograph.	83
3-39. F326 Typical HAZ Macrograph.	83
3-40. F327 Typical HAZ Macrograph.	84
3-41. F328 Typical HAZ Macrograph.	84
3-42. F329 Typical HAZ Macrograph.	85
3-43. F330 Typical HAZ Macrograph.	85
3-44. F328 Martensitic Region Macrograph.	86
3-45. A Typical Inclusion and Its Diffraction Pattern.	87
4-1. Weld Metal Mn vs. Flux MnO.	110
4-2. Weld Metal Mn vs. Added MnO.	110
4-3. Weld Metal Al vs. Added MnO.	111
4-4. Weld Metal Si vs. Added MnO.	111
4-5. Weld Metal C vs. Added MnO.	112
4-6. Weld Metal O vs. Added MnO.	112

4-7. Grong's Plot of Oxygen Content vs. Deoxidation Parameter.	113
4-8. Inclusion Mn vs. Added MnO.	114
4-9. Inclusion MnO vs. Added MnO.	114
4-10. Inclusion Mn vs. Weld Mn.	115
4-11. Inclusion MnO vs. Weld Mn.	115
4-12. Inclusion Al vs. Added MnO.	116
4-13. Inclusion Al_2O_3 vs. Added MnO.	116
4-14. Inclusion Si vs. Added MnO.	117
4-15. Inclusion SiO_2 vs. Added MnO.	117
4-16. Inclusion Ti vs. Added MnO.	118
4-17. Inclusion Mg vs. Added MnO.	118
4-18. Inclusion Cr vs. Added MnO.	119
4-19. Inclusion Zr vs. Added MnO.	119
4-20. Inclusion Size vs. Added MnO.	120
4-21. Inclusion Volume Percent vs. Added MnO.	120
4-22. Inclusion Count vs. Added MnO.	121
4-23. Inclusion Size vs. Flux MnO.	121
4-24. Volume Percent Inclusions vs. Flux MnO.	122
4-25. Inclusion Count vs. Flux MnO.	122
4-26. Weld Acicular Ferrite vs. Added MnO.	123

4-27. Weld Acicular Ferrite vs. Weld Metal O ₂	123
4-28. Weld Acicular Ferrite vs. Inclusion Size.	124
4-29. Weld Acicular Ferrite vs. Volume Percent Inclusions.	124
4-30. Weld Acicular Ferrite vs. Inclusion Count.	125
4-31. Last Pass Acicular Ferrite vs. Weld Acicular Ferrite.	125
4-32. Martensite in Coarse HAZ vs. Hardenability.	126
4-33. Last Pass Hardness vs. Yield Strength.	126
4-34. Coarse HAZ Hardness vs. Yield Strength.	127
4-35. Prior Pass Hardness vs. Yield Strength.	127
4-36. Impact Area vs. Yield Strength.	128
4-37. Weld Acicular Ferrite vs. Yield Strength.	128
4-38. Weld Acicular Ferrite vs. Impact Area.	129
4-39. Inclusion Size vs. Impact Area.	129
4-40. Inclusion Count vs. Impact Area.	130
4-41. Volume Percent Inclusions vs. Impact Area.	130
4-42. Average Microhardness vs. Martensite in Coarse HAZ.	131
4-43. Impact Area vs. Martensite in Coarse HAZ.	131
4-44. Yield Strength vs. Added MnO.	132
4-45. Hardenability vs. Added MnO.	132
4-46. Yield Strength vs. Hardenability.	133

4-47. Impact Area vs. Hardenability.	133
4-48. Position on Ternary Phase Diagram For Inclusions Analyzed at NPS.	134

ACKNOWLEDGEMENT

Many people provided support and advice that culminated in this research effort. I am especially appreciative of my parents, who instilled in me the love of science; Mr. Ron Varner, who gave me his love for chemistry; Professor Fox, for lending me his enthusiasm and knowledge in this effort; my friends, for their patience when I was frustrated; and the parishoners of St. Thomas Aquinas, for their love and prayers. Mr. Rich Hashimoto and Dr. Sarath Menon deserve special recognition for their assistance in the laboratory.

I. INTRODUCTION

In most military applications, if one does not have the best people and the best equipment, success is questionable. This is especially true in today's environment where we can no longer afford to overwhelm potential adversaries with large numbers of tanks, aircraft, ships, and submarines. The necessity of having the best has driven the U.S. Navy to develop steels with ever higher strength to weight ratios, resulting in higher speed ships for the same strength (or higher strength for the same speed).

The quest for higher strength steels for Naval construction has led to the development of complex alloy steels which rely on both alloying and heat treatment to achieve the required strength. Unfortunately, the process of joining pieces of these complex steels together by melting them together (welding) overrides the previous heat treatment, destroying the mechanical properties. Welding metallurgy is the science which allows an understanding of the factors which affect the weld metal microstructure, and leads to controlling them to achieve strength and toughness consistent with base plate design.

Currently, the primary high strength steel in use for U.S. Navy construction is HY-100. Although it will soon be superseded by HSLA-100 primarily due to reduced welding costs, HY-100 welding research is important for three reasons: the commercial use of the steel, the knowledge gained can be applied to the welding of other steels, and for U.S. Navy repair welding over the next thirty years. Submerged arc welding (SAW) was

employed in the present work because it is a common industrial practice easily repeatable in the laboratory. It is also the automated process most similar to manual shielded metal arc welding (SMAW, a.k.a. stick welding), the most common form of repair welding. SMAW itself was not studied because only highly trained (and hence highly paid) welders can produce consistent laboratory results.

Weld metal mechanical properties depend on the microstructures present, which in turn depend on welding thermal cycle, alloying elements, and impurities in the form of non-metallic inclusions and dissolved gases. Prior research in HY-100 steel welds at the Naval Postgraduate School [Refs.1-5] has focused on comparing the influence of commercially available fluxes on the non-metallic inclusions and hence the microconstituents, particularly acicular ferrite, in the weld metal. In this study, flux composition was systematically varied by adding manganese oxide (MnO) to a base flux with the goal of identifying trends specific to this component of the flux in the hope of developing a superior flux to that currently in use. In addition, one sample was prepared by adding cerium oxide (CeO_2) to the base flux in the hope that it would improve the toughness in HY-100 welds as it has with other alloys.

II. BACKGROUND

A. HY-100 STEEL

High Yield (HY) steels were developed from pre-World War I German armor plate steels as a substitute for the U.S. Navy's high tensile strength (HTS) steels in use through World War II. The Navy has employed HY-80, HY-100, and HY-130 successfully, where the number designation refers to the minimum yield strength in thousands of pounds per square inch (ksi). Cracking problems during early HY-80 welds on submarines led to tight controls over electrode storage and use, preheat and interpass temperatures, heat input, joint design, welder training, and nondestructive testing. These controls are responsible for the high cost of welding HY steels, and are leading to their replacement by the high strength low alloy (HSLA) steels. [Ref. 6]

HY-100 steel is a quenched and tempered martensitic steel, which derives its mechanical properties from alloying with nickel, chromium, molybdenum, vanadium, and carbon as well as thermal treatment. It is austenitized at 843-899 °C, quenched in water to yield not less than 80% martensite throughout the thickness (the remainder is bainite), then tempered near 621-677°C (minimum 566 °C) and quenched in water again. The required alloy chemical composition for plate HY-100 per. MIL-S-16216 is given in Table 2-1. A partial list of required mechanical properties are specified in Table 2-2. [Refs. 7 and 8]

B. THE SUBMERGED ARC WELDING (SAW) PROCESS

Submerged arc welding is an automated process most often used in the horizontal position. A granular flux is poured over the joint ahead of the consumable electrode, submerging the two base and single backing plate sections to be joined as well as the electrode. Current is passed from the electrode (electrode positive) into the base plate, melting the electrode (filler wire) and some of the base plate and flux into a pool of liquid flux-metal mixture. As the process proceeds down the joint, the trailing edge of the weld pool solidifies with most of the melted flux, along with other impurities, rising to the top as slag. The unmelted granular flux is vacuumed off and the slag removed mechanically. A schematic representation of the process is illustrated in Figure 2-1 [Ref. 9].

The chemical composition of the weld metal (that which was melted and re-solidified) can be influenced by the alloy content of the filler wire, the composition of the flux, and the composition of the base plate itself. The required filler wire composition is stated in MIL-E-26735 [Ref. 10] and provided in Table 2-1. The microstructure, and hence mechanical properties, of the weld metal are affected by the composition as well as the thermal cycle of the weldment. The thermal cycle is determined by the temperature of the base plate prior to welding (pre-heat), and the amount of energy delivered to the weld through the electrode (heat input). SAW welds generally have lower cooling rates than other welding processes due to the insulating effect of the flux, but pre-heating is still required to prevent hydrogen cracking when welding HY steels. Flux moisture and chemical content

is strictly controlled to minimize the flux as a source of hydrogen to the weld pool, also to minimize hydrogen cracking. The basicity of the flux is controlled to determine the amount of dissolved oxygen available in the weld pool, and hence the number and size of non-metallic inclusions in the weld metal [Ref. 5]. Flux basicity also affects the ease of slag removal after welding. If a proper microstructure free of cracking results from the welding process, the required mechanical property specifications of MIL-E-26735, partially enumerated in Table 2-2, will be achieved.

One of the most desirable microconstituents in the HY-100 weld metal is acicular ferrite, which will be introduced here as essentially bainite nucleated intergranularly in a prior-austenite grain. Since the energy barrier to homogeneous nucleation is high due to the large surface area to volume ratio, it nucleates on angular facets of the small non-metallic inclusions left behind as the larger ones have floated out into the slag (and perhaps autocatalytically). It would be expected that if the inclusion surface closely matches the acicular ferrite structure crystallographically, nucleation would more readily occur (this is one of several nucleation theories to be discussed later). Therefore, in order to understand the likelihood of forming acicular ferrite, the factors that determine the type of inclusions formed must be understood. [Ref. 11, pp. 251 - 268]

C. INCLUSION FORMATION IN THE WELD POOL

Steel manufacture has long required the use of deoxidizers and desulfurizers to improve the finished product. Ladle steel deoxidation refers to the addition of a component to react with the oxygen dissolved in the molten steel. This is often referred to as "killing" (eg. an aluminum killed steel). The flux can play a similar role in the deoxidation of weld metal. As the arc in SAW passes, flux, filler, and base plate are melted together and temperatures of about 2400 °C are reached [Ref. 12]. Electromagnetic effects between the weld metal and the arc cause turbulent conditions in the central portions of the weld pool. As this flowing mass starts to cool after the arc passes, chemical reactions in the liquid state occur, driven by the thermodynamics of chemical reactions. The thermodynamics are determined by the activities of the various elements in solution, which in turn are affected by concentration.

Babu et. al. [Ref. 13] use equilibrium thermodynamics and deoxidation diagrams to predict the reactions that will occur and tendency toward completion under the assumptions of constant temperature and weld metal composition. The weaknesses of these assumptions are obvious, in that the weld is constantly cooling and that the reactions occurring will cause a change in the weld metal composition, but the theory serves to point out the state of complexity in the inclusion formation problem. Thermodynamics, however, is not the only factor in the deoxidation process. The nucleation and growth kinetics associated with inclusion formation also play a role. Babu et. al. [Ref. 13] also address this and calculate the

nucleation rate of various oxides for a given steel composition and assumed inclusion-steel interfacial energy at various temperatures. Once nucleated, the inclusion grows until diffusion fields overlap and the reaction goes to completion. As the temperature falls, the thermodynamics of subsequent deoxidation reactions become favorable, and nucleation and growth of other oxides occur. Babu et. al. [Ref. 13] credit the layered structure of many inclusions studied to the heterogeneous nucleation of subsequently formed oxides and sulfides on previously formed oxides. A schematic representation of this is shown in Figure 2-2. For the steel which Babu studied, he predicted the sequence of oxide formation to be Al_2O_3 , $\text{MnO}\cdot\text{Al}_2\text{O}_3$, Ti_3O_5 , $\text{FeO}\cdot\text{Al}_2\text{O}_3$, TiO_2 , SiO_2 , and MnO . Dowling et. al. [Ref. 14] have identified the following inclusion phases in a HSLA weld metal similar to that studied by Babu using electron diffraction: $\text{MnO}\cdot\text{Al}_2\text{O}_3$, a titanium rich compound (probably TiO), a copper sulfide, a manganese sulfide, SiO_2 , and an unknown aluminum rich phase. Fox et. al. [Ref. 5] point out that Babu et al's treatment of inclusion formation ignores the possibilities that the oxides formed may have time to react with each other leading to a more equilibrium reaction product, and that reactions may continue in the solid state. This would make the phases detected differ from those originally nucleated. While these factors will need to be addressed in a comprehensive theory of weld metal inclusion development, Babu et al's effort shows how far the study has progressed compared to earlier efforts to explain weld metal deoxidation on a thermodynamic basis [Refs. 12, 15, 16 and 17].

Once the inclusions are formed, they either remain in the weld metal, or proceed to the surface of the weld pool as slag. Grong et. al. [Ref. 17] performed a study using various welding orientations in gas metal arc (GMA, aka. MIG) welds to prove that orientation has no effect on inclusion retention. They concluded from this that inclusion buoyancy has no effect, instead slag separation is due solely to turbulent flow conditions which lead to inclusion collision and coalescence at the surface of the weld pool. They go on to suggest that the turbulent flow is more prevalent directly under the arc, where the temperatures are also highest. In this "hot" portion of the weld pool, inclusions formed would collide under the influence of the flow, agglomerate, be stirred to the weld pool surface, and remain there as slag. Inclusions formed in the "cold" portion of the weld pool near the trailing edge, where flow is less and viscosity is higher, would remain in the weld metal on solidification. They present tentative data to support this in terms of a semi-empirical deoxidation parameter calculated at different temperatures, and from this determine the boundary temperature between the hot and cold portion of the weld pool for two series of welds. [Ref. 17]

D. WELD POOL SOLIDIFICATION AND THE δ -FERRITE TO AUSTENITE TRANSFORMATION

As the liquid weld metal loses heat into the base plates, thermal gradients are established, and solidification occurs. In the case of typical HY-100 welds, this solidification takes place by epitaxial nucleation of δ -ferrite on the exposed grains of the baseplate. The

cooling rates are such that a planar solidification front cannot be maintained, so a cellular front occurs. The result is several cells of parallel orientation being nucleated from each baseplate grain. Each group of these cells form a δ -ferrite grain. After nucleating, the grains whose growth axis more closely lie along the direction of maximum thermal gradient grow faster, crowding out less favorably oriented grains. As solidification proceeds, different grain orientations are favored as the thermal gradient changes with location, giving the grains a curved appearance, resulting in the typical columnar microstructure. [Ref. 9, pp. 143-146]

As the temperature continues to fall, austenite (γ) becomes the thermodynamically favored phase. It nucleates on the δ -ferrite grain boundaries due to surface energy considerations. The same surface energy considerations generally result in rapid growth along the grain boundaries followed by growth outward to consume the δ -ferrite grains. This is not the complete story, however, because the temperature gradient changes between the time that δ -ferrite solidifies and austenite forms. This causes a slight misorientation in the alignment between the two structures and, if the nucleation rate of austenite is high enough compared to the growth rate, a refinement in the grain size. In either case, the austenite grain structure is closely related to the δ -ferrite grain structure. [Ref. 18]

Sugden and Bhadeshia [Ref. 19] showed that, during solidification, larger inclusions can be pushed along by the surface tension of the solidification front, and hence end up in the region between adjacent cells. Smaller inclusions are passively enveloped. This makes it fortunate that HY-100 solidifies as δ -ferrite. This puts the larger inclusions in this alloy

inside the austenite grains vice on the grain boundary as they would be if it solidified as austenite. The importance of this distinction is apparent in the subsequent transformation of the austenite as it cools.

E. TRANSFORMATIONS ON COOLING AUSTENITE TO ROOM TEMPERATURE

As the weld metal cools from austenite into the α -ferrite (henceforth called strictly ferrite) region of the phase diagram, again the complex factors affecting nucleation and growth thermodynamics and kinetics determine the structures achieved. The literature on resulting weld metal microstructures is confusing, in that different authors classify the resulting microstructures with different terminology. For example, some use the term ferrite with aligned second phase, approved by the International Institute of Welding, which describes both Widmanstätten ferrite and bainite [Ref. 20]. Unfortunately, for the present work, it is important to distinguish between these two microstructures. The literature is further muddled by a lack of understanding of transformation mechanisms. For example, one group believes bainite is formed by a ledgewise diffusional growth mechanism [Ref. 21], while another believes in a displacive-diffusive mechanism [Ref. 22]. This confusion makes it necessary to define exactly what is meant by various terms. In the case of this study, the definitions according to Bhadeshia et. al. [Ref. 18] were adopted with the addition of bainite which was not present in the weld metal they studied.

1. Grain Boundary (Allotriomorphic) Ferrite

Grain boundary ferrite is used to describe ferrite which transforms from the austenite at the austenite grain boundaries. This is the first reaction to occur on cooling due to the high grain boundary energy. This reaction proceeds by a diffusive mechanism and is hence hindered by substitutional alloying.

2. Side Plate (Widmanstätten) Ferrite

Side plate ferrite is ferrite which grows from ferrite-austenite boundaries (or sometimes from austenite-austenite boundaries) in the form of parallel plates. The plates are usually much coarser than those of bainite. The plates form by a displacive mechanism, with carbon subsequently diffusing out of the plates [Ref. 23]. Since the plates grow quickly outward from the boundary and slowly perpendicularly to it, the carbon diffuses to the area between the plates, which is then either retained as austenite or transformed to martensite on cooling to room temperature.

3. Bainite

Bainite consists of small parallel plates of ferrite initially nucleated at austenite grain boundaries. Once one plate forms, subsequent plates can form sympathetically, resulting in highly organized clusters of ferrite plates, which can stretch across the austenite grains. The resulting microstructure consists of sheaves of ferrite plates, which, when viewed as a whole, can look like a single plate with internal carbides. The mechanism of bainite formation is still being debated [Refs. 21,22,24,25,26], but in this work a displacive-diffusive reaction as

described for side plate ferrite will be assumed. Again, some retained austenite or martensite may result from carbon diffusion out of the ferrite plates, enriching the surrounding region and preventing it from transforming to bainite as well.

4. Acicular Ferrite

Acicular ferrite is essentially bainite which nucleates on inclusions instead of on austenite grain boundaries [Ref. 26]. It forms over the same temperature ranges and has the same characteristics. It can be expected that its nucleation rate will be lower due to the curvature of the inclusion-austenite boundary [Ref. 5]. Acicular ferrite is formed by a displacive-diffusive reaction [Ref. 27], again resulting in retained austenite or martensite in the regions adjacent to the plates. Acicular ferrite sometimes forms as isolated plates, but can also form as clusters with similar spatial orientations [Refs. 28,29]. The alignment of plates can also be influenced by externally applied stresses [Ref. 30].

5. Martensite

Martensite is a metastable iron phase, supersaturated in carbon, that results from the nearly diffusionless transformation from austenite [Ref. 31, pp.312-314]. It is one of the microphases identified by Bhadeshia et. al. [Ref. 18], a classification applied to the "leftovers" after the above listed constituents form. Since it was impossible to differentiate between retained austenite, degenerate pearlite mixtures, and martensite based on optical microscopy, it was assumed in this study that all were martensite, based on the CCT curves of similar steels.

The factors that affect the formation of each of the above constituents are complex and interrelated. The first is weld metal composition. From this, a basic continuous cooling transformation diagram (CCT curve) can be obtained. One that might apply to HY-100 weld metal would be similar to that shown in Figure 2-3 [From Ref. 32], except the bainite nose would not be the whole way to the left (there would be a martensite region). This basic CCT curve would then need to be modified based on the interactions between the various microstructures. For example, Babu and Bhadesia [Ref. 33] have shown that formation of significant amounts of grain boundary ferrite result in no nucleation sites remaining for bainite, resulting in a greater propensity for acicular ferrite formation. Added to this, one would have to consider the prior austenite grain size effects on nucleation potential for bainite (more grain boundary area implies more bainite nucleation sites and thus more bainite) [Ref. 33] as well as grain boundary and side plate ferrite. Unfortunately, austenite grain sizes vary in different locations of the weld, particularly for multi-pass welds. This results in different CCT curves for various weld regions. Figure 2-4 shows this effect for a non HY-100 steel [Ref. 32]. Another factor, not directly calculable from chemistry alone is inclusion population. With no inclusions, acicular ferrite will not form. In order, then, to understand the CCT curve of a given area, one must understand the factors that affect each microstructural constituent, and to understand these, one must understand mechanisms of formation. Since acicular ferrite content improves both strength and toughness, it is the most

sought after microconstituent. For this reason it is worthwhile to digress into how it nucleates on inclusions.

F. ACICULAR FERRITE NUCLEATION

Several theories have been developed to describe what favors acicular ferrite nucleation on some inclusions and not others. The four theories summarized by Fox and Eakes [Ref. 5] are: 1) nucleation of ferrite on an inert substrate, 2) epitaxial growth on a suitably oriented inclusion facet, i.e. lattice matching, 3) strain energy effects due to differences in the thermal expansion coefficients of the inclusion and the matrix, and 4) a lower hardenability in the region near an inclusion due to the diffusion field during its formation. Grong et. al. [Ref. 34] have shown that with inclusions they analyzed which were nucleators of acicular ferrite (TiN , $\text{MnO} \cdot \text{Al}_2\text{O}_3$, and Al_2O_3) there was both an orientation relationship of the acicular ferrite to the inclusion and to the prior austenite grain. They also showed that the noted orientations were those appropriate for lattice matching. This is evidence that the lattice matching mechanism is active, at least in the types of inclusions they analyzed. They went on to show that for inclusions with three phases of suitable lattice matching and cubic structure (single crystal of each) approximately 12% of randomly oriented inclusions would be suitably oriented to nucleate acicular ferrite. It follows that if each phase within the inclusion is polycrystalline, the probability may be higher.

Much evidence exists that certain types of inclusions more readily nucleate acicular ferrite than others. Most of the evidence however, cannot explicitly rule out other factors and varies from weld metal to weld metal and with heat input. Dowling et. al. [Ref. 14] point out some of these discrepancies. Gregg and Bhadeshia [Refs. 35, 36] have conducted a series of experiments by pressure bonding different ceramics with steels and observing whether they nucleate bainite. Those that do appear to do so either by affecting the localized chemical composition or by unknown means. Unfortunately, Gregg and Bhadeshia [Ref. 36] found galaxite ($\text{MnO} \cdot \text{Al}_2\text{O}_3$) and TiN to be ineffective nucleators of bainite, while Grong et. al. [Ref. 34] studied these and noted orientation relationships with acicular ferrite. The conclusion must be that either one group of experimenters is wrong, or that there is some difference between a layer of fine powders being heated and an inclusion present in the weld metal, or that different mechanisms are in effect for different inclusions and weld metals.

The perfect experiment would result in inclusion phase identification using both chemistry and crystallography, orientation determination of the inclusion with respect to the matrix and acicular ferrite, and nucleation site on the inclusion; all of which are theoretically possible in a transmission electron microscope (TEM). Chemical determination is somewhat mutually exclusive with nucleation site or orientation because site identification and orientation require the use of a thin foil, which will hinder chemical determination by energy dispersive x-ray analysis (EDX) due to matrix interference in much the same way as it does in the scanning electron microscope (SEM) [Ref. 3, p. 41]. Chemical analysis of single

phases in an inclusion may be difficult due to the limit of spatial resolution of the TEM in EDX mode. The EDX detector usefulness is also limited due to its inability to quantify light elements like oxygen and nitrogen accurately, making it impossible to determine which of the various oxides of a given element are present by EDX alone (TiO , TiO_2 , Ti_2O_3 , Ti_3O_5 are examples which cannot be distinguished). Parallel electron energy loss spectrum analysis (PEELS) would be an alternative, but the inclusions are usually too thick for EELS analysis. The thickness of the inclusions also hinders phase determination by electron diffraction. Thick inclusions are not sufficiently penetrated by the electron beam to produce high quality diffraction patterns. Even in thin inclusions, the multi-phase polycrystalline nature yields a superpositioning of several spot patterns, analysis of which are difficult, especially since major zone axes do not have parallel orientations. If sufficient spatial resolution can be obtained to isolate a single crystal in the electron beam, perhaps using a grazing technique, EDX and electron spot diffraction may be possible simultaneously. Small electron probes may also cause heating and subsequent phase transformation in the inclusions themselves, causing improper phase determinations.

Whatever their composition, inclusions are required to nucleate acicular ferrite. Three of the four proposed mechanisms of acicular ferrite formation on inclusions would result in some inclusions being more favorable nucleation sites than others. With improved equipment and techniques, investigators will eventually understand the mechanism or mechanisms active in acicular ferrite formation in various steels. At that point, engineering

of the proper inclusions using the deoxidation theory espoused by Babu et al [Ref. 13] should be possible. This could result in higher proportions of acicular ferrite in the resulting weld metals, and hence strong and tough welds.

G. MULTI-PASS EFFECTS

As if the above wasn't complex enough, the fact that many welds consist of more than one pass further complicates the trends noticed in a study of welding. The weld metal that was laid down by a previous pass is partially re-melted and at least re-heated when the next pass is laid down. One effect of this is that the chemistry of the weld metal will change as the composition is less that of the base plate and more that of the filler wire for welds not adjacent to the base plate. Another is that some of the previous pass is re-austenitized. Depending on the thermal cycle experienced (determined by where the metal being considered is in relation to the weld pool), re-austenitization can result in a very large or very small austenite grain size. In Figure 2-4 it was shown how this could result in changes in the CCT curves. Reed and Bhadeshia have developed a model to determine the extent of re-austenization in a multi-pass weld [Ref. 37]. Eventually from work like this, complete thermal profiles may be developed for each point in the weldment, and from these, a model of the microstructure.

Bhadeshia [Ref. 23] has also developed the beginnings of a theory to explain the mechanical properties of multirun welds based on as deposited microstructures and alloy

chemistry. He models strength as a function of solid solution, microstructural, and pure annealed iron components. He considers all the fully reaustenitized region to have mechanical properties similar to that of the as deposited structure, and partially reaustenitized and tempered regions to have lost most of their microstructural component of strength. He notes that one of the primary influences of weld metal chemistry on weld metal properties is the lowering of the austenite transformation temperatures with alloying element addition. He also discusses a model to predict % elongation, but admits that there is no model able to predict toughness. This leaves weld metal chemistry as an unsatisfying, but useful, parameter even though mechanical properties are dependent on many other factors as well. [Ref. 23]

H. SUMMARY

The above shows that welding metallurgy is an extremely complex science, which is not yet fully understood. The results of any given weld depend on many factors. First is the chemistry of the material being welded. The base plate chemistry and microstructure will help determine if a region of the base plate HAZ will be susceptible to cracking. Next, the welding process selected (GMA, SAW, etc.) will determine heat inputs, deoxidation methods, and practicality of the weld (joint design and location). The composition of the filler wire and flux, if used, will influence the chemistry of the weld metal and the adherence of the slag. Weld parameters such as heat input will determine the thermal profile

experienced by the weld metal and the HAZ, as well as influence the weld metal chemistry by determining the amount of base-plate being melted. The presence of trace elements in the base plate will affect the deoxidation reactions, and hence inclusion type and content. The amount of pre-heat and alloying element addition will affect the cooling curve as shown in Figure 2-3. For these reasons, systematic welding experiments must only vary one or two parameters and specify all in order to be meaningful. In this light, one experiment jointly conducted between the Naval Surface Warfare Center, Carderock Division (NSWC) and the Naval Postgraduate School (NPS) was to use various commercial fluxes with constant SAW parameters on HY-100 to study the effects of changing the flux composition [Refs. 1-5]. The effects of varying the many components of the flux simultaneously in complex ways led to analyses only of overall trends. It was therefore decided to choose one component of the flux and systematically vary it, then study the effects from weld metal deoxidation to mechanical properties. The following is the resulting experiment for manganese oxide.

A trial observation of the effect of adding a small amount of cerium oxide was also performed. In a special low temperature steel, cerium additions have been shown to lower the amount of grain boundary ferrite formed. This is believed to be due to cerium segregating to the austenite grain boundaries and lowering their energy as is known for boron additions. The trial addition was to observe the effect of cerium addition through the flux on this steel, which has very little grain boundary ferrite to start with. [Ref. 23]

**Table 2-1. HY-100 and HY-100 SAW Filler Wire
Required and Actual Chemical Compositions [After Refs. 1, 6 and 10 ¹].**

Element	HY-100 Steel		HY-100 Filler Wire	
	MIL-S-16216	Actual	MIL-E-23765	Actual
Carbon	0.12-0.18	0.157	0.084²	0.081
Manganese	0.10-0.40	0.33	0.90-2.35	1.57
Phosphorous	0.015 max	0.003	0.012 max	0.004
Sulfur	0.008 max	0.005	0.008 max	0.006
Silicon	0.15-0.38	0.3	0.60 max	0.44
Nickel	2.25-3.50	2.79	1.00-3.0	2.25
Chromium	1.00-1.80	1.46	0.80 max	0.28
Molybdenum	0.20-0.60	0.36	0.30-1.00	0.42
Vanadium	0.03 max	0.006	0.03 max	0.001
Titanium	0.02 max	0.004	0.10 max	0.014
Copper	0.25 max	0.097	-	0.011
Antimony	0.025 max	-	-	-
Arsenic	0.025 max	-	-	-
Tin	0.030 max	-	-	-
Aluminum	-	0.018	0.10 max	0.012
Zirconium	-	<0.001	0.10 max	0.012
Oxygen	-	0.0054	-	0.003
Nitrogen	-	0.016	-	0.004
Boron	-	0.001	-	0.004
Hydrogen	-	1.1 ppm	3.0³	2.8 ppm

1- All values in weight percent unless specified. 2- 0.090 max for certain applications. 3- milliliters diffusible hydrogen deposited per. 100 grams weld metal

**Table 2-2. HY-100 Plate and Submerged Arc Weld
Mechanical Property Specifications (Partial) [After Refs. 8 and 10].**

	HY-100 Plate - MIL-S-16216		HY-100 SAW - MIL-E-23765	
Yield Strength (MPa)	690-827		703-848 ave 690-861 single	
Minimum Elongation in 2 inch section (%)	18		15	
Minimum Area Reduction in Round Section (%)	45		-	
Charpy V-notch Impact Energy	-84.4±1.7 °C three specimens	54.2 N-m min. ave.	-51.1 °C five specimens	61.0 N-m min. ave.
		47.5 N-m min. single value		no two below 61.0 N-m
		50% min. ave. fibrous fracture area		47.5 N-m min. single value
	-17.8±1.67 °C three specimens	81.4 N-m min. ave.	-17.8 °C five specimens	81.4 N-m min. ave.
		74.6 N-m min. single value		no two below 81.4 N-m
		90% min. ave. fibrous fracture area		67.8 N-m min. single value

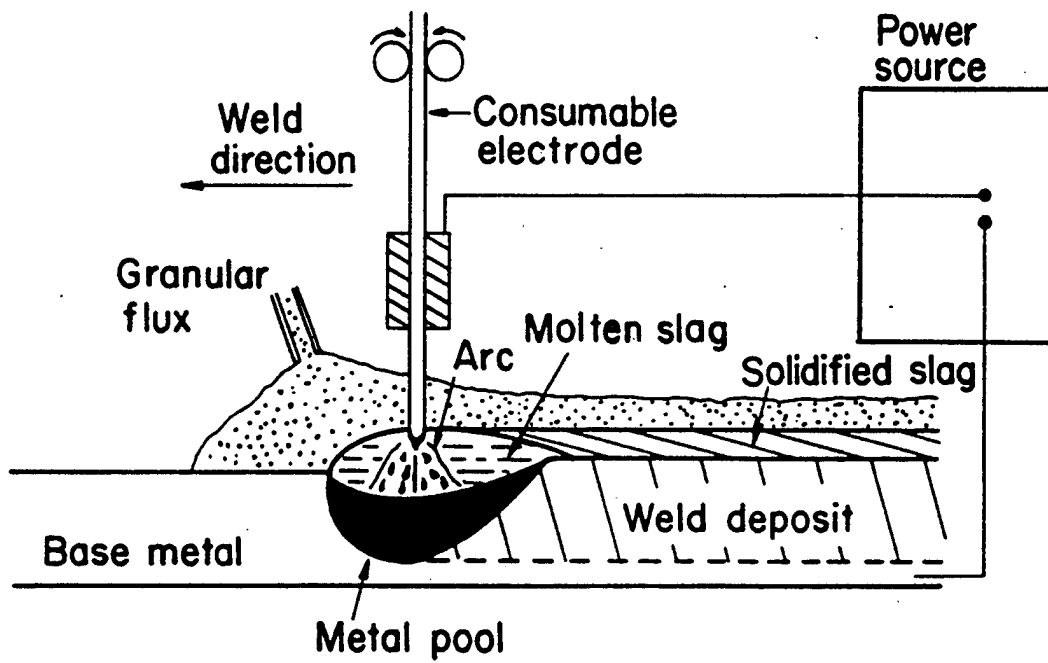
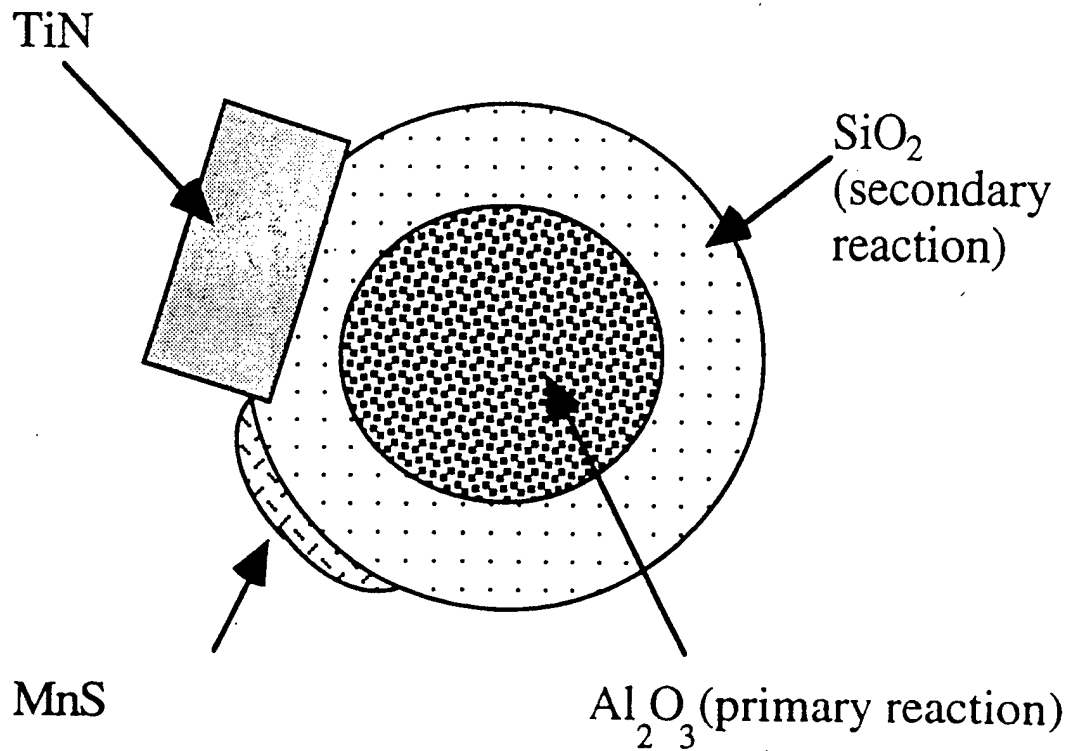


Figure 2-1. The Submerged Arc Welding Process [From Ref. 9].



morphology may be much more complicated in real weld metal inclusions – MnS formation may occur during final part of solidification as interdendritic liquid becomes enriched in sulphur, and TiN growth can occur in solid state on oxide inclusions formed previously in liquid steel

Figure 2-2. Schematic diagram of Layered Structure of Inclusions Due to Sequential Oxidation Reactions [From Ref. 13].

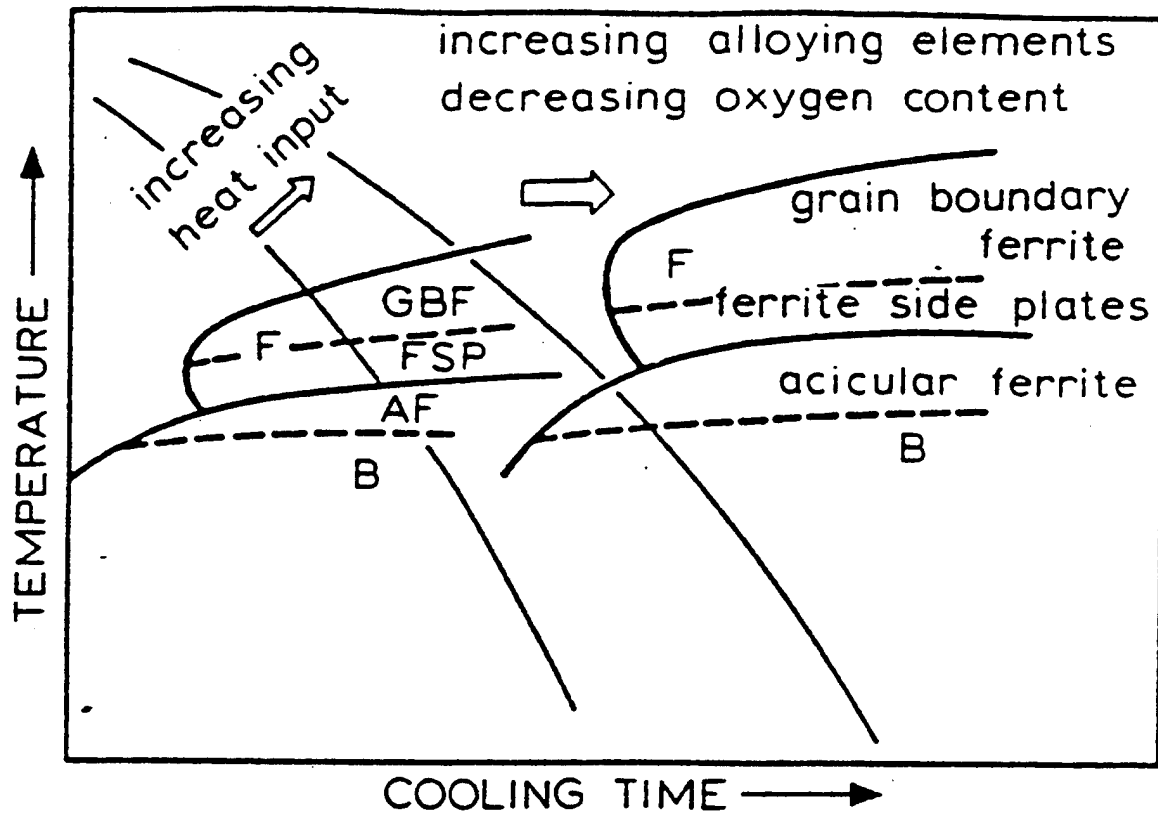
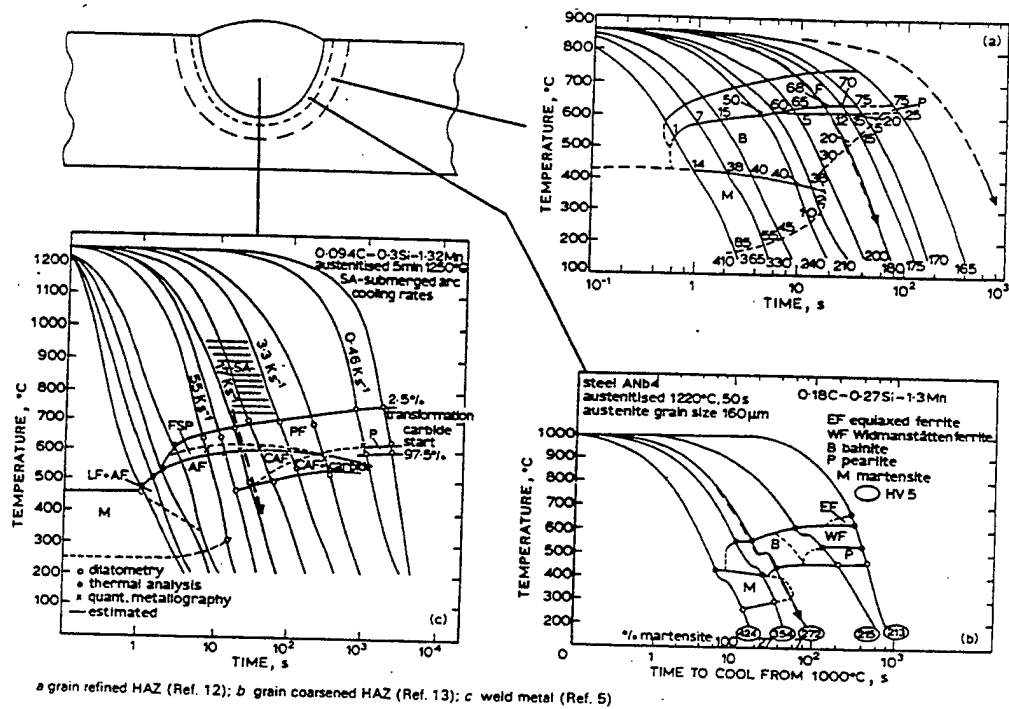


Figure 2-3. A CCT Curve Similar to That of HY-100, Except it Shows No Martensite Region [From Ref. 32].



III. EXPERIMENTAL PROCEDURES AND RESULTS

A. SAMPLE PRODUCTION

1. Flux Preparation

The Naval Surface Warfare Center (NSWC); Annapolis Detachment, Carderock Division was responsible for flux preparation. In order to minimize the effects which could be introduced by differences in flux chemistries (viscosity, heat conduction, chemical activity, basicity, current carrying capacity, etc.) all the experimental fluxes designed for this experiment were prepared from the same dry mix, Oerlikon OP121TT; lot 1161. This dry mix was selected because it should result in fluxes similar to the commercial flux Oerlikon OP121TT; lot 1131, one of the top performers in previous commercial flux comparison experiments conducted by NSWC and NPS [Refs. 1-5]. Devasco International of Houston, TX was hired to prepare fluxes from the dry mix and the following constituents; F326-100% dry mix, F327-99% dry mix 1% MnO, F328-98% dry mix 2% MnO, F329-97% dry mix 3% MnO, and F330-99.5% dry mix 0.5% CeO₂. Devasco prepared the fluxes in 22.7 kg. batches, two batches per flux, using the following procedure. First the dry ingredients listed above were weighed, then dry blended for 3 min. in a 1 ft. by 3 ft. conical Patterson Kelley mixer. To this was added the binder, a mixture of 75% K6, and 25% grade 47 (primarily potassium and sodium silicates respectively) in a 1.5% potassium hydroxide solution. The binder was added over a period of approximately five minutes. The mixer was stopped and

scraped to ensure nothing was sticking to the sides, then run for an additional two minutes. The mixture was then baked at 732 °C for five minutes in an electric rotary kiln, then sifted through an eight mesh screen. The two 22.7 kg. batches for each flux were then blended together. All the fluxes were then shipped to NSWC in 22.7 kg. buckets. The use of a commercial dry mix inherently means the exact chemical composition was unknown. A "best guess" chemistry of the dry mix and fluxes was obtained by NSWC, employing a semi-quantitative combination of the following analyses conducted by NSWC; inductively coupled plasma, X-ray fluorescence, optical emission spectroscopy, and ion-selective electrode techniques. This estimate ignores the fact that the dry mix probably contains carbonates in addition to silicates, oxides, and fluorides. These chemistries are listed in Table 3-1, along with F292, the commercially available flux from the previous experiment. These chemistries must be used with caution, particularly the basicity index (BI). Based on the experimental variation of MnO, the only parameter intentionally changed, the basicity index should have changed by only 0.09 using the relationship of Ref. 5, the same relationship used to calculate the table values.

2. Welding Parameters

The welding parameters were controlled to be the same as those previously used in the commercial flux experiment [Refs. 1-5]. These parameters are listed in Table 3-2. Although base plate and filler wire chemistries were not analyzed, they should be similar to those of the commercial flux experiment, previously given in Table 2-1.

B. WELD METAL CHEMISTRY

Weld samples were sent by NSWC to Luvak, INC. for analysis (one sample per weld). The results are listed in Table 3-3, with confidence intervals supplied to previous researchers [Ref. 38].

C. MECHANICAL TESTING

Two tensile tests were conducted at NSWC per weld. Sections were cut longitudinally from the weld (minimum depth 3.2 mm.), and machined into standard 1.28 cm. diameter test pieces. In addition, fifteen Charpy V-notch samples (10 mm. by 10 mm. by 10 cm.) were machined from each weld and fractured, three per test temperature, at NSWC. Note that a full spectrum of testing per MIL-E-23765 was not conducted [Ref. 10]. Average test results for tensile and Charpy testing are listed in Table 3-4. Figures 3-1 and 3-2 show Charpy impact energy and fracture appearance curves versus temperature.

D. SCANNING ELECTRON MICROSCOPY

One 2 cm. section was cut from each weld and sent to NPS for analysis. One face of the section transverse to the weld centerline was surface ground using an aluminum oxide wheel, then finely ground using silicon carbide papers of various grits. The surface was then polished using 15, 6, and 1 micron diamond spray to a 1 micron finish. Inclusion fields were

then analyzed on a Cambridge Stereo Scan S200 scanning electron microscope (SEM) using a LaB₆ filament at 20,000 volts. A nine mm. working distance was used at 7040 times magnification in the back-scattered mode for an approximate field of view of 180 square micrometers ($\mu\text{m.}$, microns) per field. 100 fields were analyzed per sample and each inclusion counted and categorized by size according to the bins available on the SEM cursor. The first several samples analyzed were flawed due to inexperience of the operator and problems with corrosion pitting on the surface. Representative counts appear in Figures 3-3 through 3-8. Since small oxide pits and polishing artifacts were always present on the surface and operator inexperience affected the detection of inclusions only near the limit of resolution of the SEM, it was decided to use only inclusions greater than 0.25 $\mu\text{m.}$ and to average all counts performed when comparing the samples in this study. This was justified due to the similarity in all counts at inclusion sizes above 0.25 $\mu\text{m.}$ Table 3-5 gives the statistics for these average counts. No correction was attempted for the partial submergence of the inclusions counted as would be required in the optical microscope due to the penetration of the SEM bulb of interaction [Ref. 39]. SEM analysis was also used to obtain qualitative photographs of microstructures on F292 and F328 at various magnifications for comparison. Figures 3-9 through 3-12 are representative. These micrographs were obtained following a 6 second etch using 5% nitric acid in methanol (5% nital). This etch revealed the microstructure without obscuring larger inclusions. A mixture of signals from the

secondary electron and back scattered detectors was found to improve the images so that both the microstructure and inclusions could be clearly seen.

E. OPTICAL MICROSCOPY

All optical microscopy was performed on a Zeiss Jenaphot 2000 optical photomicroscope. Following the recommendations of Hilliard and Cahn, [Ref. 40], all quantitative optical microscopy was performed using the systematic manual point count technique. ASTM standard E 562-89 [Ref.41] was followed, except the recommended number of grid points per field for the volume fractions being analyzed. This was justified due to the dispersion of phases but did result in less than the expected data scatter; Ref. 41 is written for more well defined regions of microstructure than that occurring in the welds analyzed. The requirement that individual components of the microstructure not overlap successive grid points was met. Statistical analysis was conducted using binomial approximations as explained by Gladman and Woodhead [Ref. 42] vice ASTM E 562-89 due to the simplicity of the method. The binomial approximation results in:

1.

$$\sigma^2 = p(1-p)/n$$

where σ is the standard deviation, p the proportion of the phase being analyzed, and n the number of points analyzed.

Volume percent acicular ferrite in the region of the Charpy testing was determined using photographs of ten random fields near the center of each weld at 500 times magnification following polishing to 1 micron diamond and etching in 5% nital for 12 seconds. Type 667 Polaroid film was used with a 1.27 cm. rectangular grid to give 48 grid points per photo (480 per sample). Figures 3-13 through 3-18 show typical microstructures for each of the prepared samples as well as F292 for comparison.

Additional microstructural analyses were conducted in the following weld regions after polishing to 1 micron diamond and etching in 5% nital for 6 seconds; in the columnar region of the last welding pass to investigate primary structure, in the weld metal heat affected zone (HAZ) surrounding that pass to investigate the fully reaustenitized structure, and in the columnar regions of passes laid previously to investigate tempering effects and partial reaustenitization that did not destroy the columnar nature of the macrostructure. It is important to note that these pictures were taken in the weld metal, base plate photographs were obtained, but not quantitatively analyzed. Photographs were obtained at 1000 times magnification on 35 mm. film and made into 12.70 by 17.78 cm. prints for a final magnification of 1600 times. Four photographs were obtained from each area of every sample for quantitative analysis. These were analyzed for the content of acicular ferrite, bainite, martensite, Widmanstätten ferrite, and grain boundary (allotriomorphic) ferrite using a 1.27 cm. rectangular grid pattern, resulting in 117 grid points per photo (468 per sample). Figures 3-19 through 3-37 represent some of the microstructures observed. Additional

photographs were obtained with various magnifications and processes for comparative and illustrative purposes (Figures 3-38 through 3-44). The results of the quantitative microstructural analyses are listed in Table 3-6.

F. MICROHARDNESS MEASUREMENTS

Vickers microhardness measurements were made at NPS using a Buehler Micromet 2004 microhardness machine with one kilogram load and diamond pyramid indenter. After polishing to one micron diamond finish and etching in 5% nital for six seconds, traverses were conducted from the last pass columnar region, through the HAZ, and into the prior pass columnar region on each sample. Microhardness test results appear in Table 3-7. Due to the differing number of indentations in the various regions of each sample, no overall average was calculated.

G. INCLUSION CHEMISTRY

Carbon extraction replicas were prepared on the five samples produced for this experiment as follows. The samples were polished to 1 micron diamond finish then etched in 5% nital for 25 seconds. They were then carbon coated with an EFFA Mk II carbon coater using two carbon filaments at a distance of about 3.20 cm.. Several squares approximately 3 mm. in width were scribed in the carbon to promote separation on deep etching. The sample was then placed face up in 5% nital until the squares floated off after approximately

five minutes. As the squares floated free, they were caught and placed in a solution of 20% acetone in water where they would un-twist. They were then captured on 400 mesh copper grids for analysis in the Transmission Electron Microscope (TEM). Two replicas were produced per sample, but analysis was only performed on one.

Inclusion chemistry was determined using a JEM-100 CX II TEM with a LaB_6 filament at 120,000 volts. The atomic content was analyzed using a Kevex Delta Class energy dispersive x-ray (EDX) analyzer with Quantex software. As explained by Eakes [Ref. 3, p. 41], the preparation of a carbon replica with inclusions attached eliminates interference from the steel matrix. Between twenty and thirty inclusions were analyzed per sample. The atomic compositions were composed of the elements shown in Tables 3-9 through 3-13. Trace amounts of Ca and Fe were also noted on some inclusions, but not enough to analyze.

It was readily recognizable that most of the inclusions had remarkably similar composition. Tables 3-8 through 3-13 show twenty of these typical inclusions per sample.

Occasionally, however, one was analyzed which seemed to have significantly higher concentrations of Mn and S, presumably due to high content of MnS. These (9 total of 128) were not included in Tables 3-9 through 3-18. Table 3-8 gives inclusion chemistry for F292 (commercial flux) as determined by Eakes [Ref. 3] with totals changed to eliminate an MnS inclusion for consistency with the present work. In addition to abnormal MnS inclusions, three inclusions with abnormally high Al concentrations were noted and passed over for

F326 and F330. Inclusion oxide contents were calculated to position each inclusion on the Al_2O_3 - MnO - SiO_2 ternary phase diagram. This was done by starting with the atomic percents of the analyzed elements, modifying the Mn content by subtracting off one Mn atom percent for each sulfur atom percent (assumes all sulphur is present as MnS), subtracting off one Mn atom percent for each Ti atom percent (assumes all Ti is present as $\text{MnO} \cdot \text{TiO}_2$), dropping the Mg, Zr, and Cr, dividing the Al by two (two Al in Al_2O_3), multiplying by the molecular weight of the appropriate oxide, and normalizing to 100 percent.

In addition to inclusion chemistry, an attempt was made to perform an electron diffraction experiment on the phases in the inclusions. Figure 3-45 shows a typical inclusion along with its electron diffraction pattern. Due to the multi-phase poly-crystalline nature of the inclusions, the resulting diffraction patterns proved to be more difficult to analyze than time permitted. Use of a TEM with higher accelerating voltage and smaller probe sizes may allow this at a later date.

Table 3-1. "Best Guess" Flux Chemistries in Weight Percent.

	F292 OP121 Flux	OP121 Dry Mix	F326 Base	F327 1%Mn O	F328 2%Mn O	F329 3%Mn O	F330 0.5% CeO ₂
Al ₂ O ₃	18.40	19.50	19.00	21.60	20.10	19.90	20.40
CaF ₂	22.20	22.20	22.60	28.77	26.71	25.27	25.89
CaO	12.50	13.10	9.87	10.24	10.11	9.65	10.00
Fe ₂ O ₃	1.37	1.5	1.64	1.19	1.26	1.37	1.37
K ₂ O	0.68	0.03	1.06	1.17	1.22	1.12	1.13
MgO	28.2	30.4	31.2	18.7	21.8	23.7	25.1
MnO	0.86	1.06	0.76	2.84	3.62	4.26	0.88
Na ₂ O	0.71	-	0.21	0.27	0.25	0.23	0.21
P ₂ O ₅	-	-	0.06	0.06	0.06	0.06	0.06
SiO ₂	13.5	10.0	12.3	13.5	13.0	12.7	13.0
TiO ₂	0.70	0.77	0.74	0.78	0.77	0.77	0.79
CeO ₂	0.006	0.006	0.009	0.014	0.012	0.011	0.442
ZrO ₂	0.031	0.036	0.027	0.041	0.041	0.014	0.027
Loss on Ignition	0.710	1.110	0.720	0.510	0.560	0.380	0.730
other ¹	0.120	0.214	0.174	0.148	0.301	0.151	0.173
Total	99.989	99.922	100.370	99.828	99.774	99.587	100.204
Basicity Index ²	2.81	N/A	2.94	2.45	2.64	2.70	2.66

1- BaO, Bi₂O₃, CoO, Cr₂O₃, CuO, Ga₂O₃, La₂O₃, MoO₃, NiO, PbO, Sc₂O₃, SrO, Y₂O₃,
V₂O₅

2- per. Ref. 5.

Table 3-2. Welding Parameters [After Ref. 1].

Base Plate Thickness	2.54 cm.
Root Gap / Angle	1.27 cm. / 45 degrees
Number of Passes	21 or 24
Filler Wire	L-TEC 120
Wire Diameter	0.238 cm.
Tip to Work Distance	1.588 cm.
Current	500 amp DC reverse polarity
Voltage	35 Volts
Travel Speed	48.3 cm./minute
Heat Input	21.77 kilojoules/cm.
Preheat/Interpass Temperature	121.1-135.0 °C
Post Weld Soak	None
Flux Recycled	None
Cooling Rate	10-12.8 °C/sec @ 538 °C
time from 800-500 °C	16.29 sec. (calculated)

Table 3-3. Weld Metal Chemistry in Weight Percent.

Element	Confidence Interval	F292 Comm- ercial Flux	F326 Base	F327 1% MnO	F328 2% MnO	F329 3% MnO	F330 0.5% CeO₂
C	0.001	0.062	0.056	0.059	0.055	0.054	0.056
Mn	0.02	1.49	1.37	1.45	1.71	1.75	1.42
Si	0.01	0.46	0.53	0.38	0.36	0.38	0.47
P	0.002	0.005	0.011	0.011	0.013	0.012	0.009
S	0.001	0.006	0.007	0.003	0.003	0.002	0.005
Ni	0.05	2.56	2.62	2.62	2.54	2.59	2.63
Mo	0.01	0.52	0.45	0.43	0.44	0.43	0.40
Cr	0.02	0.43	0.42	0.45	0.39	0.43	0.44
Nb	0.001	-	0.004	0.004	0.004	0.005	0.005
V	0.001	0.003	0.005	0.005	0.005	0.005	0.005
Al	0.002	0.020	0.020	0.014	0.014	0.020	0.017
Ti	0.001	0.008	0.009	0.006	0.006	0.006	0.009
Cu	0.001	0.023	0.025	0.031	0.023	0.026	0.027
Zr	0.001	0.003	0.003	0.003	0.003	0.003	0.003
B	0.001	0.003	0.003	0.003	0.003	0.003	0.003
Ce	-	-	0.0004	<0.0004	<0.0004	<0.0004	<0.0004
O	0.001	0.027	0.031	0.028	0.028	0.029	0.028
N	0.001	0.006	0.006	0.006	0.006	0.006	0.006
H	0.00001	0.00004	0.00012	0.00017	0.00010	0.00013	0.00013

Table 3-4. Average Mechanical Test Results.

Property		F292 Comm- ercial	F326 Base	F327 1% MnO	F328 2% MnO	F329 3% MnO	F330 0.5% CeO₂
Yield Strength (MPa)		752.2	751.5	737.7	759.1	835.0	766.7
% Elongation		19.5	23.5	24.0	24.0	22.5	25.0
Charpy V-notch Impact Energy (N-m)	-84.4 °C	42.87	32.09	19.89	60.33	15.82	40.23
	-51.1 °C	84.74	40.67	65.53	98.07	81.80	92.64
	-17.8 °C	115.65	122.93	95.82	120.22	81.35	122.02
	15.6 °C	123.90	141.01	116.15	129.71	102.60	131.5
	48.9 °C	128.57	130.61	129.71	134.67	107.56	138.74
Fracture Appear- ance % Shear	-84.4 °C	12.50	30.00	23.33	40.00	26.67	30.00
	-51.1 °C	54.00	46.67	43.33	76.67	66.67	80.00
	-17.8 °C	86.00	90.00	76.67	93.33	76.67	96.33
	15.6 °C	100.00	96.67	93.33	100.00	95.00	100.00
	48.9 °C	100.00	99.67	98.33	100.00	95.00	100.00
Individual Measurements all in Specifications per. MIL-E-23765		✓			✓		✓

Table 3-5. Inclusion Statistics Summary.
Average of All Counts - Inclusions > 2.5 μm Diameter.

	F292 Comm.	F326 Base	F327 1%MnO	F328 2%MnO	F329 3%MnO	F330 0.5%CeO₂
inclusion count	373	582	591	426	496	494
mean size (μm)	0.3852	0.4292	0.4421	0.4670	0.4489	0.4261
volume percent inclusions	0.28	0.55	0.59	0.46	0.50	0.43

Table 3-6. Quantitative Optical Microscopy Results (%).

		F292 Comm.	F326 Base	F327 1% MnO	F328 2% MnO	F329 3% MnO	F330 .5% CeO₂
Weld Acicular Ferrite (480 points)		66.04	66.46	67.08	69.17	71.67	63.33
Final Pass (468 points)	AF	76.07	55.12	59.40	74.36	85.26	53.42
	Bainite	16.88	31.84	25.21	6.20	12.61	35.68
	M	6.41	13.03	13.68	17.31	2.14	10.90
	GB	0.64	0	1.71	1.93	0	0
Weld Metal Coarse HAZ (468 points)	AF	64.53	48.50	65.60	47.86	52.56	60.47
	Bainite	24.15	46.58	30.34	26.28	28.85	38.68
	M	10.90	4.91	4.06	24.79	18.59	0.85
	GB	0.43	0	0	1.07	0	0
Prior Pass Columnar HAZ (468 points)	AF	64.74	66.88	73.29	40.17	44.44	58.76
	Bainite	32.69	30.56	20.51	55.98	33.76	38.46
	M	2.56	2.56	6.20	0	21.79	2.78
	GB	0	0	0	3.42	0	0

AF- Acicular Ferrite M- Martensite GB- Grain Boundary Ferrite

Table 3-7. Vickers Microhardness Test Results.

		F292 Comm.	F326 Base	F327 1% MnO	F328 2% MnO	F329 3% MnO	F330 0.5% CeO ₂
Last Pass Columnar	Mean	302.3	288.8	292.2	345.5	349.8	320.9
	Std.Dev.	5.86	13.74	2.43	11.34	9.64	4.80
	# tests	8	8	9	10	9	6
	Max.	312.3	309.1	296.7	359.7	364.7	327.4
	Min.	294.1	273.1	288.6	322.3	334.5	315.6
Prior Pass Columnar	Mean	298.9	298.0	281.9	320.5	321.3	292.1
	Std.Dev.	9.99	7.51	19.72	10.60	25.29	14.19
	# tests	13	8	13	8	8	8
	Max.	315.2	307.9	314.3	333.2	359.2	309.1
	Min.	280.2	288.6	254.8	303.2	288.3	270.8
Root of Columnar Cells	Mean	313.0	315.5	297.8	363.8	332.0	308.1
	Std.Dev.	8.34	4.50	-	5.02	32.22	15.22
	# tests	2	3	1	2	4	4
	Max.	318.9	318.5	-	367.3	358.2	322.3
	Min.	307.1	310.3	-	360.2	285.8	286.8
HAZ	Mean	318.5	324.3	299.6	336.2	319.4	299.6
	Std.Dev.	14.90	6.92	15.97	17.57	18.90	20.85
	# tests	7	11	13	10	9	12
	Max.	331.8	335.9	327.0	361.7	352.3	338.6
	Min.	294.1	313.9	275.4	314.3	293.7	273.1

Table 3-8. F292 (Commercial Flux) Inclusion Chemistry [After Ref. 3].

Element Atomic Percent								Oxide Weight Percent ¹		
Mg ²	Al	Si	S	Ti	Cr ²	Mn	Zr	MnO	Al ₂ O ₃	SiO ₂
	43.95	11.21	0.63	14.97		27.18	2.06	21.99	59.98	18.03
	47.81	12.02	1.54	9.98		27.13	1.52	25.95	57.12	16.93
	46.11	12.28	1.10	12.14		26.50	1.86	23.35	58.34	18.31
	49.81	10.08	2.02	10.29		25.55	2.24	23.00	62.17	14.83
	41.17	10.19	5.01	14.15		27.81	1.66	18.46	63.13	18.42
	50.76	8.35	3.64	11.19		23.02	3.04	15.83	70.50	13.67
	58.57	9.28	0.00	8.49		22.04	1.61	21.34	66.28	12.38
	53.64	10.82	0.22	9.13		25.25	0.93	24.99	60.60	14.41
	52.37	9.50	1.75	9.07		25.15	2.15	23.88	62.71	13.41
	47.81	7.95	2.90	12.53		26.90	1.91	21.82	65.37	12.81
	***	***	***	***		***	***	***	***	***
	53.44	9.63	1.67	10.31		22.53	2.43	18.47	67.25	14.28
	48.66	8.54	1.74	11.73		27.56	1.77	25.03	62.12	12.85
	48.70	9.81	2.32	9.48		27.28	2.41	26.33	59.53	14.13
	51.51	10.27	3.08	8.24		25.56	1.34	23.75	61.74	14.51
	53.04	7.77	0.07	12.74		23.22	3.15	18.89	69.17	11.94
	47.75	10.63	1.01	11.92		25.30	3.40	22.21	61.62	16.17
	46.07	10.47	1.04	13.06		26.93	2.43	23.41	60.41	16.18
	52.51	9.26	1.14	10.05		24.77	2.26	22.95	63.79	13.26
	57.46	9.88	1.86	5.15		25.09	0.57	26.69	60.96	12.35
Average										
0.00	50.06	9.89	1.72	10.77	0.00	25.51	2.04	22.54	62.78	14.68

1- assumes all S in form of MnS, all Ti in form of MnO•TiO₂

2- Mg and Cr not analyzed in commercial flux experiment

*** MnS inclusion

Table 3-9. F326 (Base) Inclusion Chemistry.

Element Atomic Percent								Oxide Weight Percent ¹		
Mg	Al	Si	S	Ti	Cr	Mn	Zr	MnO	Al ₂ O ₃	SiO ₂
3.28	49.60	12.06	0.88	8.27	0.72	23.84	1.36	24.26	58.87	16.87
3.94	45.50	14.65	1.30	7.49	0.58	23.25	3.29	24.27	54.89	20.83
3.40	43.85	16.95	1.91	7.81	1.24	24.31	0.52	24.13	52.12	23.75
3.11	42.95	15.96	2.00	8.93	0.96	25.62	0.46	24.87	52.25	22.88
3.42	45.52	17.53	2.22	5.54	1.25	23.46	1.07	24.82	51.71	23.47
0.32	44.96	13.57	2.77	9.54	1.55	25.43	1.87	23.05	56.76	20.19
1.94	51.40	13.01	0.34	8.85	0.63	22.50	1.33	21.72	60.29	17.99
1.83	45.91	13.83	2.66	8.45	1.20	25.68	0.45	24.58	55.66	19.76
2.18	45.55	12.97	3.49	8.22	1.46	25.67	0.45	24.20	56.75	19.05
2.55	49.44	11.63	1.51	7.69	0.86	25.78	0.56	26.76	57.34	15.90
2.95	40.70	15.71	3.75	9.88	0.96	25.49	0.55	21.79	53.75	24.45
3.62	47.45	14.34	1.54	7.21	0.98	24.36	0.50	25.24	55.13	19.64
3.65	43.85	17.02	1.16	7.73	0.67	24.71	1.21	25.62	51.03	23.35
1.99	37.57	16.55	2.42	11.90	2.28	26.97	0.32	23.57	50.31	26.12
1.98	41.55	17.47	1.52	8.70	1.06	27.05	0.68	27.37	48.56	24.07
2.39	49.54	14.29	1.12	7.31	0.94	24.05	0.36	24.67	56.22	19.11
1.81	46.71	15.43	1.48	8.88	0.83	23.34	1.52	21.77	56.31	21.92
2.67	39.19	15.71	2.15	10.18	0.75	28.56	0.79	28.13	48.81	23.06
3.56	44.90	15.27	0.93	8.07	0.70	25.08	1.50	26.24	52.66	21.11
2.96	46.26	14.57	1.49	7.13	1.17	25.61	0.81	27.15	53.13	19.72
Average										
2.68	45.12	14.93	1.83	8.39	1.04	25.04	0.98	24.71	54.13	21.16

1- assumes all S in form of MnS, all Ti in form of MnO•TiO₂

Table 3-10. F327 (1% MnO) Inclusion Chemistry.

Element Atomic Percent								Oxide Weight Percent ¹		
Mg	Al	Si	S	Ti	Cr	Mn	Zr	MnO	Al ₂ O ₃	SiO ₂
2.53	22.91	24.26	1.54	5.73	0.47	40.99	1.57	47.67	23.28	29.05
2.13	31.11	19.76	2.23	5.34	0.63	36.83	1.98	42.81	32.71	24.49
2.51	29.02	22.59	6.88	4.39	1.74	32.55	0.31	34.73	34.04	31.23
2.48	26.79	24.81	3.42	4.24	0.83	36.84	0.59	42.02	27.72	30.26
0.62	23.54	25.62	3.04	4.33	1.00	41.21	0.65	46.70	23.35	29.95
1.83	19.60	25.88	8.52	4.35	0.85	37.69	1.27	40.80	23.16	36.04
1.34	23.33	23.14	9.11	5.01	1.55	35.99	0.53	37.55	28.79	33.66
1.79	31.01	19.45	1.60	6.52	0.94	36.43	2.27	42.21	33.23	24.56
2.15	31.14	20.04	5.73	5.28	1.52	33.51	0.62	36.38	36.18	27.44
2.59	23.21	23.51	1.84	5.58	0.74	40.85	1.68	47.74	23.82	28.44
1.07	27.46	22.82	3.05	5.45	0.92	39.01	0.22	43.85	28.37	27.78
1.59	28.80	24.09	3.70	4.88	0.93	34.74	1.26	38.89	30.77	30.34
3.00	27.29	23.81	4.08	5.03	1.74	34.39	0.66	38.86	30.15	31.00
1.35	26.69	23.04	5.10	5.37	1.66	36.36	0.43	40.09	29.70	30.22
0.79	21.93	27.75	5.33	3.92	0.58	38.97	0.73	43.08	22.85	34.07
1.74	23.11	26.29	1.77	4.84	0.54	40.31	1.40	46.43	22.88	30.68
1.39	23.03	25.38	1.98	4.68	0.53	41.96	1.04	48.13	22.57	29.31
1.39	26.67	25.53	1.78	4.70	0.67	38.59	0.66	44.05	26.29	29.66
1.54	25.01	24.93	2.04	4.67	0.53	40.48	0.79	46.35	24.67	28.98
1.03	28.00	24.83	3.34	3.92	0.45	37.51	0.92	42.36	28.18	29.45
Average										
1.74	25.98	23.88	3.80	4.91	0.94	37.76	0.98	42.54	27.63	29.83

1- assumes all S in form of MnS, all Ti in form of MnO•TiO₂

Table 3-11. F328 (2% MnO) Inclusion Chemistry.

Element Atomic Percent								Oxide Weight Percent ¹		
Mg	Al	Si	S	Ti	Cr	Mn	Zr	MnO	Al ₂ O ₃	SiO ₂
3.14	30.81	15.05	2.27	4.64	0.75	41.51	1.82	49.79	31.86	18.34
0.76	30.74	18.45	2.26	5.42	1.20	39.18	1.99	45.51	31.92	22.58
1.48	29.01	17.83	4.63	5.67	1.44	39.41	0.53	44.74	32.04	23.21
1.34	12.67	27.38	3.09	13.15	1.08	40.01	1.28	42.40	16.24	41.36
3.43	33.23	15.67	1.30	6.92	0.83	36.09	2.54	42.86	36.73	20.41
2.42	29.61	21.63	5.03	5.97	0.44	32.80	2.10	35.50	34.66	29.84
1.99	36.57	16.97	0.80	5.89	0.86	36.12	0.80	41.99	37.50	20.51
2.28	37.26	13.01	1.90	9.28	1.05	34.77	0.45	38.43	43.62	17.95
1.84	35.21	18.84	3.37	4.35	0.43	35.09	0.87	39.88	36.87	23.25
1.53	32.64	19.85	3.83	5.63	0.72	34.68	1.12	38.51	35.82	25.67
2.09	32.06	20.62	2.71	4.65	0.66	36.55	0.67	41.88	33.06	25.06
2.54	37.18	14.19	0.47	7.95	0.59	36.69	0.38	42.19	39.88	17.94
2.39	34.92	19.11	1.23	5.06	0.70	35.84	0.75	41.72	35.43	22.85
1.19	29.71	24.93	1.15	4.01	0.67	37.64	0.70	43.34	28.49	28.17
2.79	36.30	18.43	0.93	5.65	0.90	33.83	1.17	39.52	37.84	22.64
1.69	27.68	25.13	3.83	4.12	0.72	35.85	0.98	40.39	28.80	30.81
2.36	37.35	17.55	0.59	5.23	0.93	35.56	0.44	41.63	37.57	20.81
0.96	25.58	20.41	7.19	5.94	0.65	37.81	1.48	40.89	30.46	28.64
1.35	29.08	23.17	2.95	3.68	0.89	37.95	0.93	43.59	29.09	27.32
1.75	36.12	17.14	2.31	4.85	1.20	36.03	0.61	41.63	37.43	20.94
Average										
1.97	31.69	19.27	2.59	5.90	0.84	36.67	1.08	41.82	33.77	24.42

1- assumes all S in form of MnS, all Ti in form of MnO•TiO₂

Table 3-12. F329 (3% MnO) Inclusion Chemistry.

Element Atomic Percent								Oxide Weight Percent ¹		
Mg	Al	Si	S	Ti	Cr	Mn	Zr	MnO	Al ₂ O ₃	SiO ₂
0.62	27.48	20.57	2.11	5.94	0.40	41.60	1.28	47.44	27.93	24.64
0.83	24.57	19.84	4.93	5.60	0.80	42.61	0.82	48.21	26.54	25.25
1.90	32.39	18.58	1.59	5.27	0.31	39.25	0.72	45.36	32.60	22.04
0.79	28.23	16.95	4.97	6.53	0.65	40.07	1.81	45.20	32.09	22.71
1.00	29.56	19.59	1.58	5.76	0.26	40.43	1.83	46.65	29.95	23.39
1.16	30.26	21.34	1.27	5.20	0.35	39.14	1.28	45.07	30.00	24.93
0.65	27.61	20.42	1.82	5.99	0.46	42.07	0.98	47.98	27.79	24.22
0.86	23.45	16.47	6.79	7.11	0.34	43.63	1.35	49.11	27.84	23.05
0.50	22.34	16.92	6.69	7.62	0.68	43.78	1.48	49.23	26.82	23.94
0.77	30.95	16.82	4.77	5.69	0.74	39.22	1.04	44.08	34.09	21.83
0.83	30.27	19.34	3.89	4.81	0.71	39.25	0.91	44.48	31.67	23.85
0.65	30.41	21.61	1.85	4.87	0.27	38.96	1.38	44.53	30.19	25.28
0.45	26.15	23.44	1.82	5.13	0.62	41.07	1.32	46.89	25.83	27.28
2.19	29.14	20.34	3.49	4.82	0.55	38.24	1.22	43.95	30.75	25.30
0.71	25.70	21.03	4.48	5.26	0.50	39.43	2.90	45.00	28.00	27.00
1.33	31.42	19.69	1.82	4.59	0.43	39.93	0.80	46.06	31.03	22.92
1.13	31.66	18.07	3.62	5.24	0.59	38.39	1.29	43.69	33.66	22.64
0.61	22.52	15.63	7.88	7.10	0.57	44.70	0.99	50.25	27.37	22.38
1.22	28.51	21.78	3.28	4.88	0.26	39.15	0.91	44.32	29.30	26.38
0.45	28.24	18.90	3.31	5.93	0.66	41.49	1.01	47.04	29.61	23.35
Average										
0.93	28.04	19.37	3.60	5.67	0.51	40.62	1.27	46.23	29.65	24.12

1- assumes all S in form of MnS, all Ti in form of MnO•TiO₂

Table 3-13. F330 (0.5% CeO₂) Inclusion Chemistry.

Element Atomic Percent								Oxide Weight Percent ¹		
Mg	Al	Si	S	Ti	Cr	Mn	Zr	MnO	Al ₂ O ₃	SiO ₂
2.27	40.98	10.34	3.91	11.53	0.97	29.02	0.97	26.22	56.87	16.91
1.75	38.54	12.49	3.47	13.01	1.04	28.42	1.27	23.78	55.16	21.07
3.18	51.74	11.30	1.05	6.42	0.37	25.11	0.83	27.39	57.74	14.86
2.82	54.14	11.73	0.43	5.31	0.68	24.04	0.85	27.25	57.95	14.80
3.05	55.10	12.26	0.62	4.33	0.96	23.42	0.27	26.98	57.85	15.17
3.37	50.78	9.74	2.89	7.63	0.59	23.60	1.41	22.62	63.11	14.27
2.72	42.58	6.86	2.47	11.56	0.89	31.35	1.58	32.23	56.95	10.81
2.38	43.38	9.37	6.12	10.22	0.68	26.17	1.70	20.08	63.70	16.22
4.33	43.99	10.00	2.34	9.02	0.76	26.95	2.60	28.00	56.78	15.21
2.64	48.79	10.61	2.26	7.49	0.64	25.97	1.61	26.91	58.18	14.91
1.88	51.80	11.34	4.51	5.35	0.25	23.28	1.60	22.27	61.79	15.94
2.55	39.42	10.47	2.57	13.98	1.72	29.06	1.23	25.17	56.99	17.84
2.30	48.21	9.96	1.04	10.28	0.62	25.80	1.79	25.15	60.19	14.66
2.89	49.43	8.43	1.96	9.36	0.43	25.98	1.52	25.57	61.97	12.46
2.91	53.13	8.92	0.44	6.66	0.57	26.30	1.07	29.57	58.80	11.63
2.37	49.54	12.65	0.36	7.12	1.07	25.84	1.05	28.39	55.05	16.57
3.33	43.24	8.19	5.88	8.98	0.41	28.70	1.27	26.69	59.93	13.38
2.64	39.96	11.61	10.82	7.96	1.19	23.86	1.96	11.64	65.82	22.54
1.70	50.27	8.44	3.36	10.03	1.06	23.05	2.10	18.25	68.25	13.50
2.60	45.43	9.33	3.51	9.91	0.67	27.00	1.56	25.09	60.31	14.60
Average										
2.68	47.00	10.20	3.00	8.80	0.78	26.13	1.41	24.96	59.67	15.37

1- assumes all S in form of MnS, all Ti in form of MnO•TiO₂

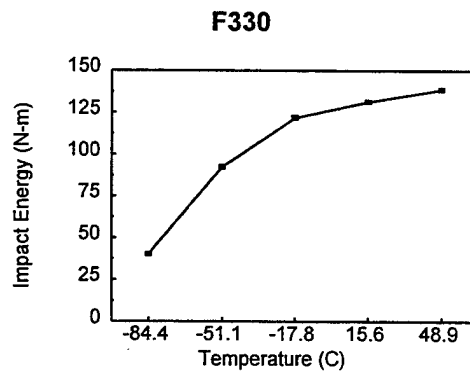
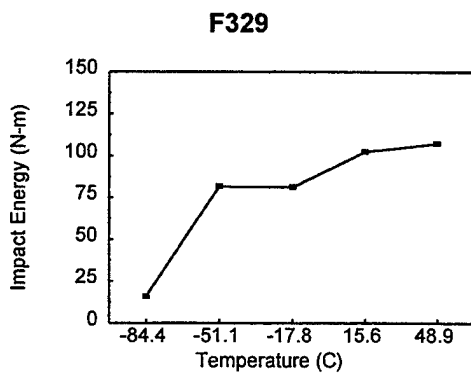
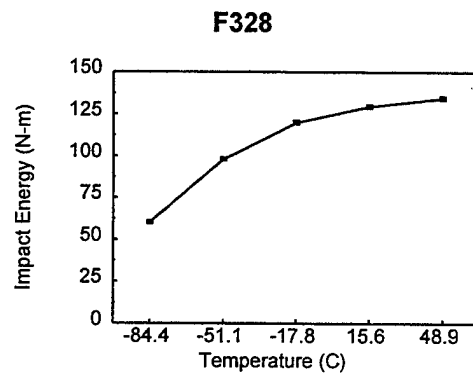
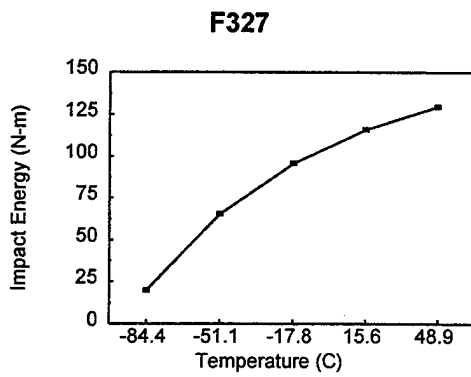
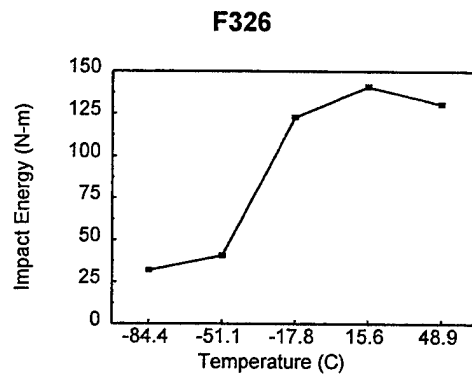
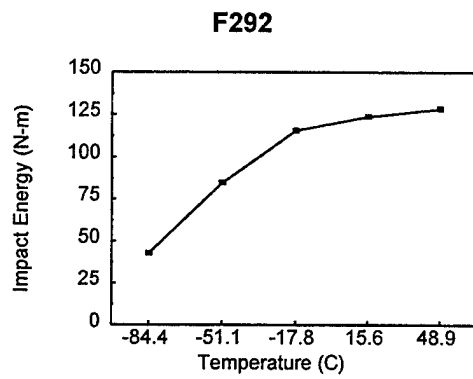


Figure 3-1. Charpy Impact Test Results.

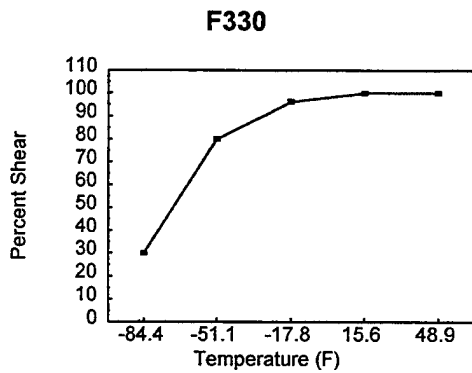
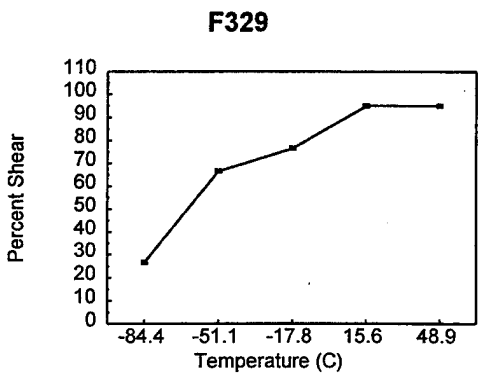
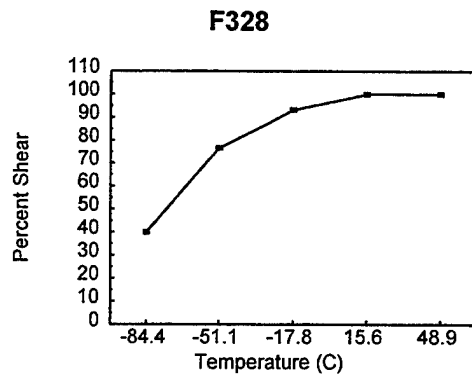
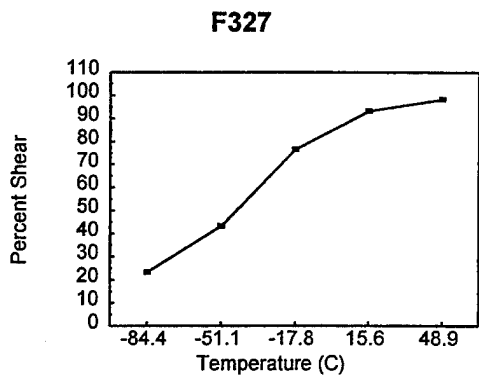
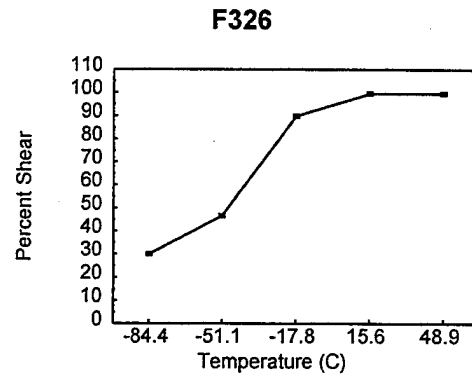
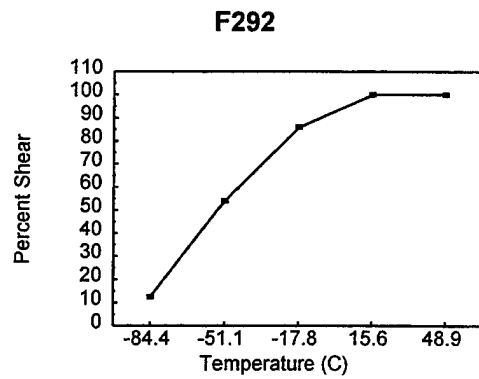


Figure 3-2. Fracture Appearance Test Results.

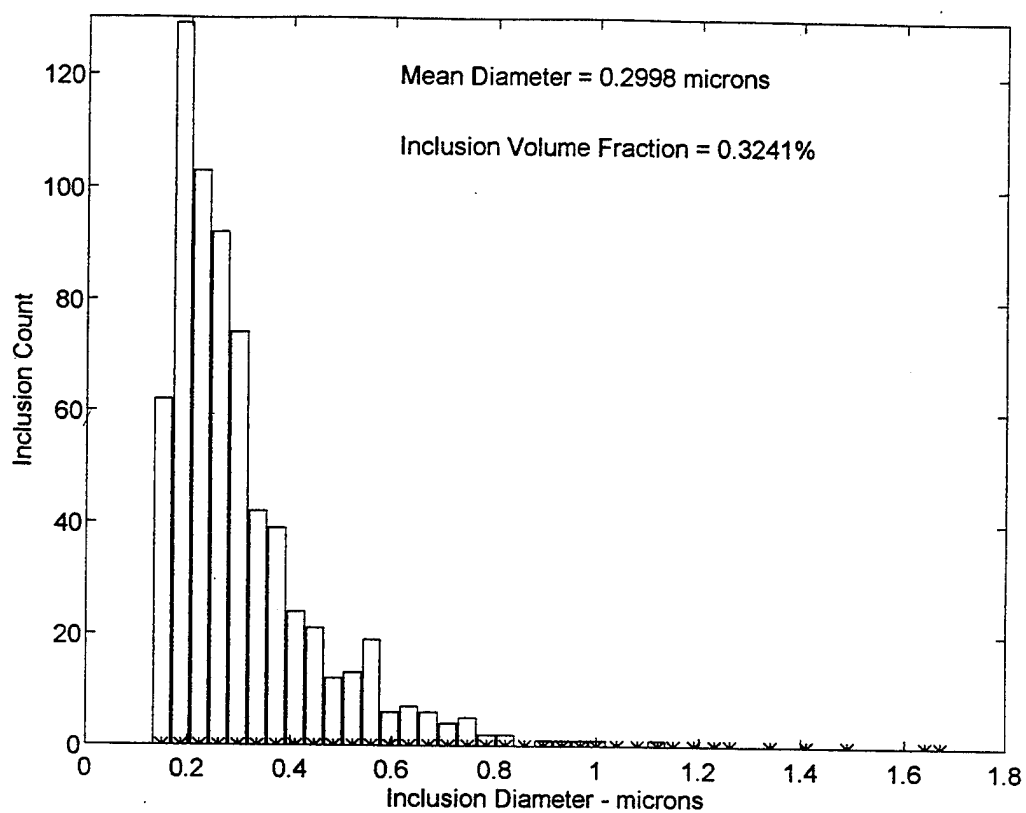


Figure 3-3. Sample F292 Inclusion Distribution.

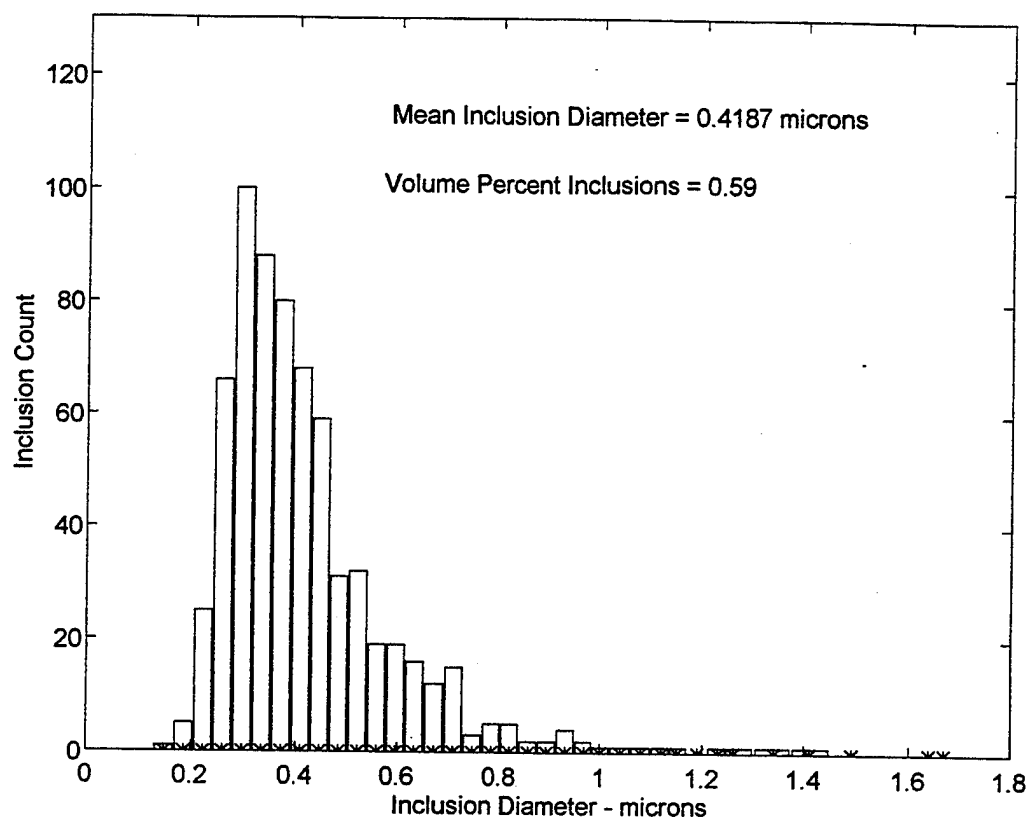


Figure 3-4. Sample F326 Inclusion Distribution.

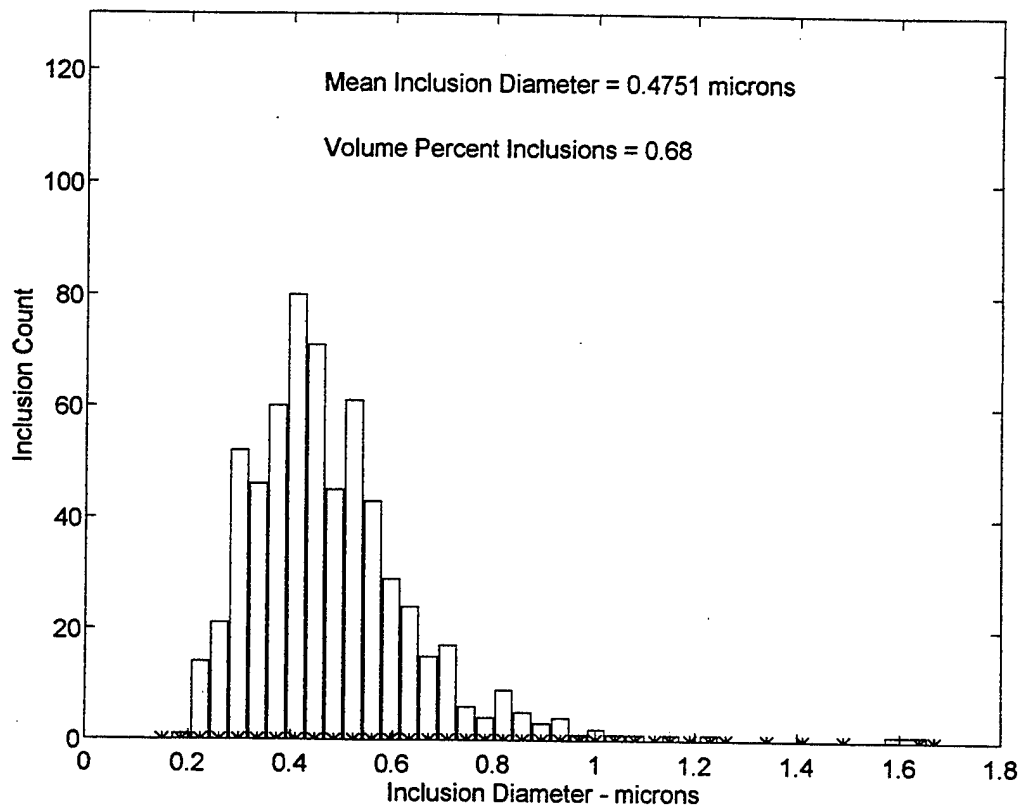


Figure 3-5. Sample F327 Inclusion Distribution.

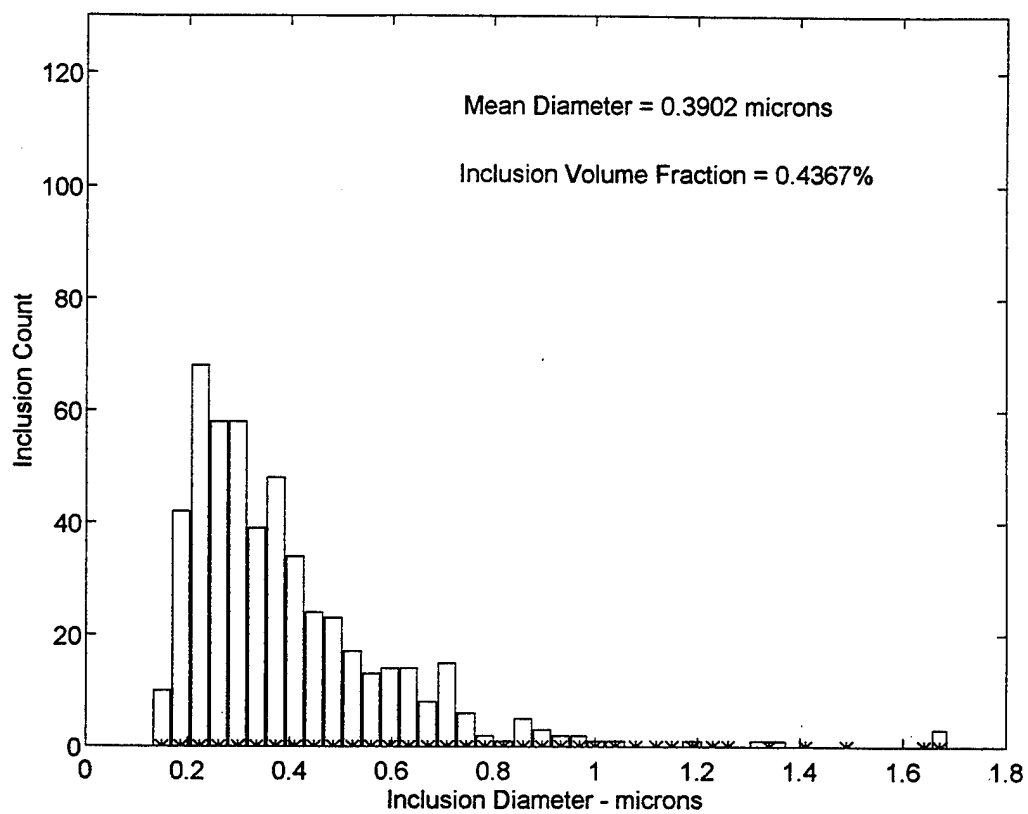


Figure 3-6. Sample F328 Inclusion Distribution.

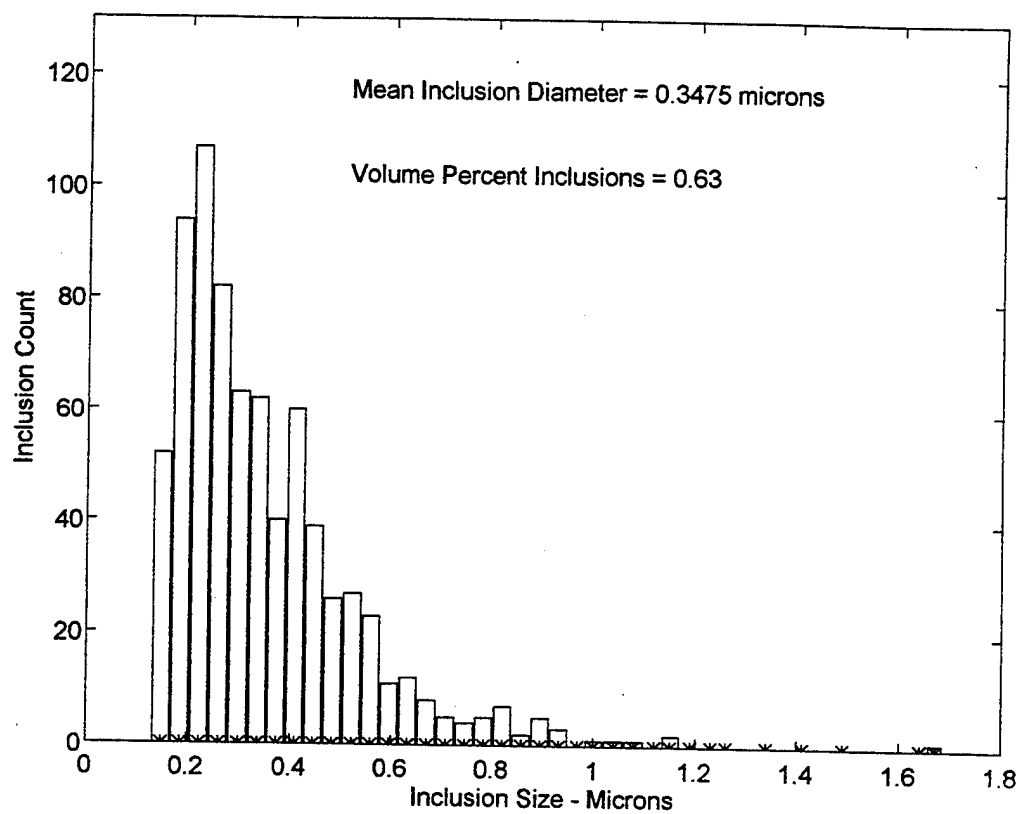


Figure 3-7. Sample F329 Inclusion Distribution.

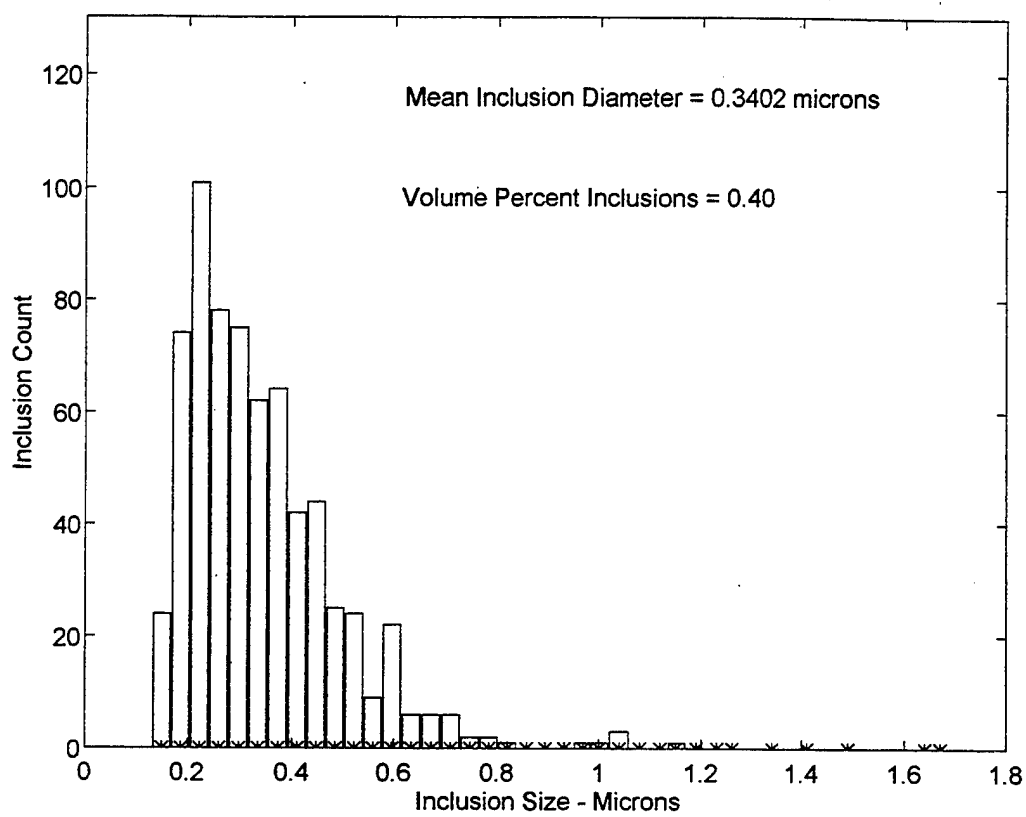


Figure 3-8. Sample F330 Inclusion Distribution.

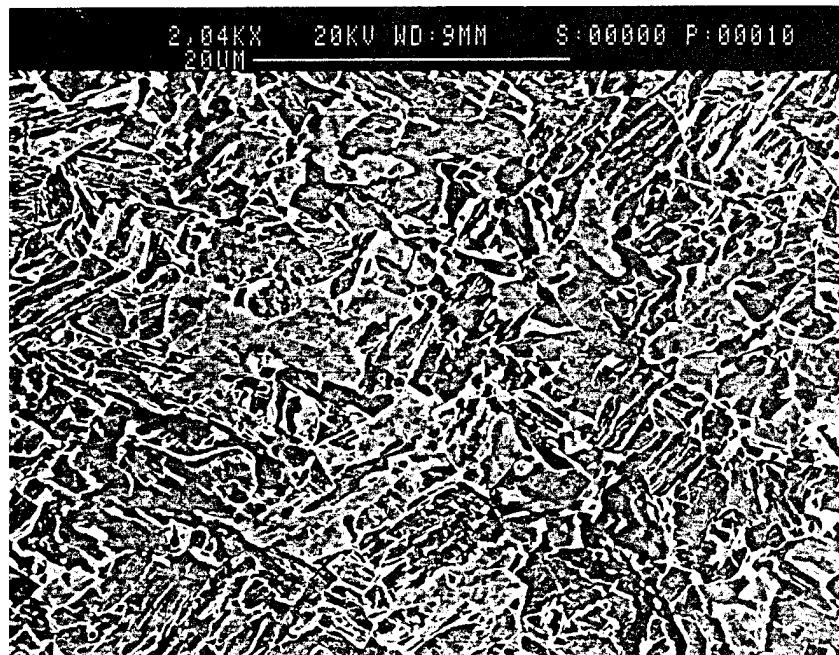


Figure 3-9. F292 SEM Microstructure.

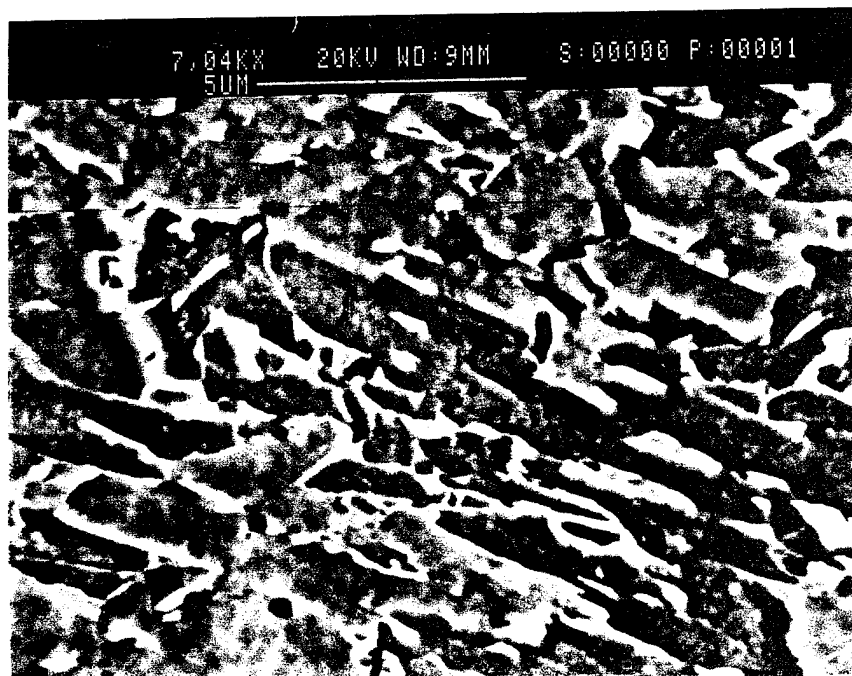


Figure 3-10. F292 SEM Microstructure.

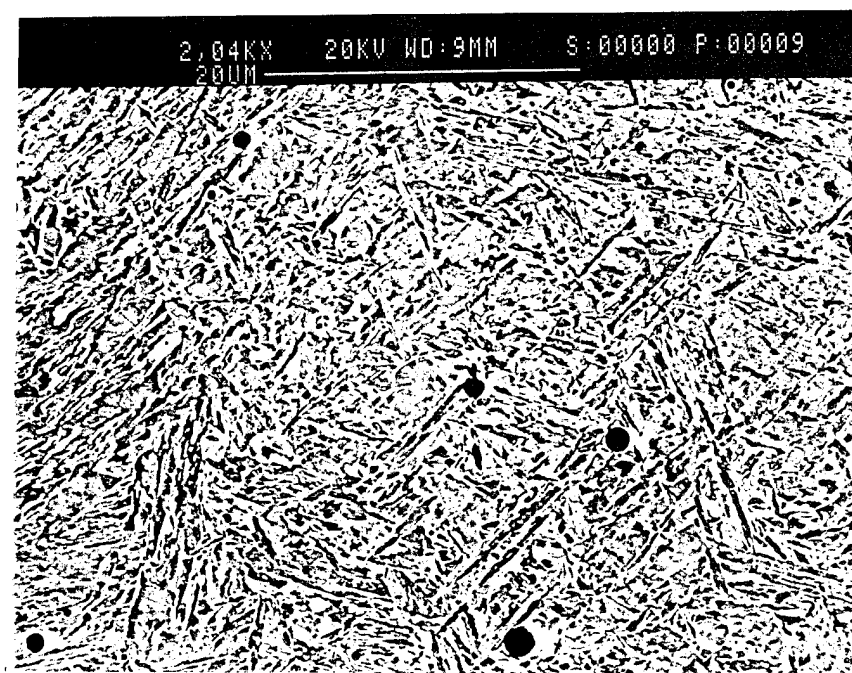


Figure 3-11. F328 SEM Microstructure.

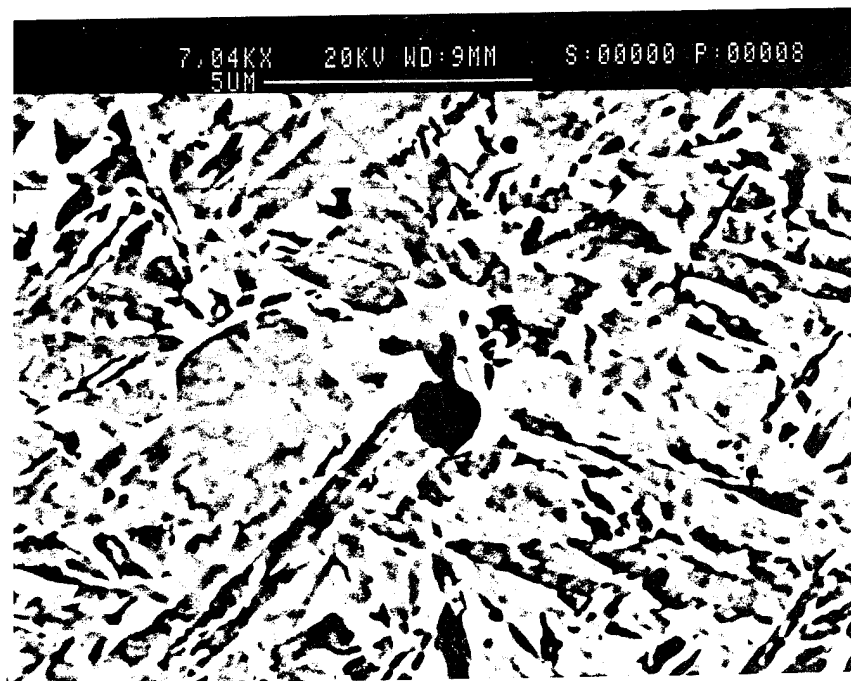


Figure 3-12. F328 SEM Microstructure.

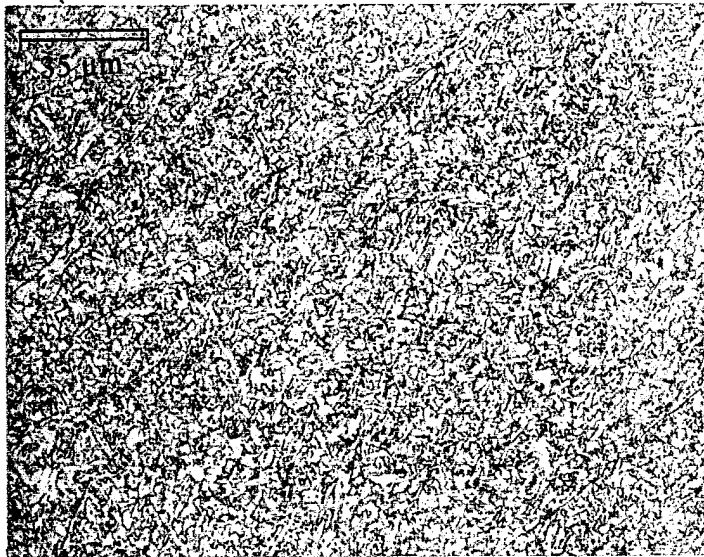


Figure 3-13. Representative F292 Microstructure for Acicular Ferrite Count.

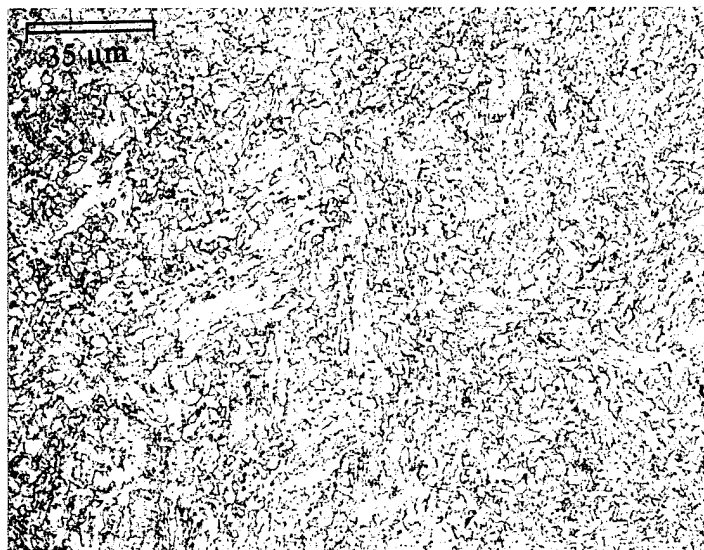


Figure 3-14. Representative F326 Microstructure for Acicular Ferrite Count.

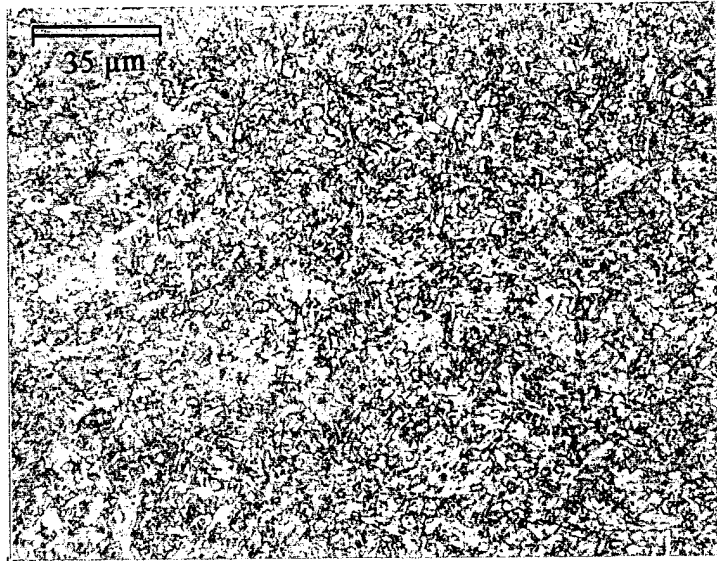


Figure 3-15. Representative F327 Microstructure for Acicular Ferrite Count.

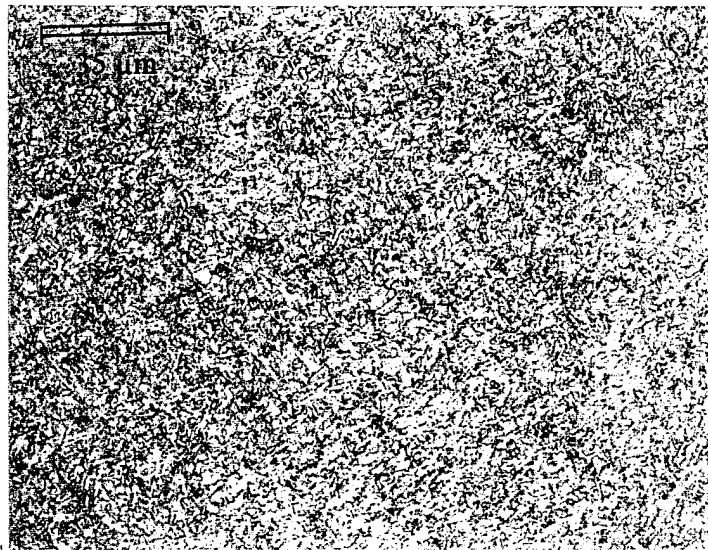


Figure 3-16. Representative F328 Microstructure for Acicular Ferrite Count.

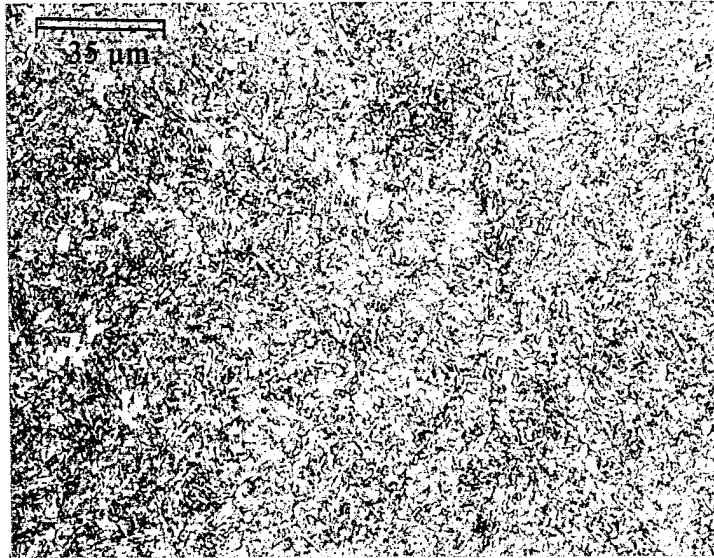


Figure 3-17. Representative F329 Microstructure for Acicular Ferrite Count.

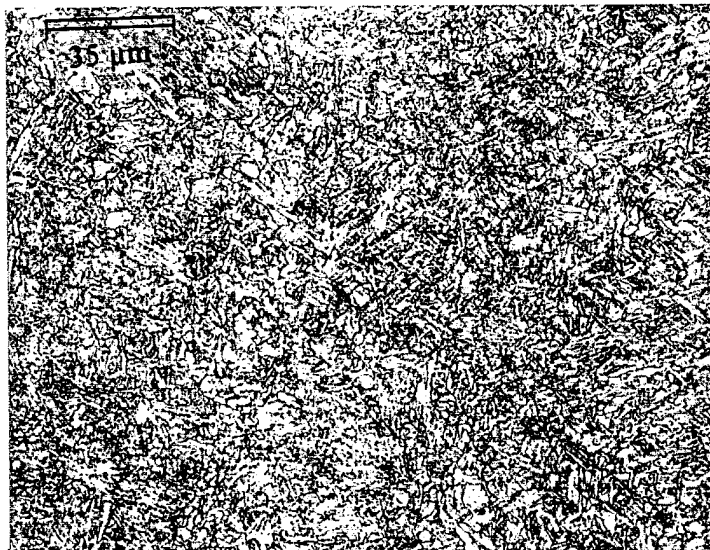


Figure 3-18. Representative F330 Microstructure for Acicular Ferrite Count.

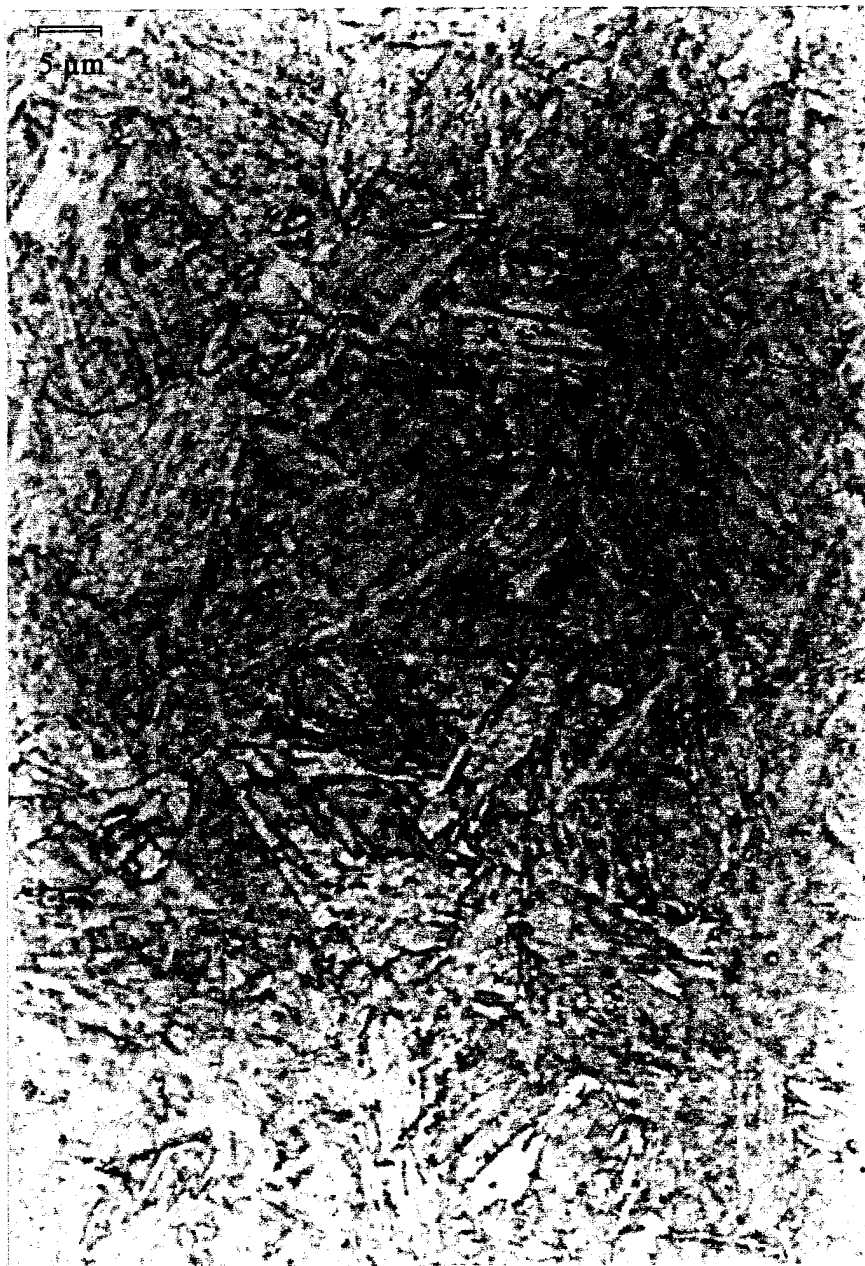


Figure 3-19. Baseplate Microstructure.

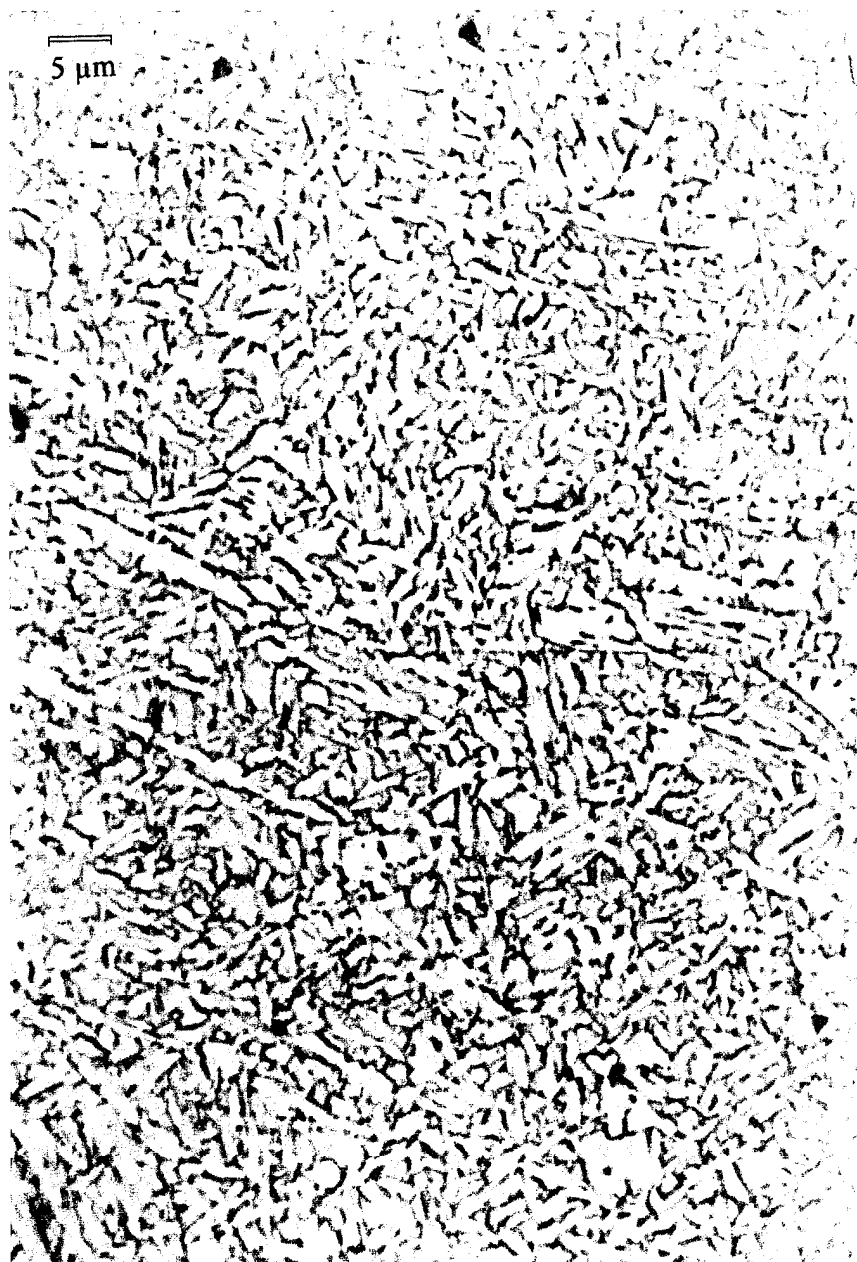


Figure 3-20. F292 Last Pass Microstructure.

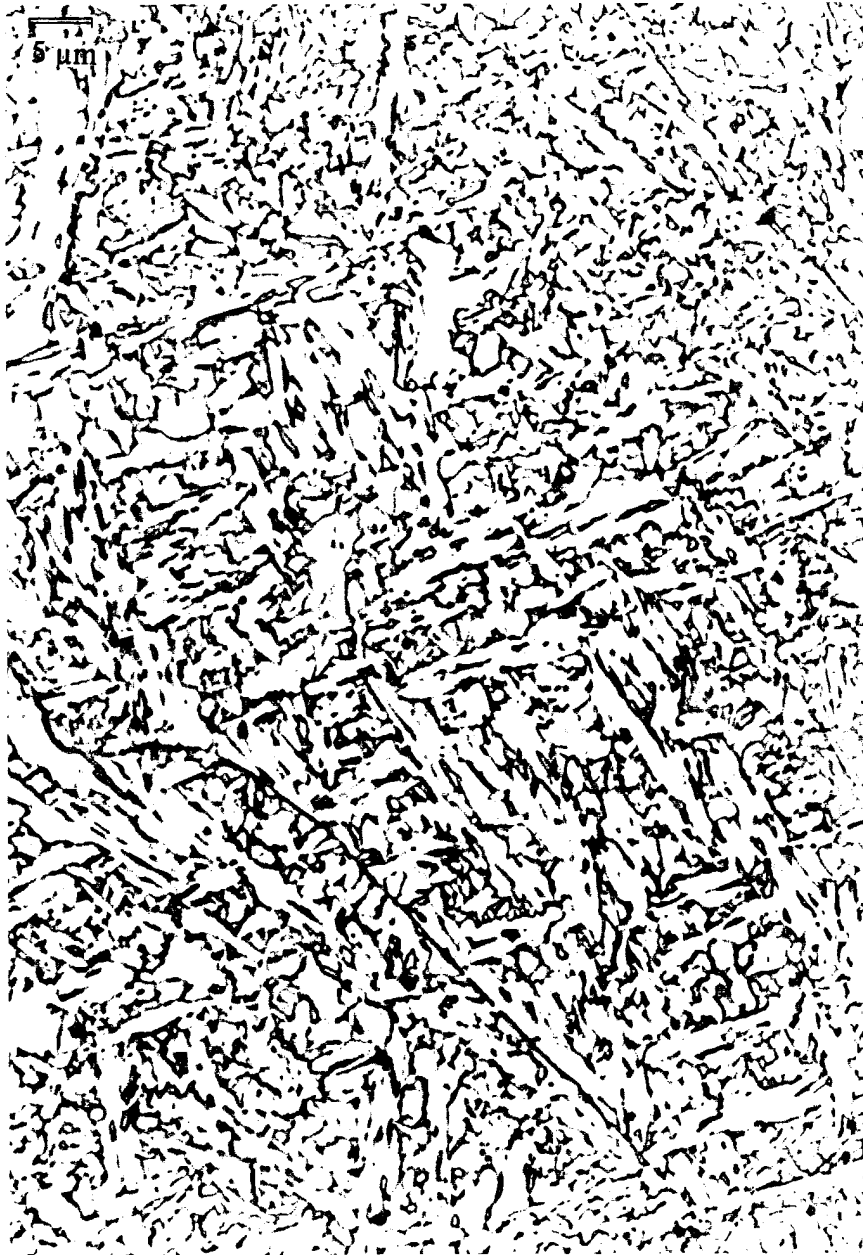


Figure 3-21. F326 Last Pass Microstructure.

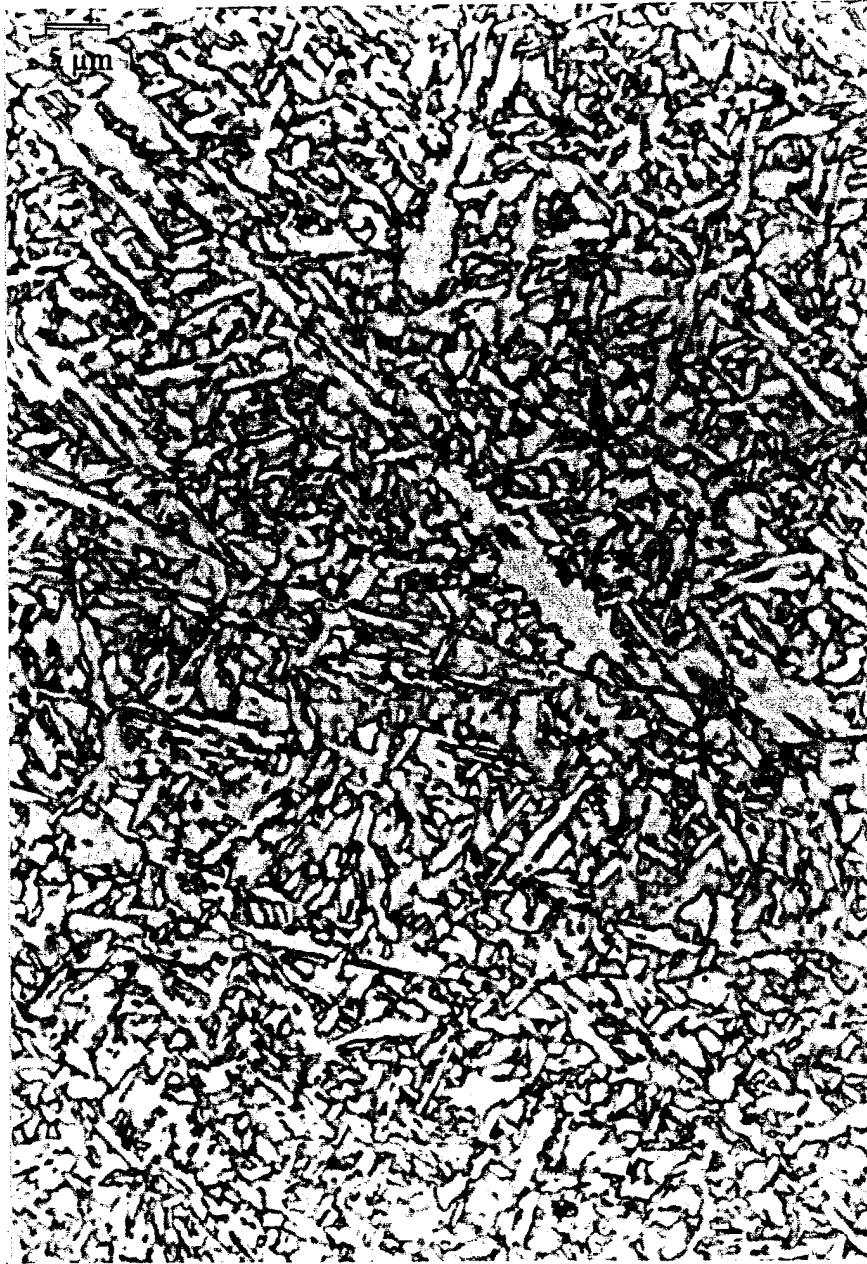


Figure 3-22. F327 Last Pass Microstructure.

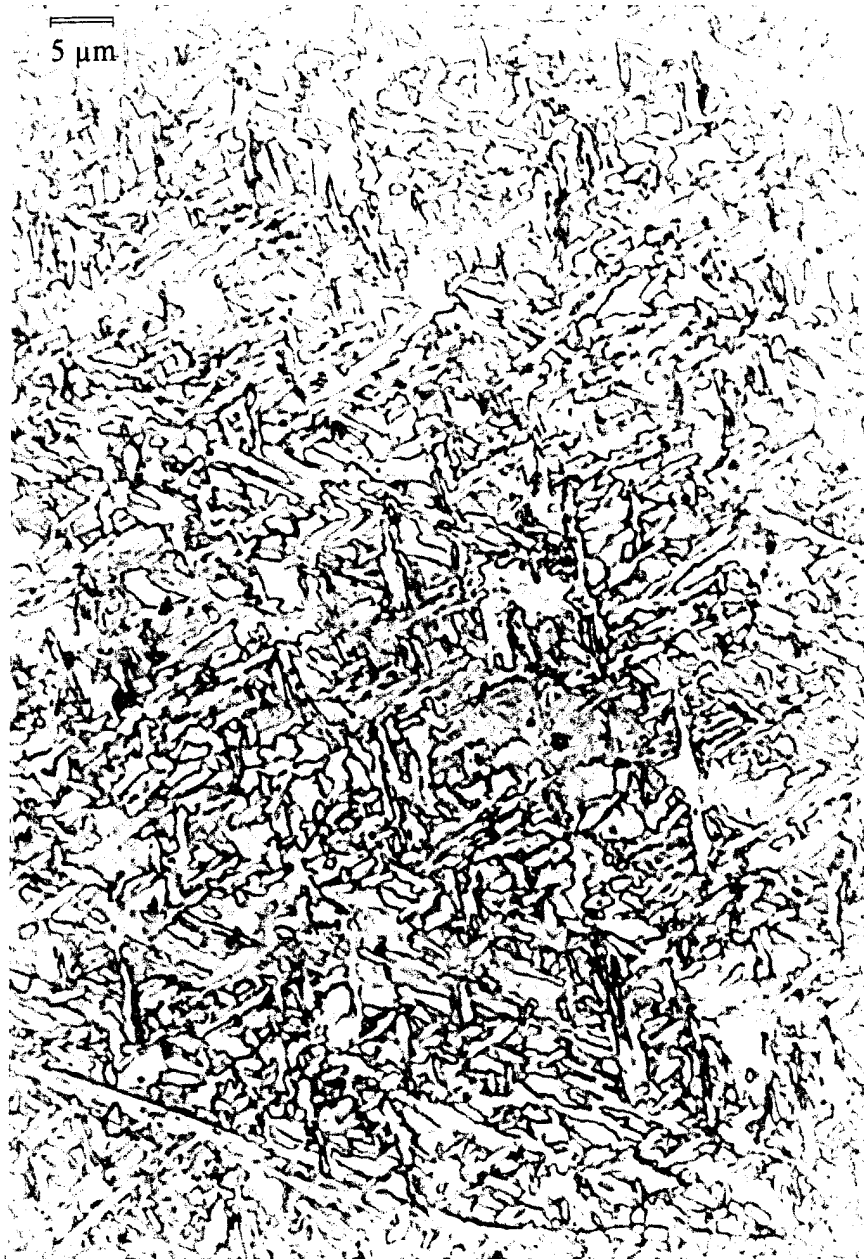


Figure 3-23. F328 Last Pass Microstructure.

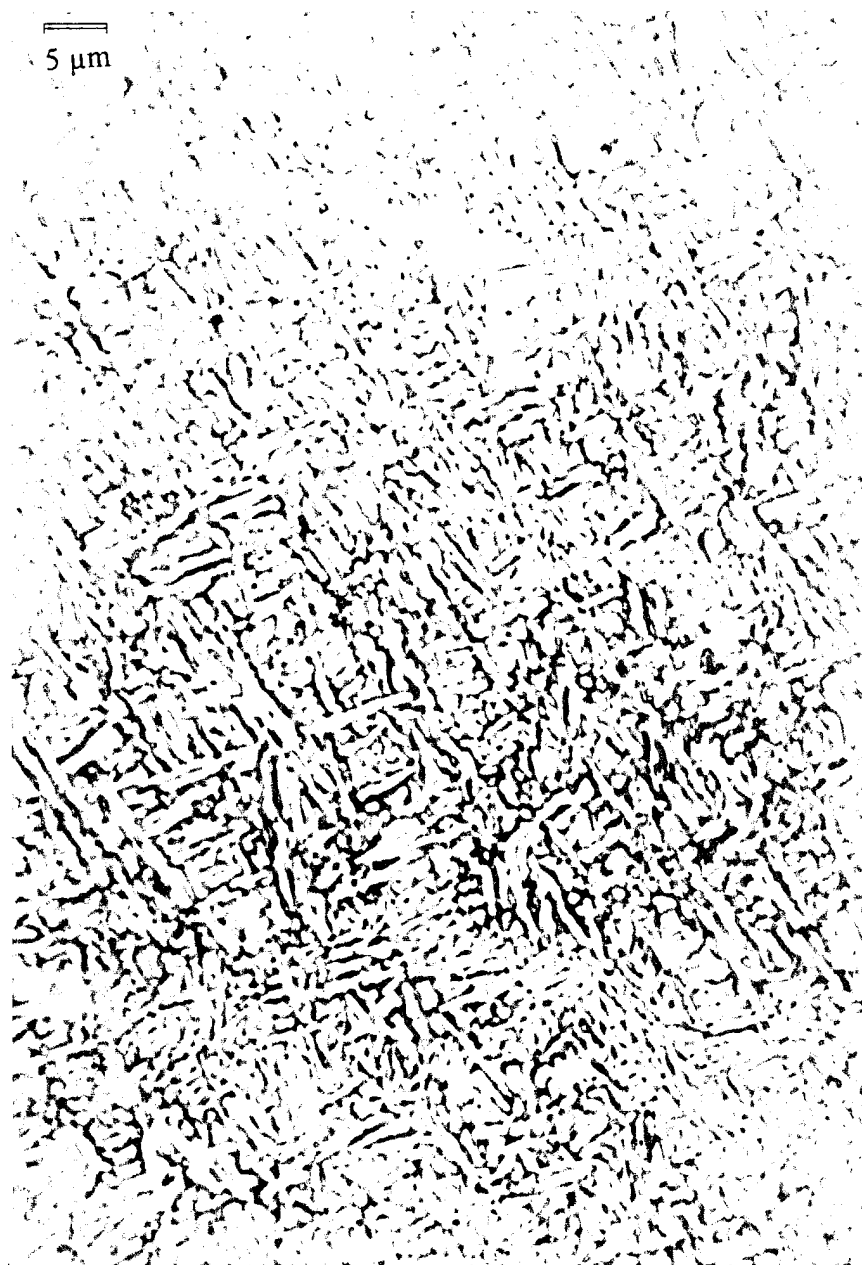


Figure 3-24. F329 Last Pass Microstructure.

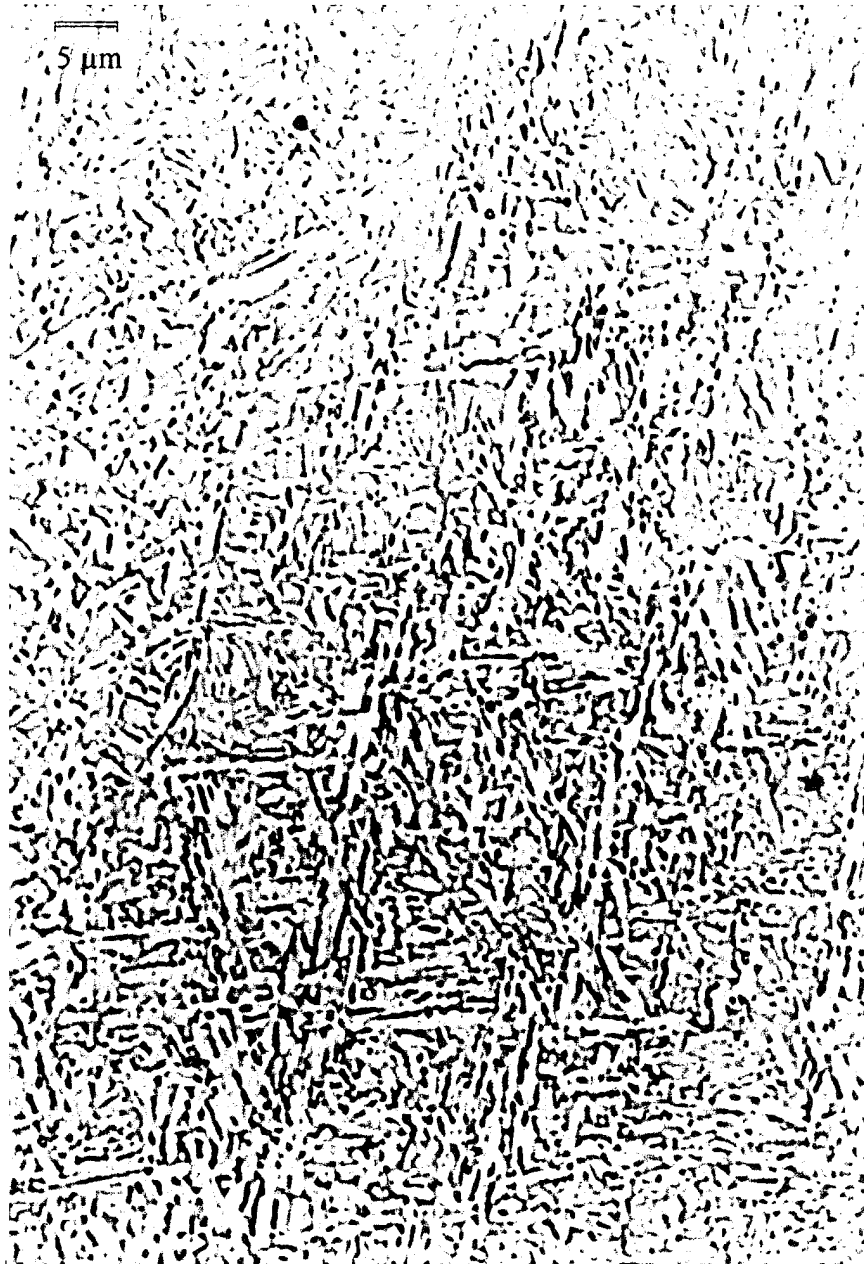


Figure 3-25. F330 Last Pass Microstructure.



Figure 3-26. F292 Weld Metal Coarse HAZ Microstructure.

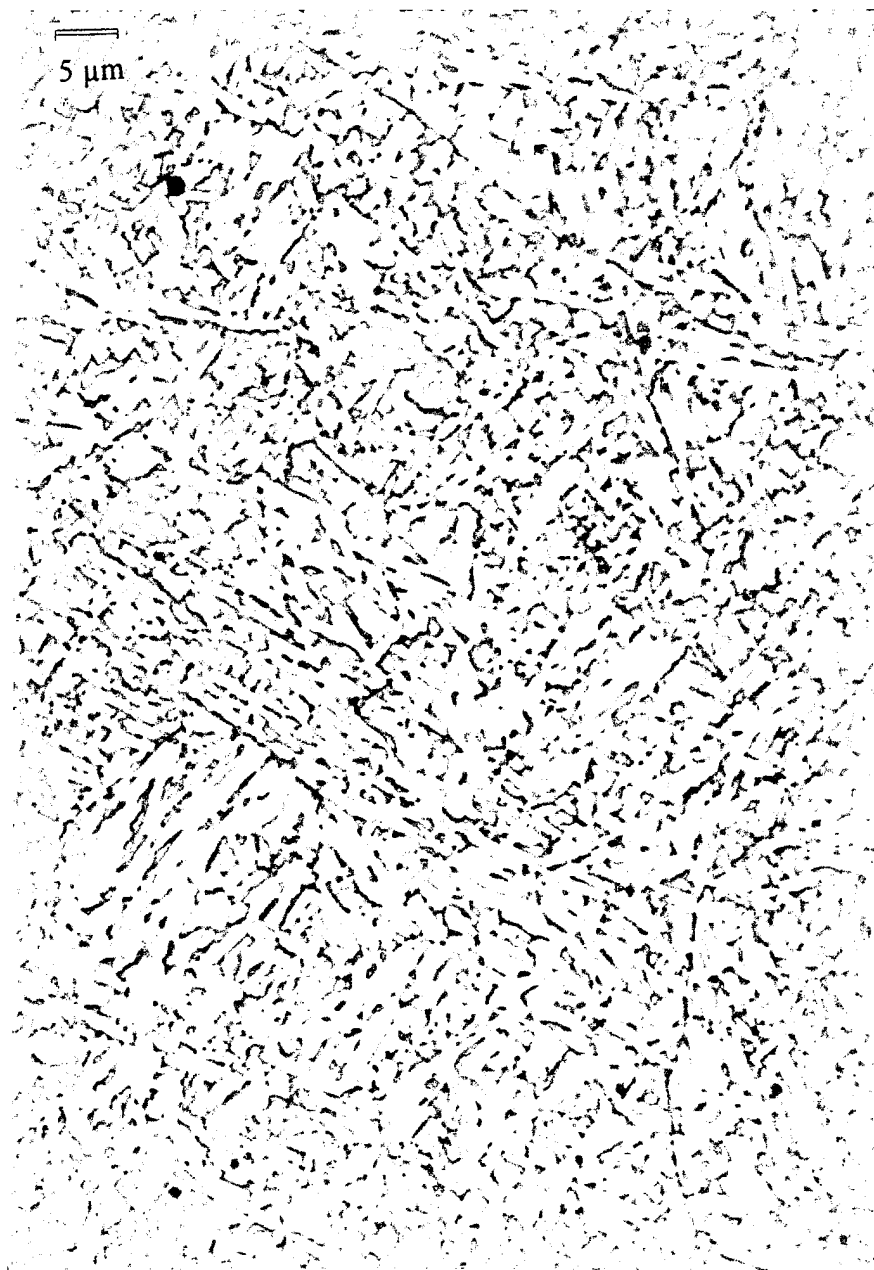


Figure 3-27. F326 Weld Metal Coarse HAZ Microstructure.

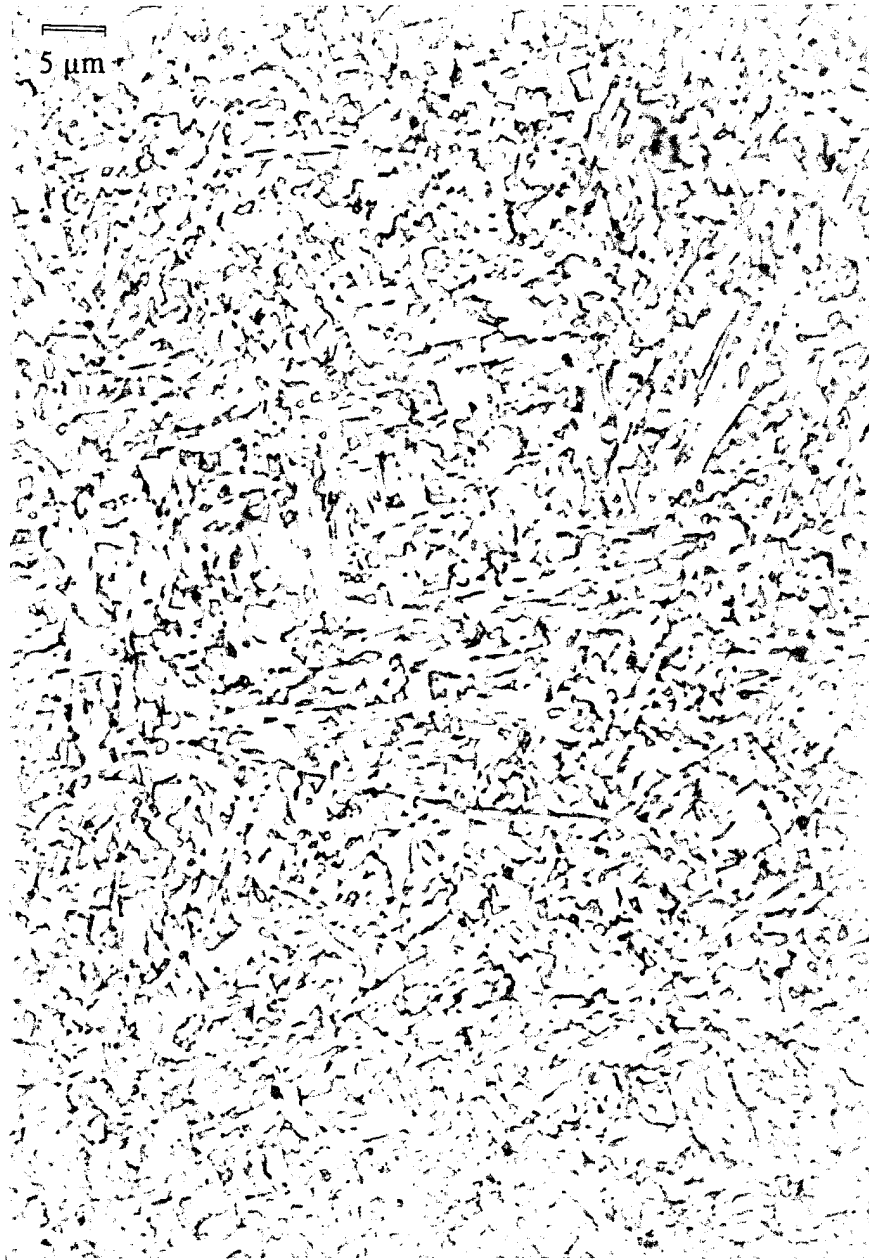


Figure 3-28. F327 Weld Metal Coarse HAZ Microstructure.

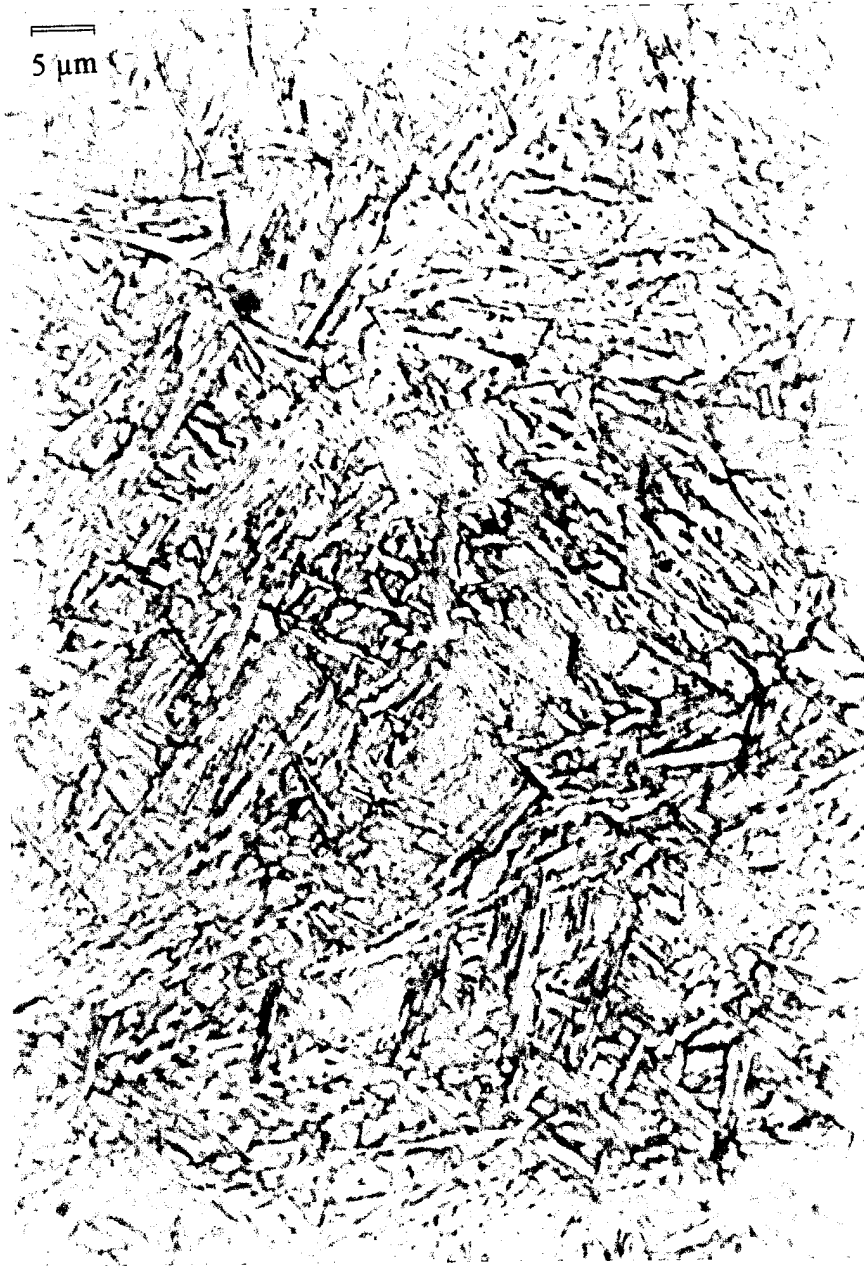


Figure 3-29. F328 Weld Metal Coarse HAZ Microstructure.

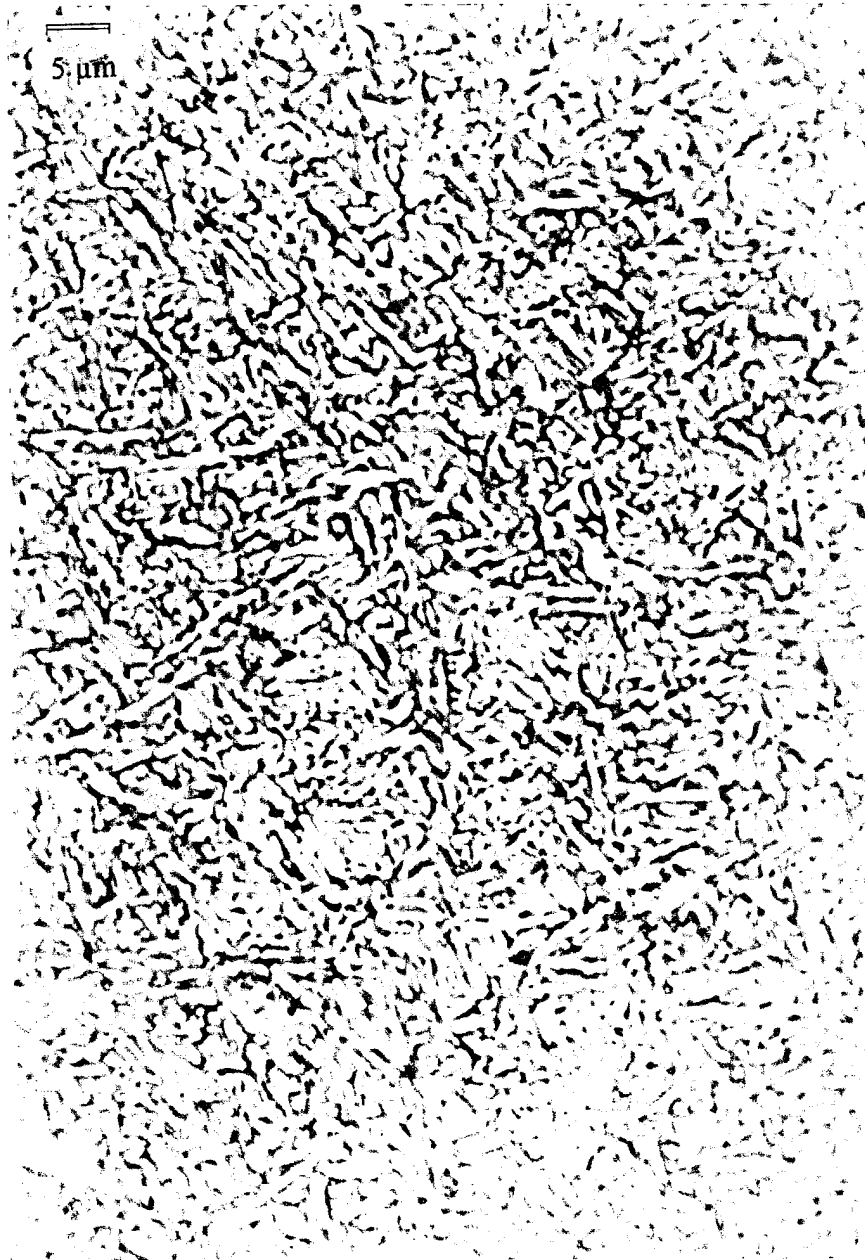


Figure 3-30. F329 Weld Metal Coarse HAZ Microstructure.

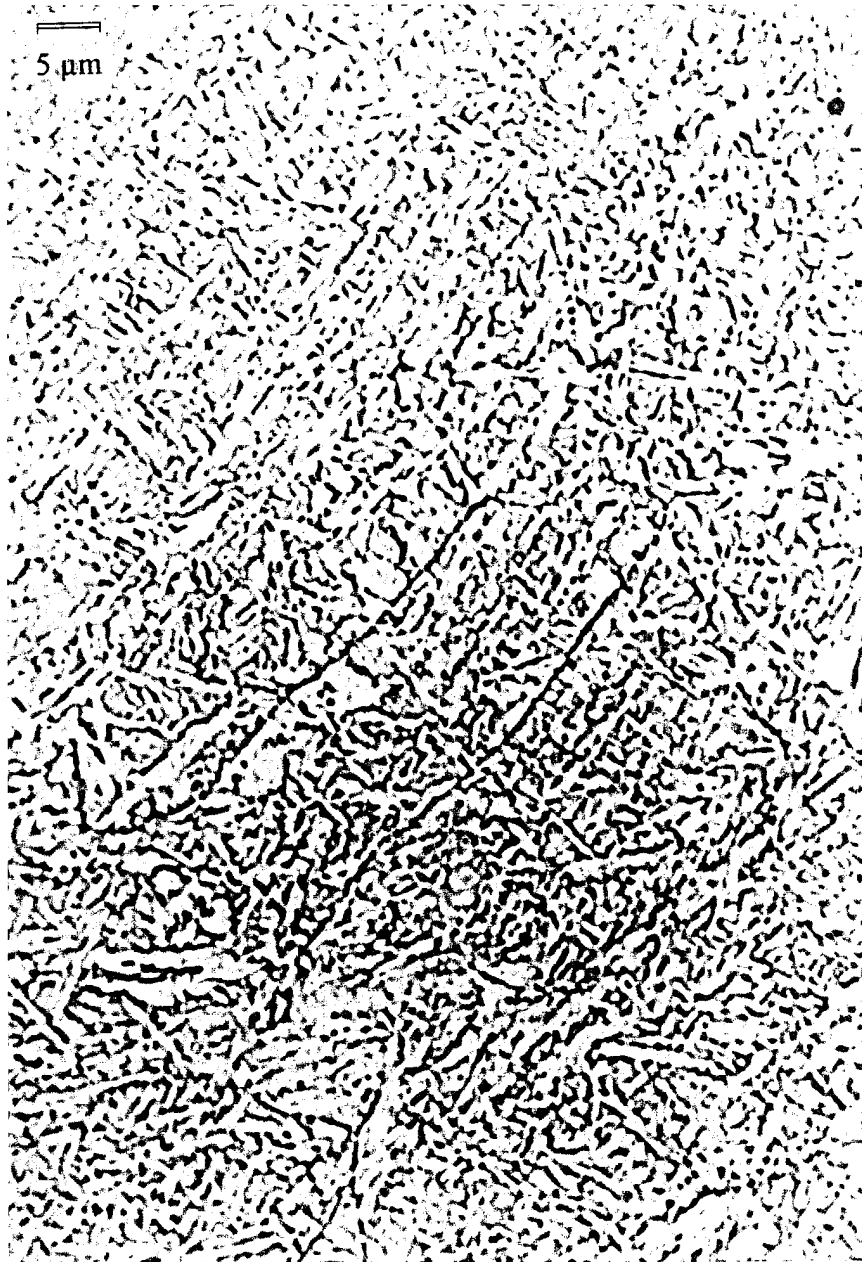


Figure 3-31. F330 Weld Metal Coarse HAZ Microstructure.

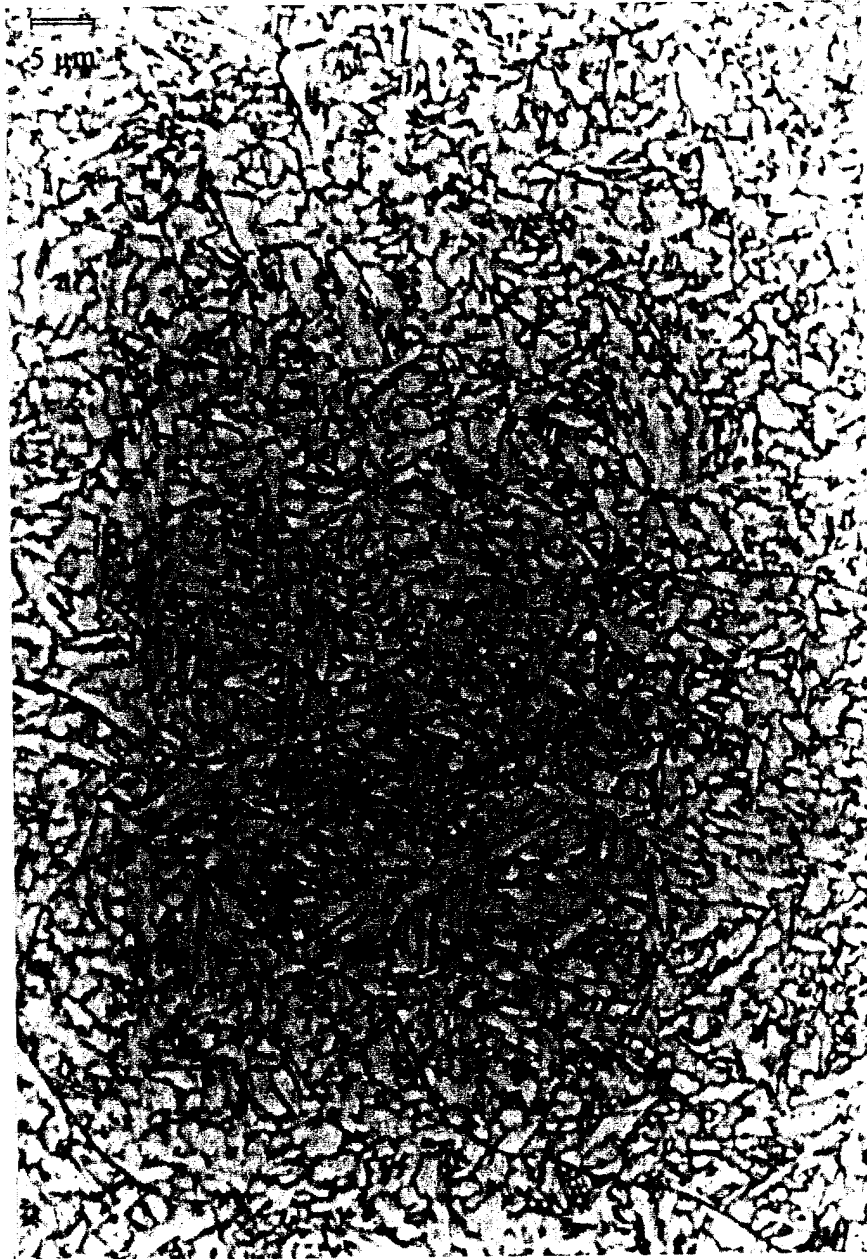


Figure 3-32. F292 Prior Pass Reheated Microstructure.



Figure 3-33. F326 Prior Pass Reheated Microstructure.

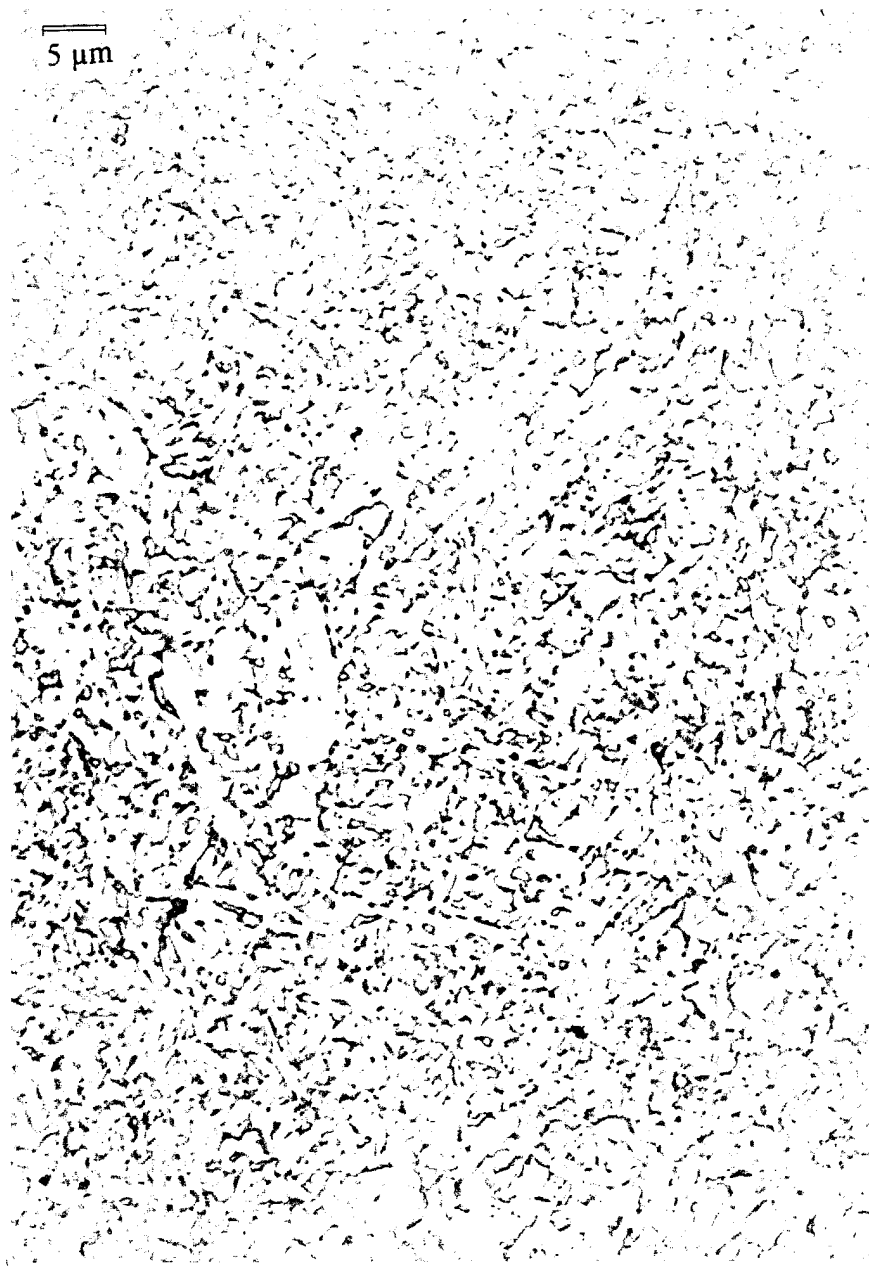


Figure 3-34. F327 Prior Pass Reheated Microstructure.

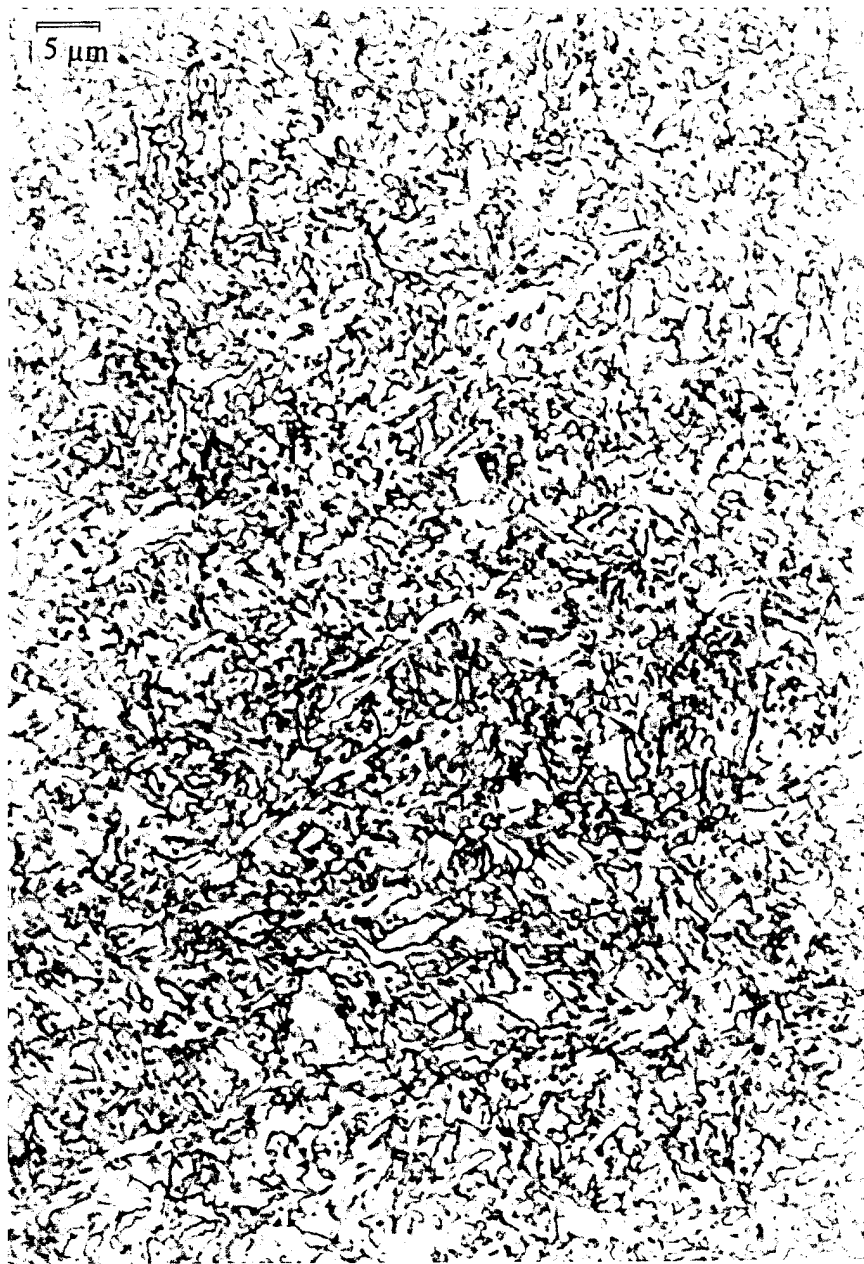


Figure 3-35. F328 Prior Pass Reheated Microstructure.

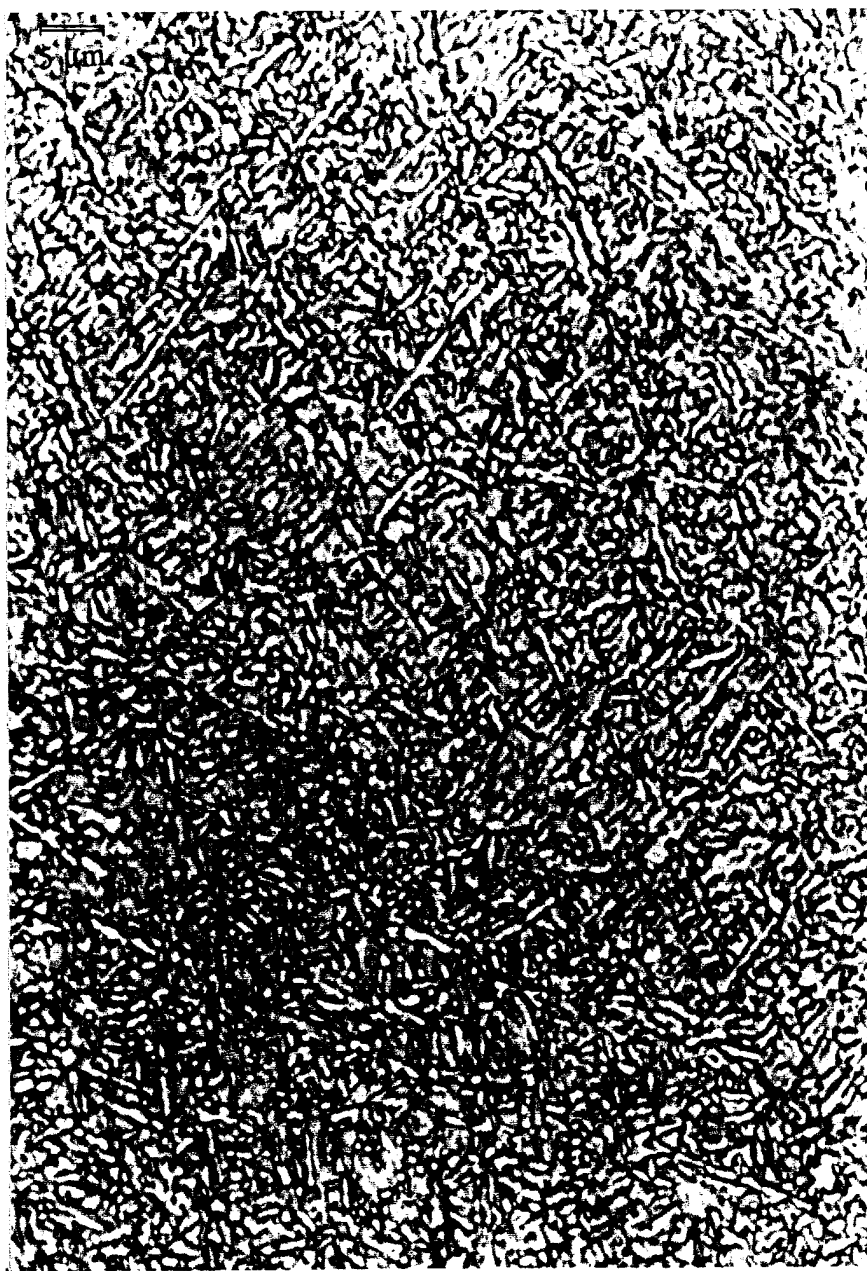


Figure 3-36. F329 Prior Pass Reheated Microstructure.

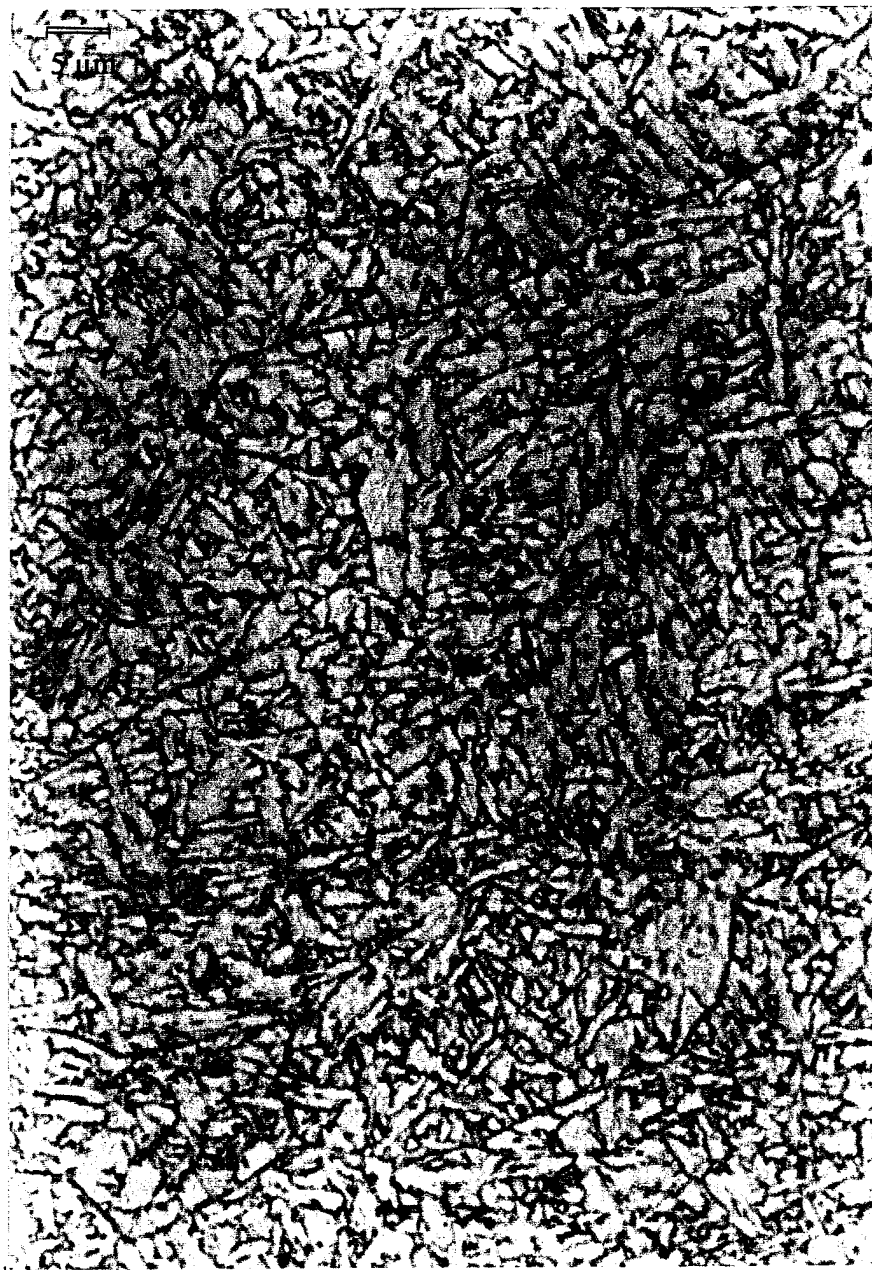


Figure 3-37. F330 Prior Pass Reheated Microstructure.

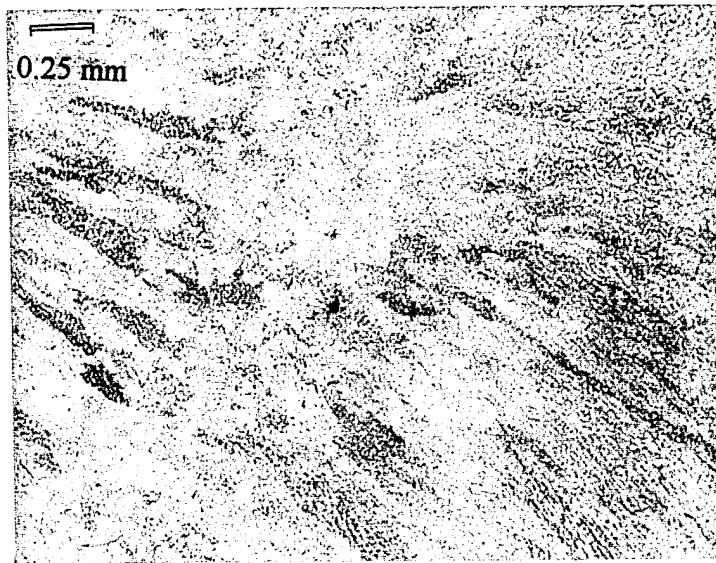


Figure 3-38. F292 Typical HAZ Macrograph.



Figure 3-39. F326 Typical HAZ Macrograph.

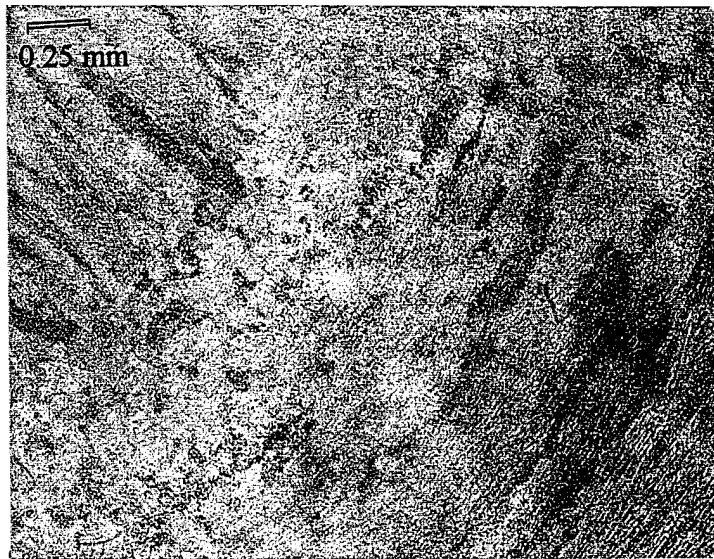


Figure 3-40. F327 Typical HAZ Macrograph.



Figure 3-41. F328 Typical HAZ Macrograph.

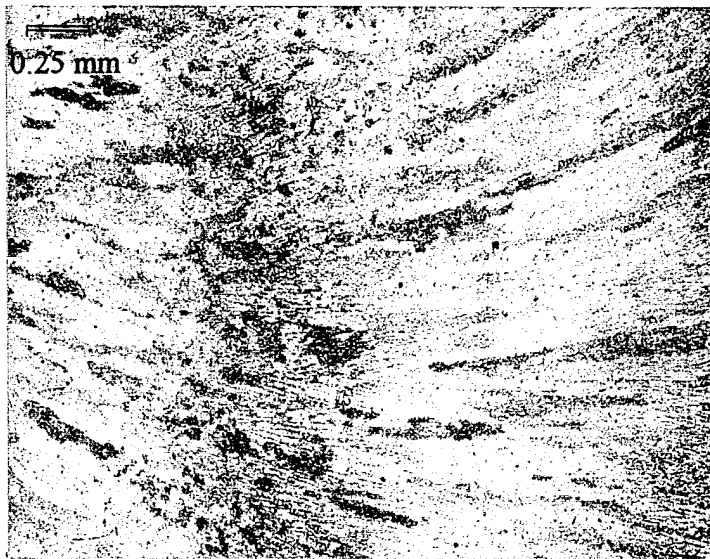


Figure 3-42. F329 Typical HAZ Macrograph.

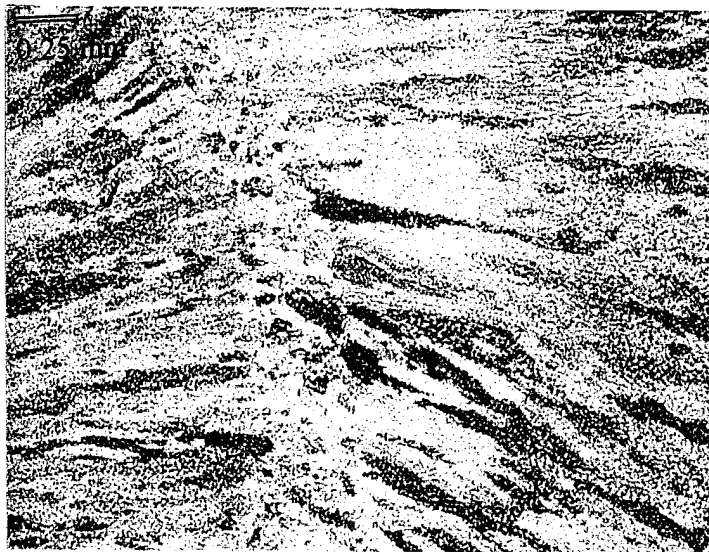


Figure 3-43. F330 Typical HAZ Macrograph.



Figure 3-44. F328 Martensitic Region Macrograph.
M = martensite region
LP = last pass region

0.236 μm

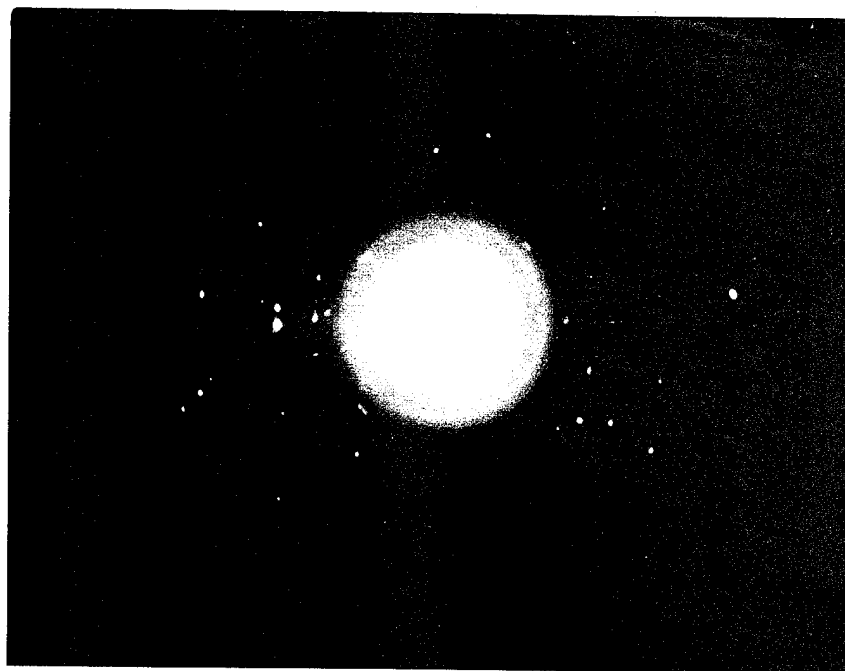


Figure 3-45. A Typical Inclusion and Its Diffraction Pattern.

IV. DISCUSSION

In all the plots shown in this section, the experimental welds produced in the MnO addition series (F326-Base, F327-1% MnO, F328-2% MnO, F329-3% MnO) are indicated by circles. F292-Commercial is indicated by a square and F-330-0.5% CeO₂ is indicated by a triangle, with both appearing on the y-axis in plots against added MnO. All linear regression is performed only on the MnO addition series unless specifically stated otherwise.

A. WELD METAL CHEMISTRY

Figures 4-1 and 4-2 clearly illustrate that addition of MnO to the flux results in a rising Mn content in the weld metal. They also show that the correlation is better when only the amount of MnO added to the dry mix is considered, vice using the "best guess" flux chemistry provided by NSWC and all six weld data. This is due to uncertainty in the chemical analyses, the combining of various analyses into one composite, and in assuming only the constituents listed, i.e. no carbonates. Looking back at Table 3-1, the large changes in CaF₂ and MgO cannot be explained by the flux making procedure, which calls the chemistry results into question. For these reasons the MnO added was the parameter used in comparing the data; flux chemistry was only used when required. This is the same as assuming that nothing occurred in the creation of flux from the dry weighed components

(other than the addition of MnO) that would have resulted in any changes in chemistry. It will be specifically stated when this assumption is not in effect.

Figures 4-3 and 4-4 show weld metal Al and Si versus the amount of MnO added. There is zero correlation between weld metal Al and flux MnO, especially when the 0.002 confidence interval is applied. There is a drop in Si with MnO addition, with a trend similar to the curve shown. These trends support the equilibrium weld metal chemistry thermodynamics espoused by Palm [Ref. 15]. Also in support of his theory, C drops with MnO addition as seen in Figure 4-5. On the other hand, Figure 4-6 shows that oxygen appears to drop slightly with rising MnO, contradicting Palm's conclusion that raising MnO will always lead to a higher dissolved oxygen content in the weld metal. When the 10 ppm. confidence interval for oxygen and the small change in MnO concentration are considered, however, this trend may be weak. The 10 ppm. confidence interval also makes it impossible to determine if there is a positively sloped tail as indicated by the dotted curve. Palm's theory, based on chemical equilibrium (thermodynamics), can therefore at least partially explain trends in weld metal chemistry, but may not accurately predict oxygen. His conclusions about effects on mechanical properties have been superseded, however, by microstructural dependence on inclusions in high strength steels. [Ref. 15]

An attempt was made to compare the results of the present experiment to those of Grong et. al. [Ref. 17] concerning the deoxidation parameter, $([\% \text{ Si}][\% \text{ Mn}])^{-0.25}$, in the hope of determining an approximate temperature for deoxidation in these welds (boundary

between "hot" and "cold" regions of the weld pool). This attempt was unsuccessful due to the small variation in both weld metal oxygen and the parameter when compared to the ranges considered by Grong. Grong's graph of the deoxidation parameter vs. weld metal oxygen appears as Figure 4-7. All the points calculated from this experiment fall on a single point on his graph (1.11,0.028) with a temperature slightly less than 1800°C. Data scatter made it impossible to try to fit this data using thermodynamic calculations. It is interesting to note, however, that use of Grong's deoxidation parameter would predict the nearly constant weld metal oxygen content observed.

B. INCLUSION CHEMISTRY

It was previously explained that the oxide concentrations in the inclusions were calculated assuming all of the sulfur existed in the form of MnS, and all the titanium existed in the form of pyrophanite ($\text{MnO} \cdot \text{TiO}_2$). The MnS assumption is reasonable in that MnS has a comparatively high solubility in liquid iron and low solidification temperature when compared to the oxides considered [Ref. 14]. It therefore could nucleate on inclusions during the final stage of weld metal solidification as proposed by Babu [Ref. 13], or could come out of solution with iron by dissolving into inclusion material while it is still liquid, or by precipitating onto solid inclusions as the weld metal solidification front passes. Differences between the first and final two theories above could explain why some inclusions have only a small amount of sulfur, while manganese and sulphur dominate in others. If the

inclusion is in weld metal liquid at the final stage of solidification, it would be expected to have more sulphur. This could also explain why 7% of the inclusions analyzed had sulphur contents significantly higher than those typical of these samples. The pyrophanite assumption is based on the work of Fox and Brothers [Ref. 4] who were able to determine that pyrophanite and probably galaxite, $\text{MnO} \cdot \text{Al}_2\text{O}_3$, were present in HY-100 submerged arc weld inclusions using diffraction in a high voltage electron microscope (HVEM). In any case, both the variation in atomic composition and in assumed oxide composition will be discussed. None of the elements are believed to be contained in nitrides (like TiN), because no nitrogen peaks were noted in the EDX spectra and the oxygen activity in all the weld metals would have been quite high when they were molten.

Figures 4-8 and 4-9 show the changes of inclusion Mn and calculated MnO with the addition of MnO to the flux. It is easily concluded that the addition of Mn via the flux results in an increased manganese activity, and hence more deoxidation products in the form of manganese containing oxides in the inclusions. Similarities in the Mn and MnO content of the inclusions in the 1 and 2% MnO added (F327 and F328) may lead one to question if the TEM samples were not two from the same weld. This is not confirmed by the Al and Si content of the inclusions, which are different considering that the 95% confidence interval for atomic composition is typically less than 1% in each inclusion for the elements analyzed. Local variations in slag content as explained by Chai and Eagar [Ref. 16] could account for the similar Mn and MnO contents of these samples, as could the shape of the curves shown.

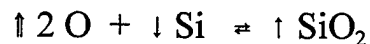
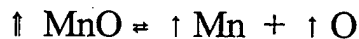
The conclusion that manganese activity (directly related to concentration) is the controlling factor is verified by Figures 4-10 and 4-11 which show inclusion manganese and assumed oxides as a function of weld metal Mn (Figures 4-1 and 4-2 showed the increase of Mn in the weld metal with MnO). The fact that the correlation is better with the MnO added to the flux is probably associated with the relative errors involved in the parameters and the fact that only one weld metal chemistry sample was obtained per weld.

Figures 4-12 and 4-13 show that the aluminum and Al_2O_3 content of the inclusions fall with increasing MnO content in the flux. This could be potentially caused by two mechanisms. First, the Mn could be competing with the Al for the oxygen in the weld metal. An increase in Mn concentration, and hence activity, would make it more competitive, hence aluminum oxides would be replaced by manganese oxides. The favored mechanism is based on Babu et al's work [Ref. 13]. In this case, since the aluminum activity is unaffected by the flux, Al_2O_3 formation would proceed toward completion in accordance with the deoxidation diagram. As favorable temperatures for manganese containing oxides like galaxite are reached, these reactions occur, also in accordance with their deoxidation diagrams. Since, however, the manganese activity (concentration) is higher, more manganese containing oxides will form before equilibrium is reached (an outgrowth of LeChatelier's principle). The reduced aluminum and aluminum oxide contents would therefore be due to dilution: the corundum (Al_2O_3 mineral phase) is enclosed by more galaxite and pyrophanite. The conclusion that more total oxides are formed is consistent with the trend shown previously

in Figure 4-6, that weld metal oxygen tends to fall with MnO addition. It is unfortunate that data scatter precludes strong confirmation or rebuttal of this conclusion. An interesting experiment to verify this theory would be to obtain several TEM photographs of inclusions from each of the various samples and compare the amount of visually distinguishable phases in each inclusion as a function of inclusion chemistry. This is very difficult to do due to the thickness of the inclusions relative to the penetration depth of the TEM, the multiphase and possibly layered irregular shape of the inclusions, and the fact that phase changes may occur under the influence of the electron beam as explained previously, and was not performed in this study.

In contrast to aluminum, inclusion silicon and silicon oxide content rise with the addition of MnO to the flux as shown in Figures 4-14 and 4-15. This cannot be explained on the basis of competition or dilution. Presenting the argument of Palm [Ref.15] in simplified fashion (equilibrium is probably not achieved in the dynamic welding process) the following equations result:

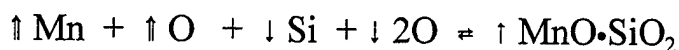
2.



Double arrows indicate the forcing function on each equation and single arrows the trends according to LeChatelier's principle. The weakness of this argument is that there is no notable increase in dissolved oxygen content in the weld metal (Figure 4-6); in fact, the trend appears to be the opposite. A possible alternative which would explain a lowering dissolved

oxygen content would be that a deoxidation product containing both manganese and silicon, like rhodonite ($\text{MnO} \cdot \text{SiO}_2$), forms. The stressed equilibrium equations would be:

3.



If the second reaction has a high enough equilibrium constant that it proceeds sufficiently to the right, the oxygen content of the weld metal will drop. Both of these reaction sequences would result in the lowering of weld metal silicon with increasing MnO which was seen in Figure 4-4. The fact that inclusion silicon is rising while weld metal silicon is falling indicates that a mechanism similar to either of the above is in effect. For example, a ternary oxide based on MnO, Al_2O_3 , and SiO_2 could be forming as long as the aluminum content is low enough to result in the observed aluminum dilution in the inclusion as a whole. To determine the most likely mechanism, thermodynamic calculations for HY-100 along the lines of Babu et al [Ref. 13] are required. These complex thermodynamic calculations are in progress by Babu at Oak Ridge National Laboratory with data supplied from this experiment.

Trace element inclusion content as a function of added MnO to the flux are shown in Figures 4-16 through 4-19. As argued for aluminum previously, the drop in trace element content with increasing MnO could be due to competition or dilution. The Ti in the inclusions falling with MnO addition would tend to suggest that pyrophanite is not a major

constituent in these inclusions, but Table 3-3 seems to indicate that Ti content is lower in the welds with MnO added. These effects could be a combination of dilution of Ti in the inclusion and Ti removal from the weld metal in the slag, with the different effects dominating in the measured parameters.

C. INCLUSION SIZE AND DISTRIBUTION

As discussed in the experimental section, inclusion counts and distributions were hindered by oxide pitting, polishing artifacts, and operator error. It was noticed that slight undersaturation of the SEM filament as well as less than full resolution significantly affected the ability to detect small inclusions (less than 0.25 μm .), and when they were detected they were easily confused with oxide pits and polishing artifacts. When coupled with the low resolution of the CRT screen on this particular SEM, it was decided that data for inclusions less than 0.25 μm . was unreliable, so it was discarded. This should not present a problem for relating inclusions to acicular ferrite formation because only larger inclusions (0.25-0.8 μm .) are believed to nucleate acicular ferrite [Ref. 43]. Above 0.25 μm ., trends could be compared if a sufficient number of fields were analyzed, though by throwing out the small inclusions the numbers themselves become meaningless. Also, smaller inclusions which may be responsible for Zener grain growth pinning are not counted. Due to these experimental difficulties, it is recommended that future inclusion size and distribution analysis be conducted on a TEM or using SEM image analysis on carbon extractions [Ref.

44]. (The SEMICAPS image analysis system recently installed on this SEM might be useful if it can distinguish polishing artifacts. Electropolishing may be an option.)

Another problem with the inclusion distribution determination was the use of random sampling. The way the sample was conducted was to place a polished sample in the SEM with the outer portion of the weld masked with copper tape. Fields were taken at random by selecting a point, then taking several fields in a line from that point, then selecting another point. Since the inclusions are not scattered at random throughout the weld metal (some were pushed to δ -ferrite grain boundaries), this has the potential to introduce error. A better approach may be to uniformly sample the selected area of the weld.

Figures 4-20 through 4-22 show the variation of inclusion size, volume fraction, and number with MnO addition to the flux. It is clear that the inclusion size is increasing with the addition of MnO. This is further evidence that the addition of Mn causes more deoxidation, though no trend is apparent in weld metal oxygen with inclusion size due to data scatter (not shown). The inclusion number falls with a weak correlation (0.7) with manganese oxide addition. This could be due to an increased float-out rate associated with larger inclusion size, but it is more likely a result of random sampling vice uniform sampling due to the small effect of Stoke's law [Ref. 17].

The fact that inclusion size increases with flux MnO lends support to the theory that the drop in aluminum and trace element content in the inclusions is due to dilution. This would be further supported by a nearly constant inclusion number with flux MnO. Figures

4-23 through 4-25 show what happens to the inclusion distributions if F292 and F330 are included in the analysis (this requires the use of flux chemistry). The inclusion size trend is still obvious, but now the inclusion count shows no trend. This use of F292 is suspect, however, because other factors like basicity could be in effect.

D. MICROSTRUCTURES

A qualitative look at Figures 3-13 through 3-18 and 3-20 through 3-39 shows that the microstructure in general is finer with increasing MnO added. This is expected because the resulting increase in weld metal Mn slows diffusive processes, limiting the growth of both diffusive and displacive-diffusive transformation products. The low content of Widmanstätten and grain boundary ferrites is a direct result of the high alloy content of these weld metals.

1. Weld Acicular Ferrite

Figures 4-26 and 4-27 show the variation in acicular ferrite with flux MnO and weld metal oxygen. It appears that the addition of manganese has a strong relationship with the fraction of acicular ferrite (correlation = 0.9714). When the 95% confidence interval for acicular ferrite per Equation 1 is calculated, however, it is seen to be about $\pm 4\%$. So, this trend could be due purely to chance, but the high correlation makes that doubtful. A regression analysis was conducted ignoring the error involved in measuring the acicular ferrite content. It yielded a 95% confidence interval for the slope of the curve of

1.772±1.493 percent acicular ferrite per percent MnO added. This shows that the addition of manganese oxide probably is related to the increase of acicular ferrite, but it is questionable that the relationship is as strong as it appears. A possible explanation for there being less data scatter than expected in the acicular ferrite determination is the use of more than the recommended number of points per photograph. A goodness of fit test could be conducted to verify this. Any trend of acicular ferrite with weld metal oxygen shown in Figure 4-27 is obscured by data scatter in this narrow range of oxygen concentrations.

Figures 4-28 through 4-30 show the relationships between acicular ferrite content and inclusion characteristics. The volume fraction of acicular ferrite tends to increase with inclusion size, and have no relationship with volume fraction or number of inclusions. Theoretically, it would be expected that a larger inclusion size would favor acicular ferrite formation in any of the four nucleation mechanisms previously discussed. It would also be expected that a larger number of inclusions would favor acicular ferrite formation due to an increased number of nucleation sites. Since volume fraction is related to both size and number, it would be expected that acicular ferrite content would closely follow the trend in volume fraction. These effects are either masked by the inclusion distribution experimental problems or Bhadeshia et. al. were correct when they concluded that acicular ferrite formation was unaffected by inclusion population once it exceeds a threshold value [Ref. 18].

2. Individual Areas

The individual area microstructural analyses previously shown in Table 3-6 show few obvious trends. This is believed to be due to selecting only four photographs per region for analysis. Four pictures was probably not enough to adequately sample the range of microstructures found on a traverse of each area. Additionally, Bhadeshia et. al. [Ref. 18] note that the experimental determination of microphase (martensite) volume fraction is very difficult, so it is normally included with the phase that it encloses. In this study, however, there were often well defined regions of martensite due to the high hardenability. This segregated martensite was what was counted, though the definition of "well defined" was subject to operator inconsistency. Use of properly calibrated image analysis equipment is encouraged to allow more sampling, eliminate the cost of photography, and eliminate operator bias and fatigue as influencing factors.

One trend that was noted was that the last pass acicular ferrite content showed the same trend as weld metal acicular ferrite content as shown in Figure 4-31. This tends to support that the operator was unbiased in counting acicular ferrite grid points.

The second trend noted was that the more hardenable weld metals tended to form more martensite in the region where HAZ austenite grain growth obliterated the previous passes columnar grains (referred to as Weld Metal Coarse HAZ in Table 3-6), as seen in Figure 4-32. Since prior austenite grain size was not determined due to experimental difficulties associated with the small amount of grain boundary ferrite, hardenability was

compared using the International Institute of Welding (IIW) carbon equivalent relationship [Ref. 23]. This relationship compares the effect of other alloying elements with that of carbon in an empirical manner. The IIW equation and calculated hardenabilities are given in Table 4-1.

An additional factor which may have confused the results in Table 3-6 is the effect of stress on the acicular ferrite transformation. Bhadeshia [Ref. 30] has shown that externally applied stresses can cause acicular ferrite plates to form with parallel orientations. Much of what was counted as bainite in the F328 prior pass columnar recrystallized region may actually be aligned acicular ferrite (see Figure 3-29). In the higher strength and hardenability welds, the thermal stresses generated by the weld thermal cycle could be expected to be higher if the coefficient of thermal expansion is the same, which it should be based on the small compositional change (strength changes much more rapidly with composition than the temperature coefficient). This would lead to an increased likelihood of acicular ferrite alignment in the higher strength welds, and hence a greater occurrence of misclassifying acicular ferrite as bainite in these welds.

E. MECHANICAL PROPERTIES

1. Relationships Between Mechanical Properties

Since yield strength and microhardness are both measures of the deformability of the weld metal, they should be related, though microhardness is more affected by local variations

in the microstructure. Figures 4-33 through 4-35 show the relationships between the average microhardness in each of the three weld regions considered to the yield strength of the entire weld. It can be seen that the strength of the weld is more closely related to the microhardness of the columnar regions than that of the region where the columnar structure has been eliminated by the large prior austenite grain HAZ. This would support a claim that the columnar regions are more closely related to weld strength. Consideration of the standard deviations in the microhardness data (Table 3-7) weakens the validity of this claim, however.

In this experiment, traditional parameters associated with weld toughness like the 50% cleavage fracture temperature (FATT) did not represent which samples met specifications and which did not. It was found that the area under the Charpy impact energy curve, termed impact area, was able to correctly identify samples that met specifications, and hence it was used as a measure of toughness. Table 4-2 lists the impact areas under each Charpy curve as determined by the trapezoidal rule.

Typically, impact resistance (toughness) falls with increasing strength. Figure 4-36 shows that this may be the case in these welds in an overall sense, but at yield strengths less than 780 MPa the opposite trend may exist. In high strength steel welds, increasing toughness with increasing strength is generally associated with an increasing acicular ferrite content.

2. Mechanical Property - Microstructure Relationships

In the case of the present experiment, Figures 4-37 and 4-38 show that while yield strength does indeed rise with acicular ferrite content, the toughness does not, at least within the accuracy of the point count used. Figures 4-39 through 4-41 show the trends of impact area with inclusion statistics. The weak relationships shown confirm that, if anything, the factors that promote acicular ferrite formation lower the toughness in these welds. This is probably due to the slight increase in acicular ferrite content not being able to offset the effect of having more crack initiation sites or stress concentrators.

Figure 4-42 shows the relationship between the Microhardness of the coarse HAZ and the fraction of martensite. Again, the errors involved in the analysis make any conclusions questionable, but they appear related. Analysis of the relationship of impact area with the coarse grained HAZ martensite content showed no correlation (Figure 4-43).

3. Mechanical Property - Chemistry Relationships

Figures 4-44 and 4-45 show the yield strength and carbon equivalents of the samples against the added MnO. Note that both tend to increase with MnO and have similar shapes. This is the expected trend due to the increase of weld metal Mn with MnO addition to the flux previously shown in Figure 4-2. Figure 4-46 shows that yield strength and carbon equivalent are indeed closely related.

Figure 4-47 shows the variation of impact area with hardenability as measured by carbon equivalent. It is important to note that the two conventional (no cerium addition)

samples meeting Charpy testing specifications have similar hardenabilities. From this, it can be concluded that the hardenability is the controlling factor in the toughness of these samples. One of the results of this moderately high hardenability appears to be the appearance of a fine, possibly tempered or autotempered martensite in the weld metal reaustenitized HAZ formed by subsequent passes in F292 and F328 that is seen in Figures 3-21, 3-29, and 3-44. F328 has relatively large regions of this primarily martensitic structure as illustrated in Figure 3-44. The relatively low carbon content of the weld metal apparently prevents this martensite from adversely affecting the toughness like it so often does if formed in the base plate.

A second result of the moderately high hardenability is that the increase in alloying elements slows the diffusive portions of the acicular ferrite and bainite formation reactions. This results in the finer appearance of the microstructures in the more alloyed welds. It is postulated that the smaller acicular ferrite and bainite plates result in less carbon enrichment of the remaining austenite, and hence a less brittle martensite in the microphase resulting when the transformation from austenite is complete.

Third, the moderately high hardenability results in a lower reaustenitization temperature on subsequent heating as mentioned previously [Ref. 23]. In a similar steel used for pipeline applications, Bhadeshia and Svensson noted that with more alloying the reaustenitized region became larger at the expense of the recrystallized region [Ref. 45], and

that this resulted in more weld homogeneity and hence greater toughness. Figures 3-38 through 3-43 show a similar trend.

F. CERIUM OXIDE ADDITION

Table 3-3 clearly shows that, as expected, the weld metal of the 0.5% CeO₂ weld, F330, is remarkably similar chemically to that of the base flux, F326. Tables 3-4 and 4-2, however, show that in spite of this chemical similarity, the CeO₂ weld shows dramatic increases in both strength and toughness. Table 3-6 shows that the microstructures of the two welds are very similar, the major difference being that the CeO₂ weld has more acicular ferrite and less bainite in the coarse grained re-austenitized HAZ. This could be a result of the proposed lowering of austenite grain boundary energy mentioned previously, which would also result in a lower propensity to nucleate bainite. The effect would be similar to that discussed previously as noted by Babu and Bhadeshia [Refs. 33,46]. In their case, they suppressed bainite formation by eliminating grain boundary nucleation sites by forming thin layers of grain boundary ferrite. This enhanced the formation of acicular ferrite. Another potential effect of CeO₂ addition could be solute pinning of austenite grains, but prior austenite grain size determination was not conducted in this study due to the small amount of grain boundary ferrite present. Obviously, more study must be conducted to explain the mechanism for the favorable mechanical properties observed, but the addition of CeO₂ to welding fluxes shows considerable promise.

G. SUMMARY OF RELATIONSHIPS

1. Weld Metal Deoxidation

The addition of manganese oxide to the SAW flux, resulted in increased weld metal manganese, and decreased silicon and oxygen. The remaining elements showed no trends. In the inclusions, on the other hand, the atom fraction of manganese and silicon both raised, as did the average size with MnO addition to the flux. This indicates that the final stage of deoxidation in these weld metals may be accomplished with the formation of a manganese silicate, possibly rhodonite or tephroite ($2\text{MnO}\cdot\text{SiO}_2$), with a mechanism similar to that shown in Equation 3. This manganese silicate comes out of solution on inclusions previously formed in the weld pool, greatly reducing the activation energy for nucleation. These pre-existing inclusions perhaps contain Al_2O_3 , various titanium oxides, galaxite, pyrophanite, and trace element oxides. The addition of more manganese results in more manganese silicate formation, making the layer of manganese silicate thicker over the inner core produced by previous deoxidation reactions, resulting in larger inclusions. This coating process results in the decreasing atom fractions of Al, Mg, Cr, and Ti noted in these inclusions with manganese oxide addition. Figure 4-48 shows the position of inclusions from several series of welds analyzed at NPS [Refs. 3,5,46] on a ternary phase diagram of the Al_2O_3 - SiO_2 - MnO system, with oxide concentration compositions calculated as explained previously. The position of these multi-phase inclusions would tend to indicate a close relationship between manganese and silicon in the weld metal deoxidation, with

aluminum being more independent. This is consistent with deoxidation theory as espoused by Babu et al [Ref. 13]. Their results on HSLA steels suggest that much of the aluminum in the weld pool is consumed very early in the deoxidation process to form Al_2O_3 and galaxite. Thermodynamic calculations are in progress at the Oak Ridge National Laboratory to help validate this proposed subsequent part of the deoxidation sequence for these weld metals. Of course, there still exists the possibility of reactions taking place within the inclusions after weld metal deoxidation is complete.

2. Microstructure and Mechanical Properties

Trends in microstructure and mechanical properties are much more difficult to locate. In all cases, differences in toughness appear to be a result of microstructural differences in the weld metal HAZ. In the future, one half of the fractured Charpy samples needs to be provided to NPS for fractographic analysis. This analysis should be able to determine the region of the weld in which the crack initiated as well as propagation mechanisms through the various regions. This would greatly enhance the ability to diagnose which features of the weld deserve the most attention, and may allow the improvement of those features which result in poor toughness.

In the absence of fractography, it is believed that the ability of F292 and F328 to meet Charpy testing specifications rests on the presence of a fine, and possibly tempered, martensite in the coarse grained weld metal HAZ of these multi-pass welds in combination with a high acicular ferrite content in the columnar regions of the weld. The high toughness

of F330 is attributed to the austenite grain boundary stabilization provided by the cerium, which lowers the production of bainite, especially in the coarse grained weld metal HAZ in this weld.

In the case of these welds, the variation in weld metal chemistry appears to be more important in shaping the mechanical properties than the proportion of acicular ferrite. This is largely due to the fact that the experimental parameters were set up to yield cooling rates and oxygen contents that resulted in maximum acicular ferrite while following industrial welding procedures. It is interesting that the weld metal manganese content of F328 is about 1.7 %. This is very close to the 1.6% that Grong et. al. found to be ideal in a similar experiment in flux cored GMA welding of C-Mn steels [Ref 48]. Due to the vastly different alloying in the weld metals this is probably a matter of coincidence, but in both cases deoxidation was being controlled with manganese and silicon.

Table 4-1. IIW Equation and Calculated Hardenabilities.

$$IIW \text{ CarbonEquivalent (CE)} = C + \frac{Mn + Si}{6} + \frac{Ni + Cu}{15} + \frac{Cr + Mo + V}{5}$$

Sample	F292	F326	F327	F328	F329	F330
IIW CE	0.750	0.724	0.718	0.738	0.827	0.717

Table 4-2. Areas Under the Impact Energy Curves (N•m•°C) by Trapezoidal Rule.

Sample	F292	F326	F327	F328	F329	F330
Impact Area	10947.3	10305.1	9406.4	11894.9	8742.6	11631.7

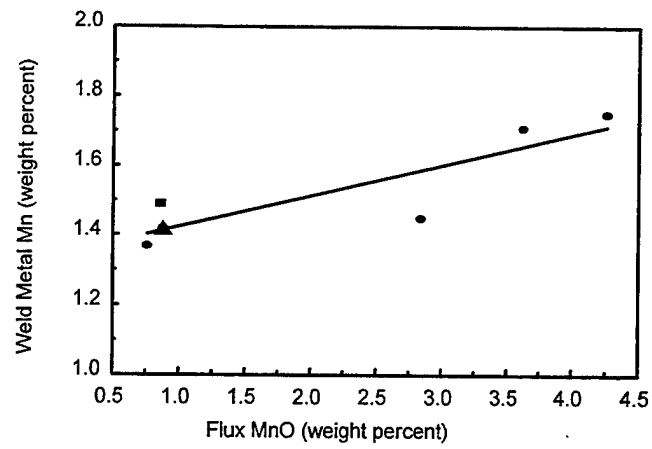


Figure 4-1. Weld Metal Mn vs. Flux MnO.
Corr. = 0.872 (all points)

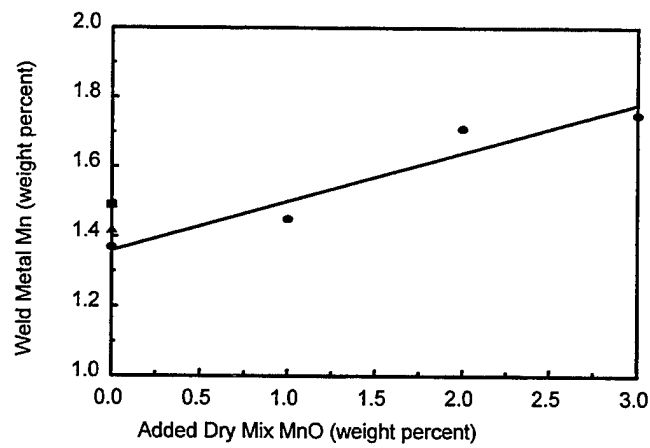


Figure 4-2. Weld Metal Mn vs. Added MnO.
Corr. = 0.9597 (MnO Series)

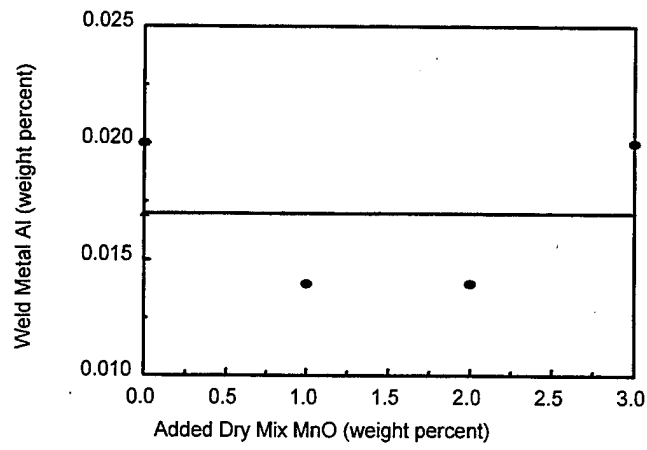


Figure 4-3. Weld Metal Al vs. Added MnO.
Corr. = 0.0 (MnO series)

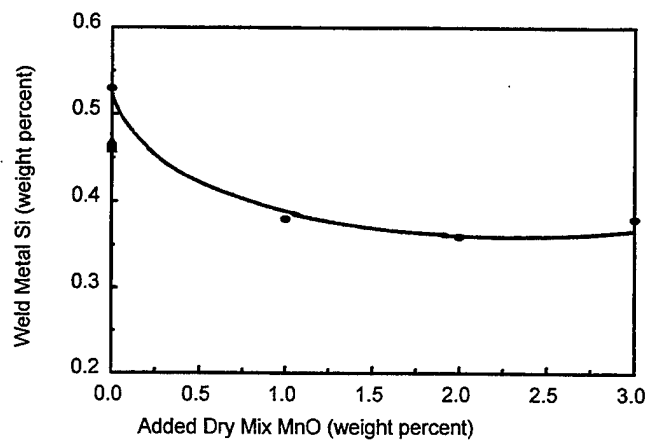


Figure 4-4. Weld Metal Si vs. Added MnO.

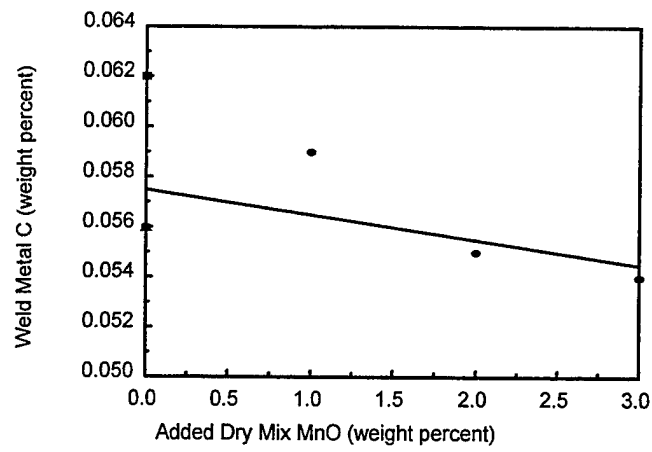


Figure 4-5. Weld Metal C vs. Added MnO.
Corr. = -0.5976 (MnO series)

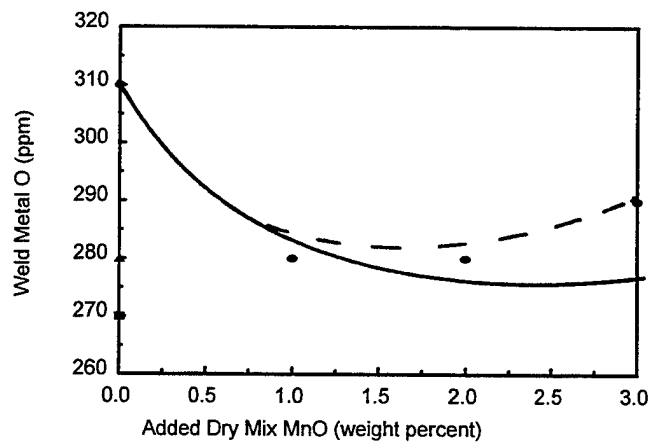


Figure 4-6. Weld Metal O vs. Added MnO.

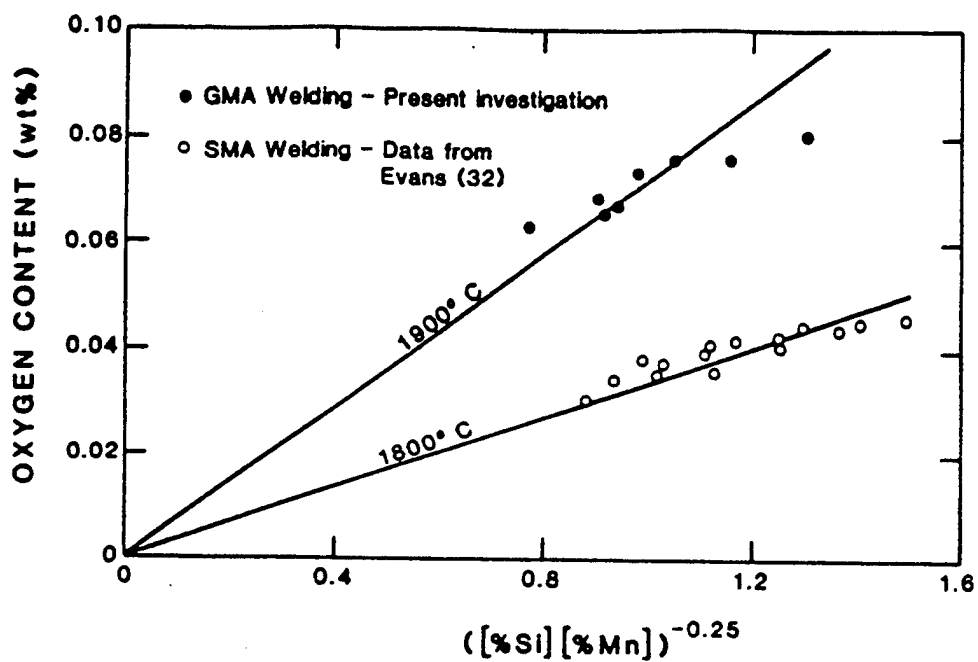


Figure 4-7. Grong's Plot of Oxygen Content vs. Deoxidation Parameter. Solid Lines Represent Thermodynamic Calculations at the Indicated Temperatures [From Ref. 17].

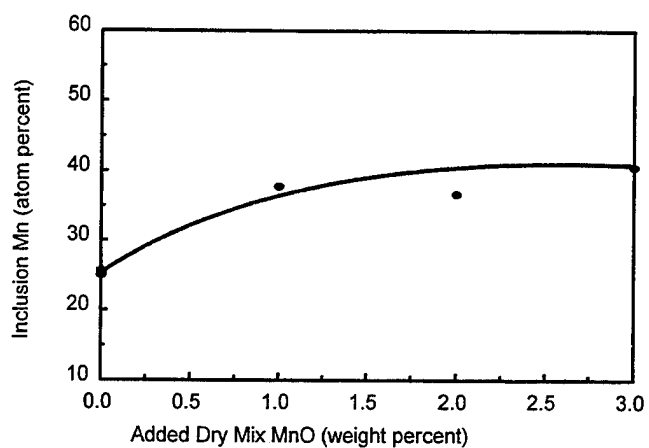


Figure 4-8. Inclusion Mn vs. Added MnO.
Corr. = 0.8591 (MnO series)

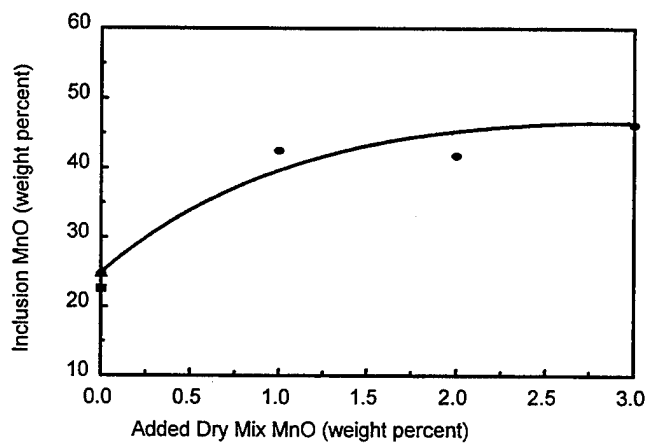


Figure 4-9. Inclusion MnO vs. Added MnO.
Corr. = 0.8580 (MnO series)

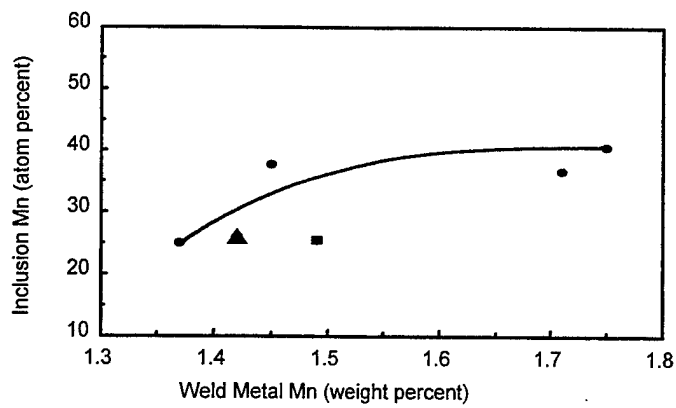


Figure 4-10. Inclusion Mn vs. Weld Mn.

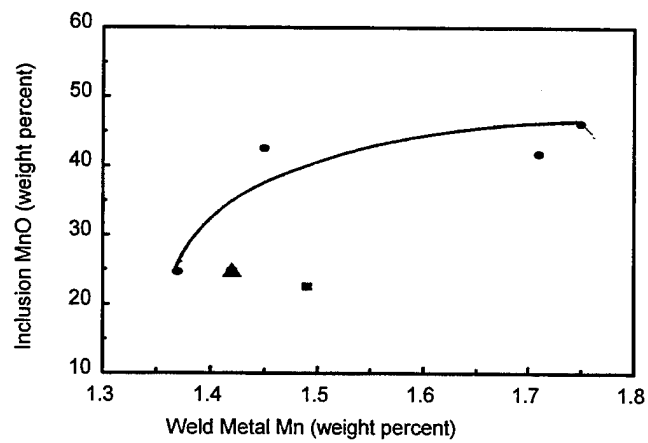


Figure 4-11. Inclusion MnO vs. Weld Mn.

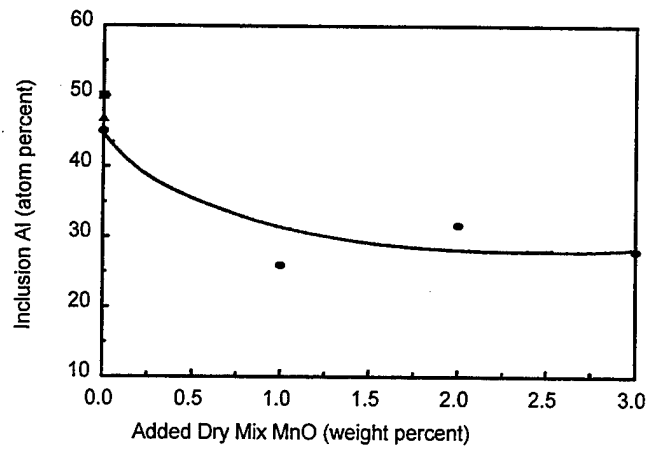


Figure 4-12. Inclusion Al vs. Added MnO.

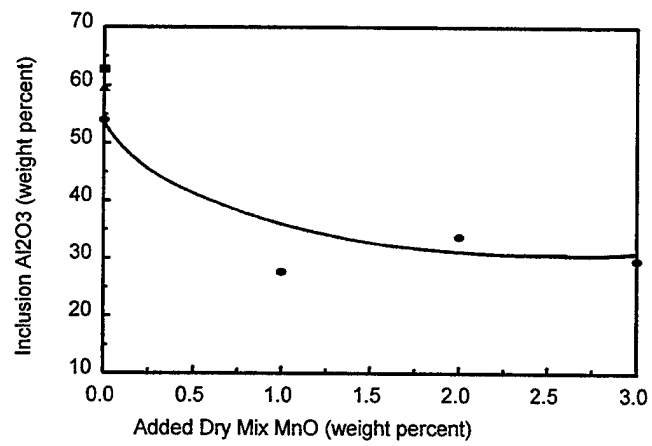


Figure 4-13. Inclusion Al₂O₃ vs. Added MnO.

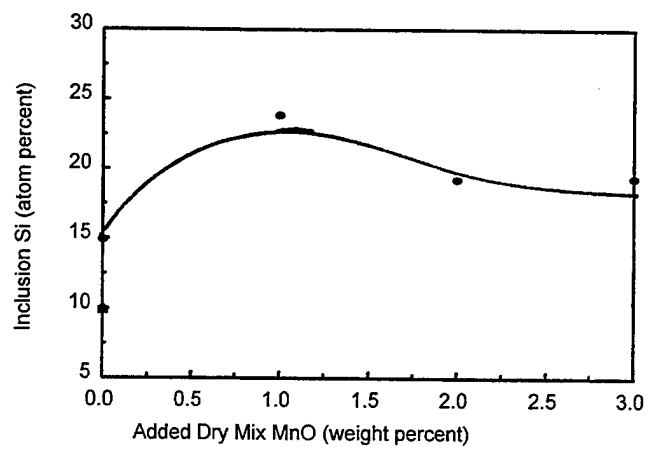


Figure 4-14. Inclusion Si vs. Added MnO.

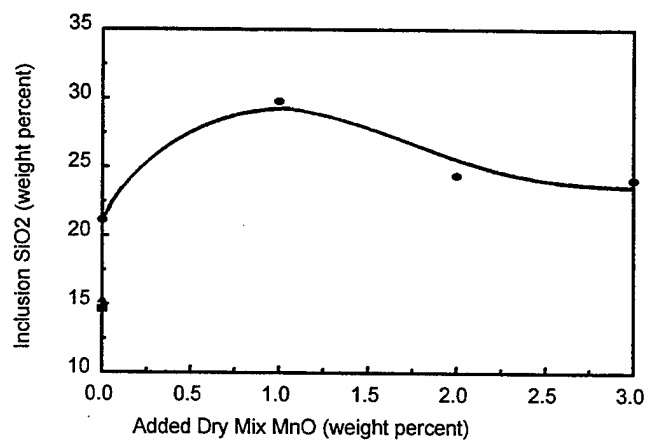


Figure 4-15. Inclusion SiO₂ vs. Added MnO.

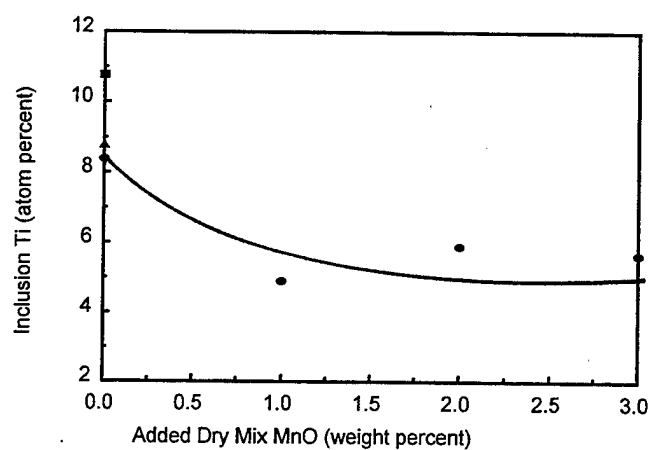


Figure 4-16. Inclusion Ti vs. Added MnO.

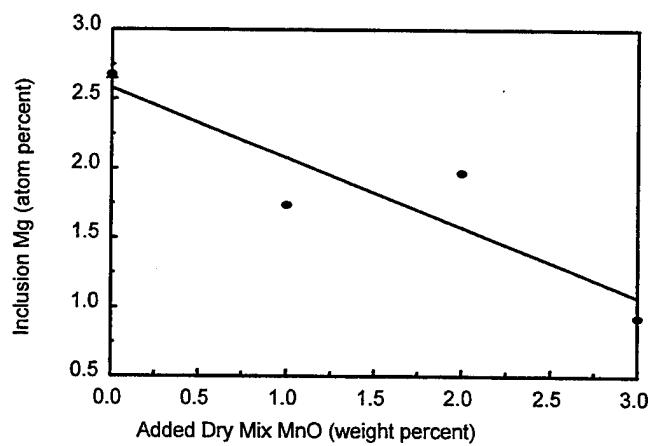


Figure 4-17. Inclusion Mg vs. Added MnO.
Corr. = -0.8987 (MnO series)

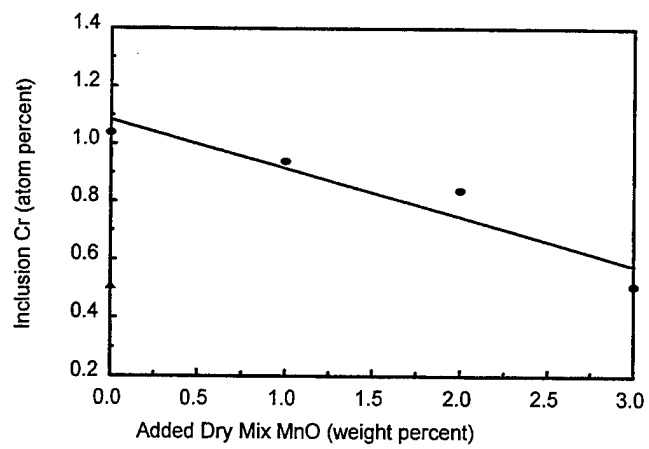


Figure 4-18. Inclusion Cr vs. Added MnO.
Corr. = -0.9487 (MnO series)

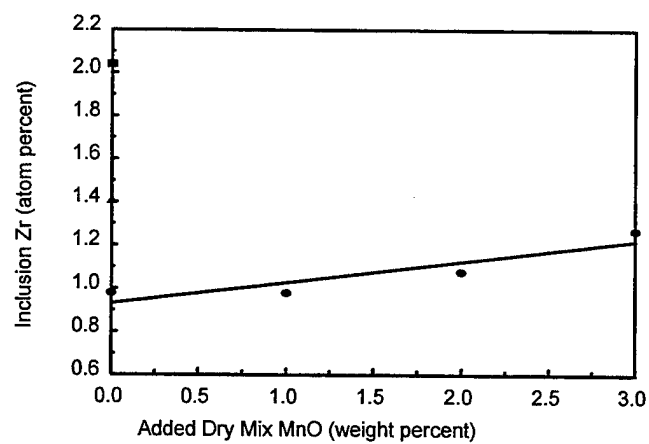


Figure 4-19. Inclusion Zr vs. Added MnO.
Corr. = 0.9160 (MnO series)

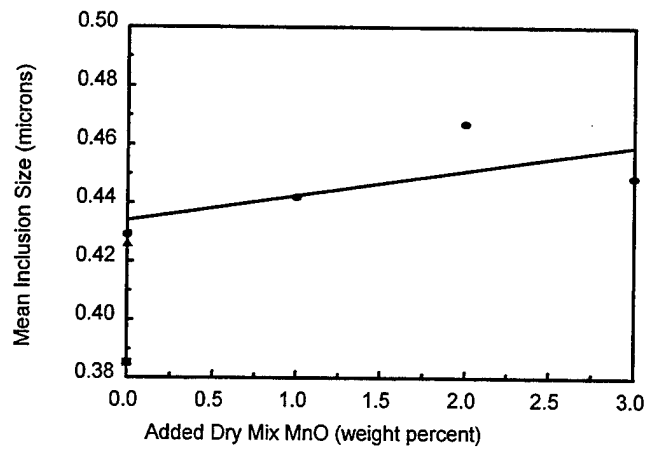


Figure 4-20. Inclusion Size vs. Added MnO.
Corr. = 0.6885 (MnO series)

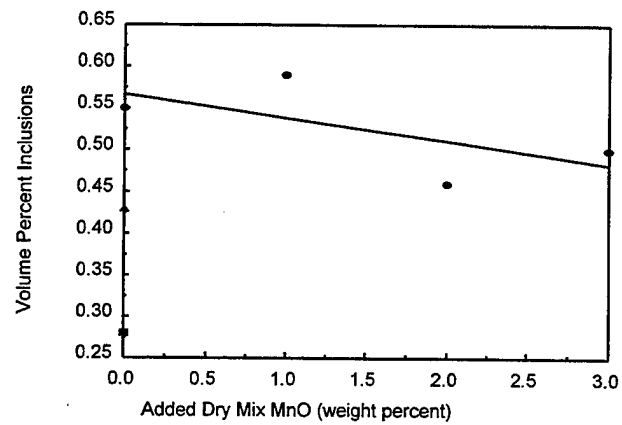


Figure 4-21. Inclusion Volume Percent vs. Added MnO.
Corr. = -0.6357 (MnO series)

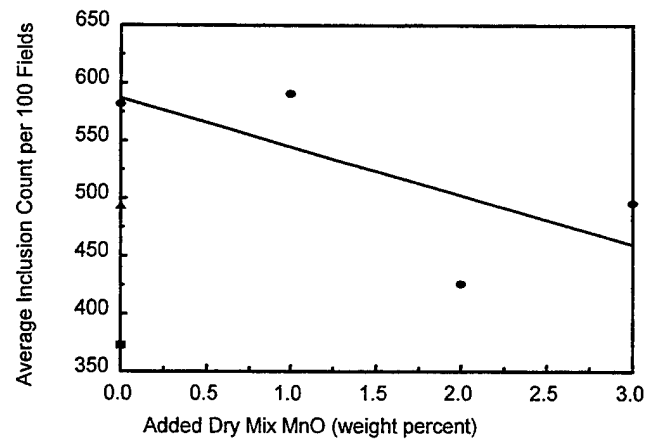


Figure 4-22. Inclusion Count vs. Added MnO.
Corr. = -0.7003 (MnO series)

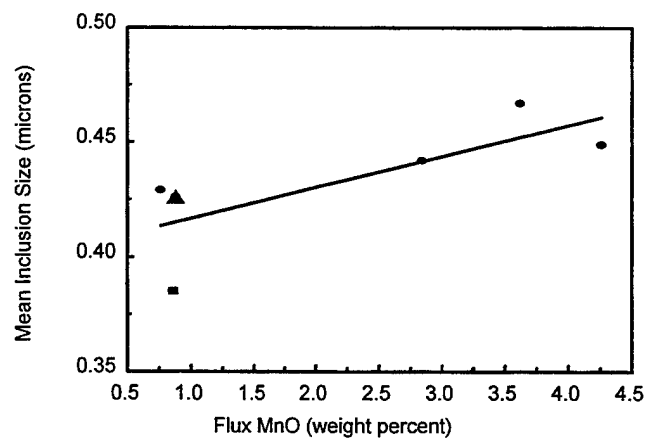


Figure 4-23. Inclusion Size vs. Flux MnO.
Corr. = 0.7622 (all points)

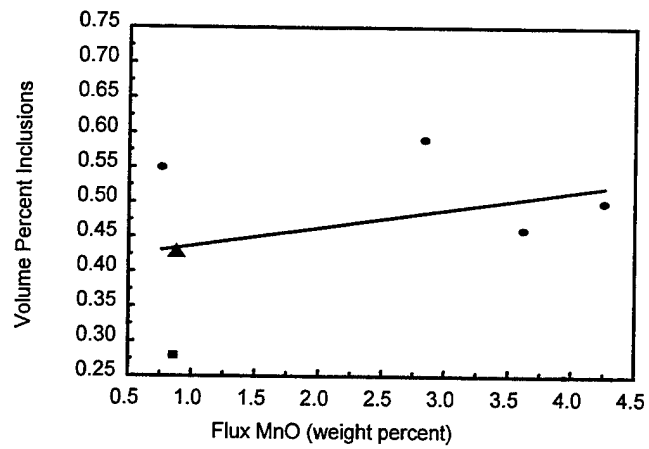


Figure 4-24. Volume Percent Inclusions vs. Flux MnO.
Corr. = 0.3704 (all points)

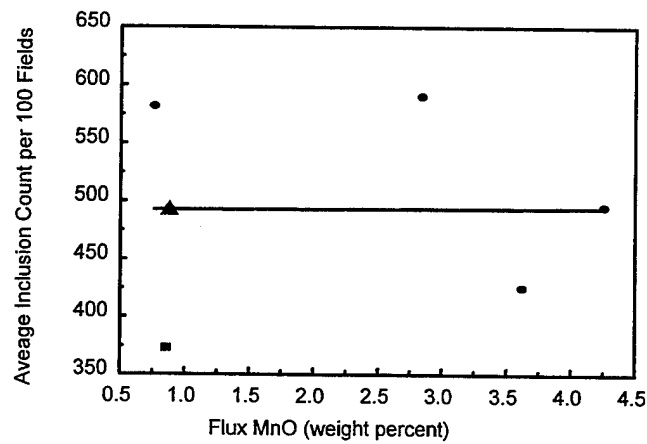


Figure 4-25. Inclusion Count vs. Flux MnO.
Corr. = -0.0075 (all points)

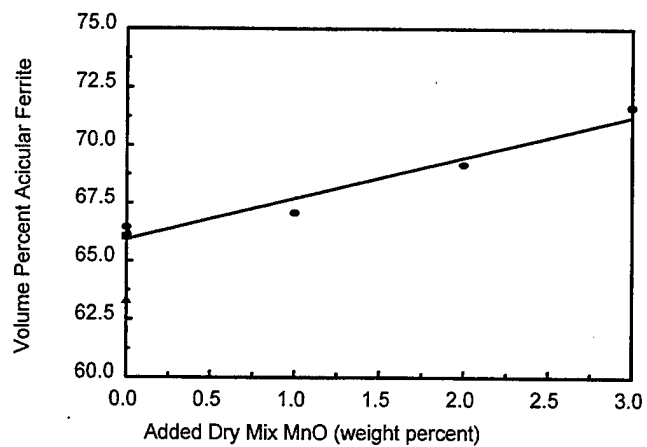


Figure 4-26. Weld Acicular Ferrite vs. Added MnO.
Corr. = 0.9714 (MnO series)

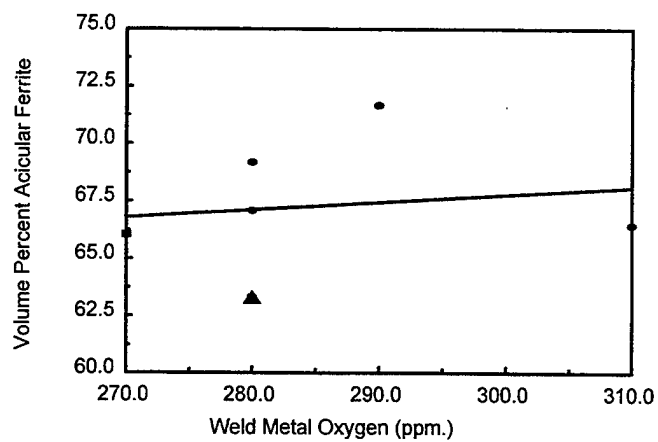


Figure 4-27. Weld Acicular Ferrite vs. Weld Metal O₂.
Corr. = 0.1594

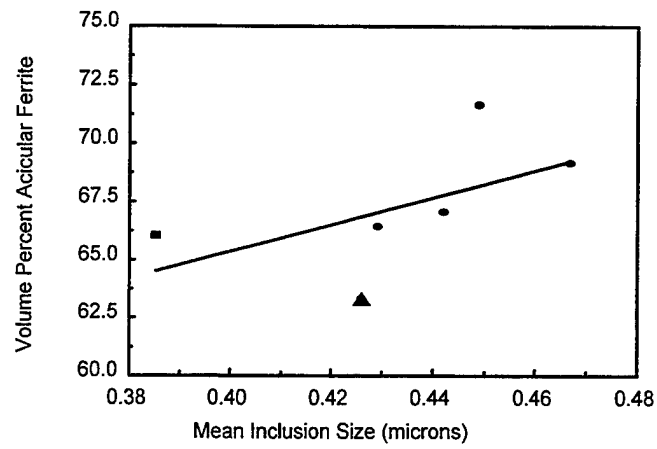


Figure 4-28. Weld Acicular Ferrite vs. Inclusion Size.
Corr. = 0.5614 (all points)

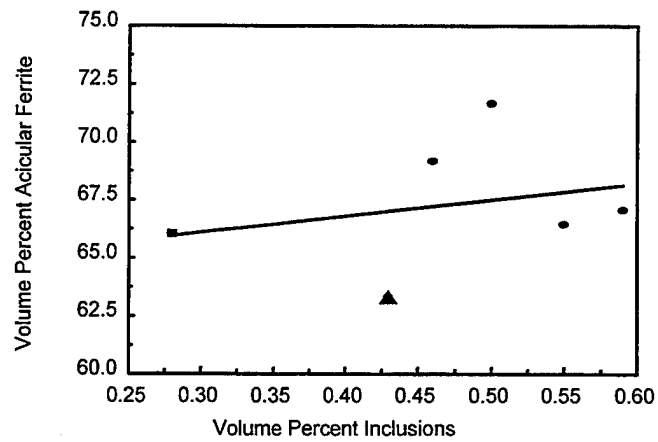


Figure 4-29. Weld Acicular Ferrite vs. Volume Percent Inclusions.
Corr. = 0.2860

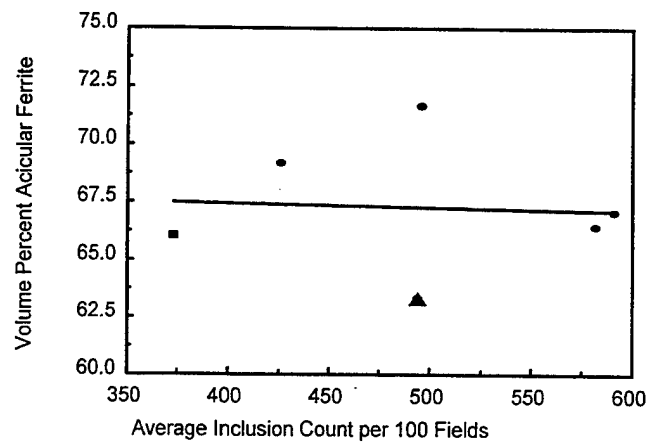


Figure 4-30. Weld Acicular Ferrite vs. Inclusion Count.
Corr. = -0.0503

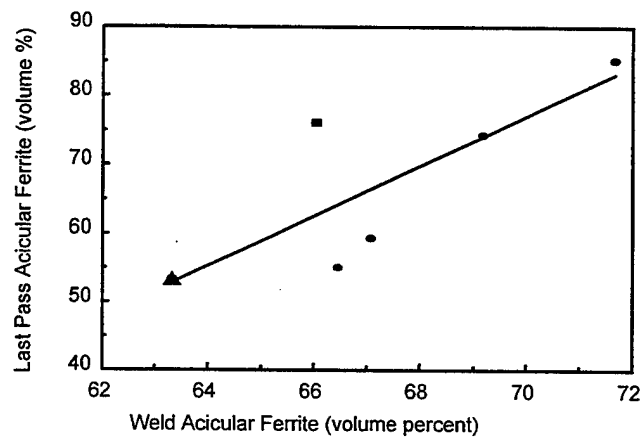


Figure 4-31. Last Pass Acicular Ferrite vs. Weld Acicular Ferrite.
Corr. = 0.7929 (all points)

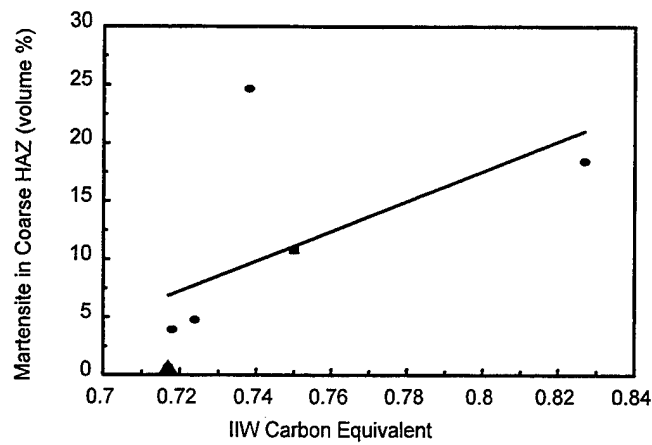


Figure 4-32. Martensite in Coarse HAZ vs. Hardenability.
Corr. = 0.5769 (all points)

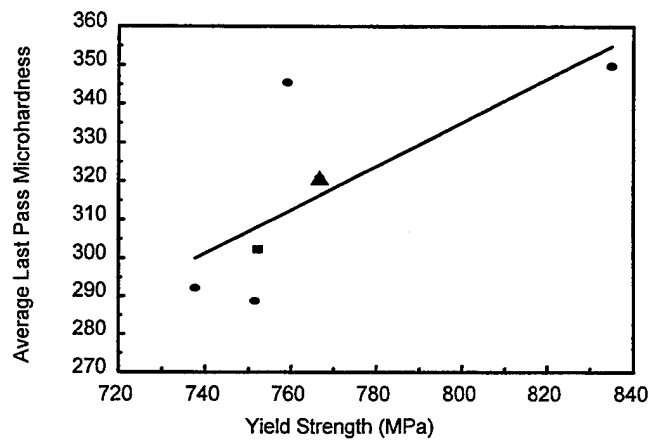


Figure 4-33. Last Pass Hardness vs. Yield Strength.
Corr. = 0.7355 (all points)

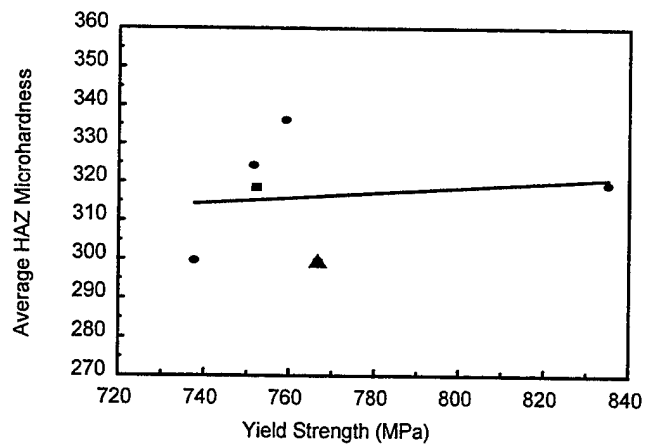


Figure 4-34. Coarse HAZ Hardness vs. Yield Strength.
Corr. = 0.1572 (all points)

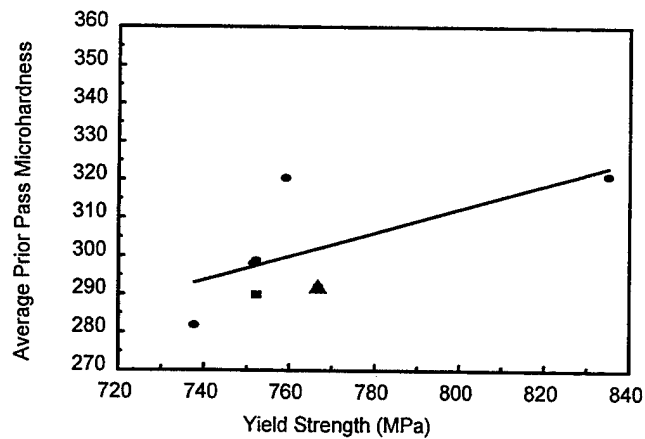


Figure 4-35. Prior Pass Hardness vs. Yield Strength.
Corr. = 0.6832 (all points)

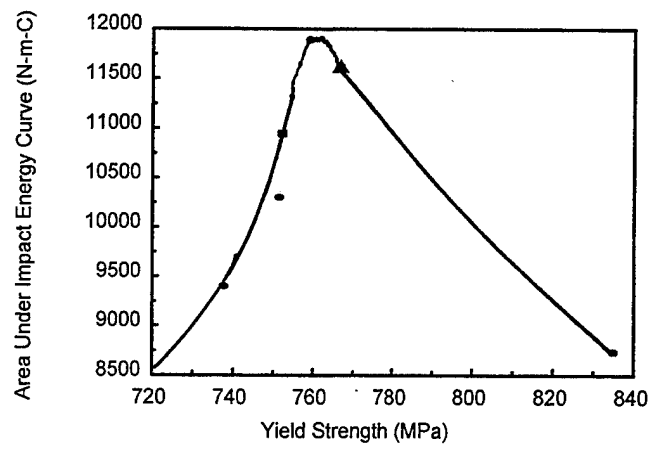


Figure 4-36. Impact Area vs. Yield Strength.

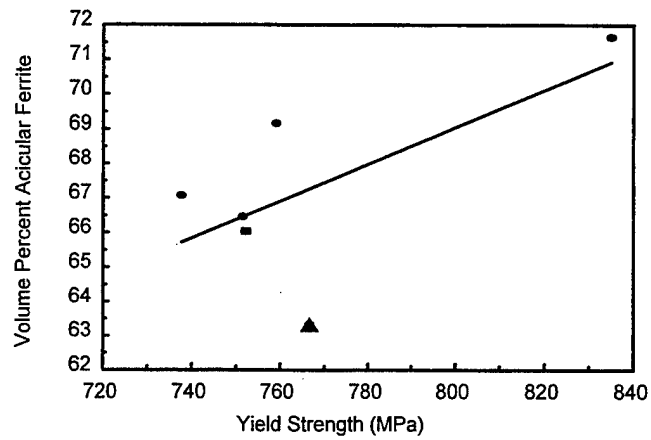


Figure 4-37. Weld Acicular Ferrite vs. Yield Strength.
Corr. = 0.6508 (all points)

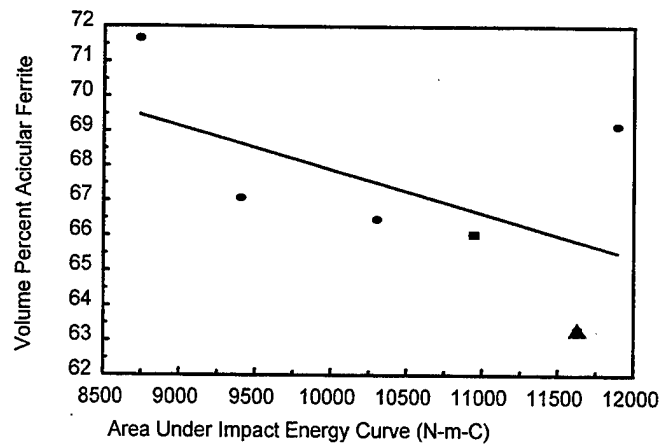


Figure 4-38. Weld Acicular Ferrite vs. Impact Area.
Corr. = -0.5476 (all points)

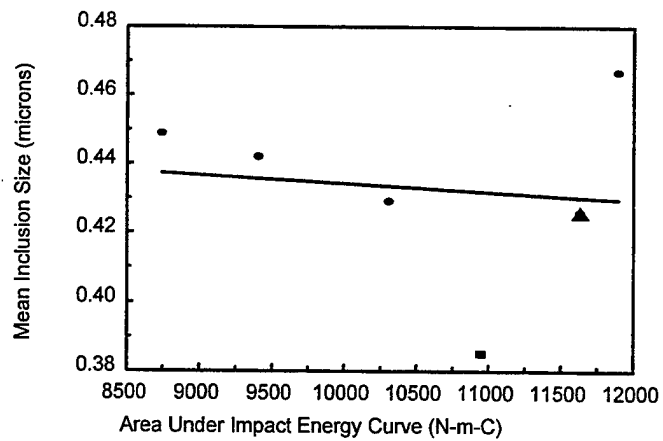


Figure 4-39. Inclusion Size vs. Impact Area.
Corr. = -0.1097 (all points)

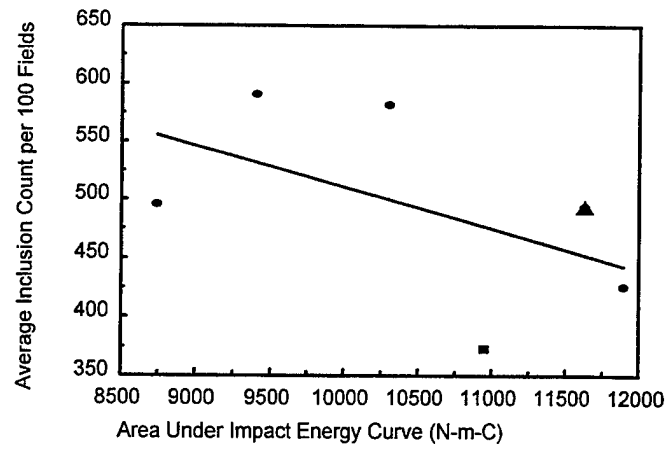


Figure 4-40. Inclusion Count vs. Impact Area.
Corr. = -0.5191 (all points)

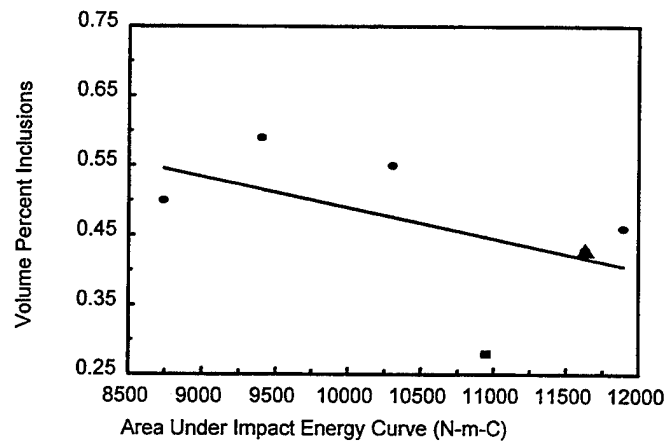


Figure 4-41. Volume Percent Inclusions vs. Impact Area.
Corr. = -0.5065 (all points)

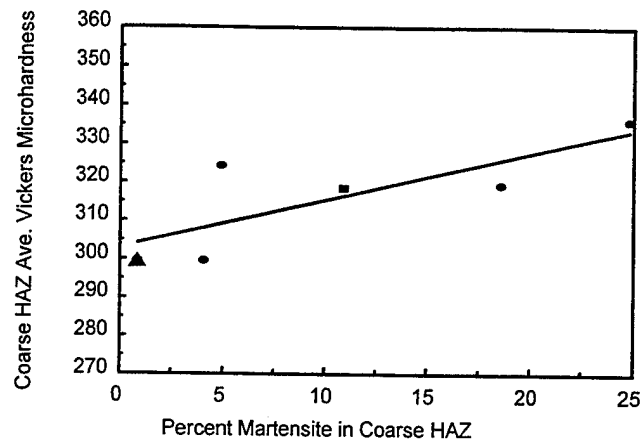


Figure 4-42. Average Microhardness vs. Martensite in Coarse HAZ.
Corr. = 0.7970 (all points)

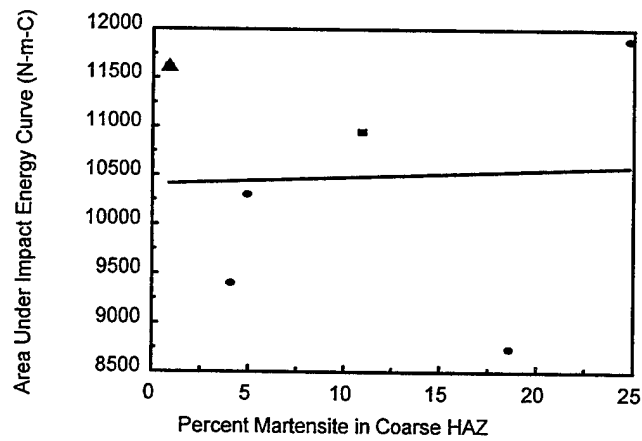


Figure 4-43. Impact Area vs. Martensite in Coarse HAZ.
Corr. = 0.0537 (all points)

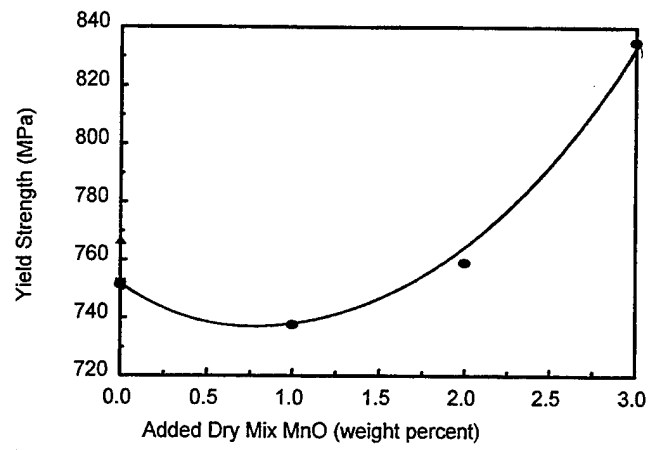


Figure 4-44. Yield Strength vs. Added MnO.

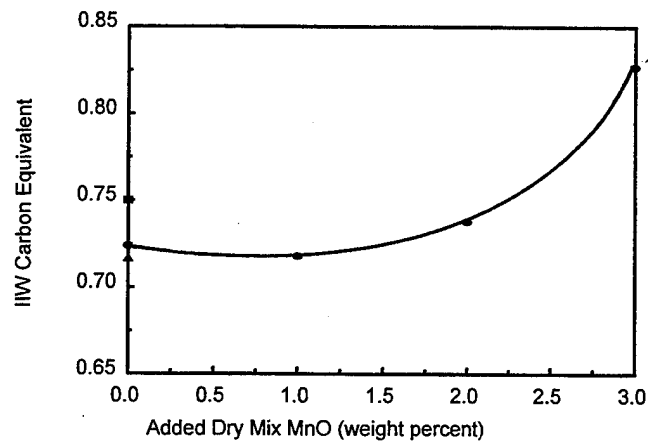


Figure 4-45. Hardenability vs. Added MnO.

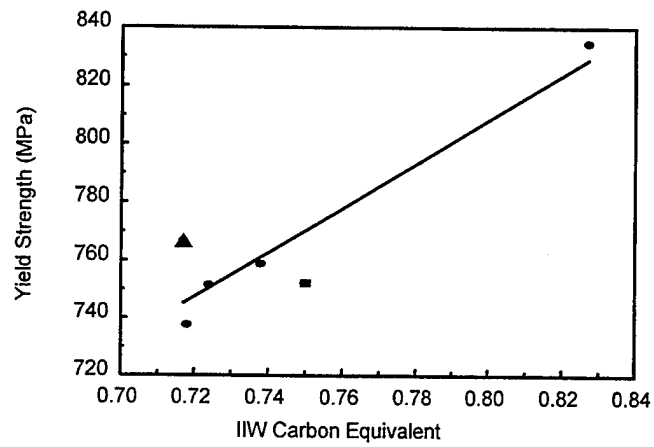


Figure 4-46. Yield Strength vs. Hardenability.
 Corr. = 0.9219 (all points)
 Corr. = 0.9967 (MnO series)

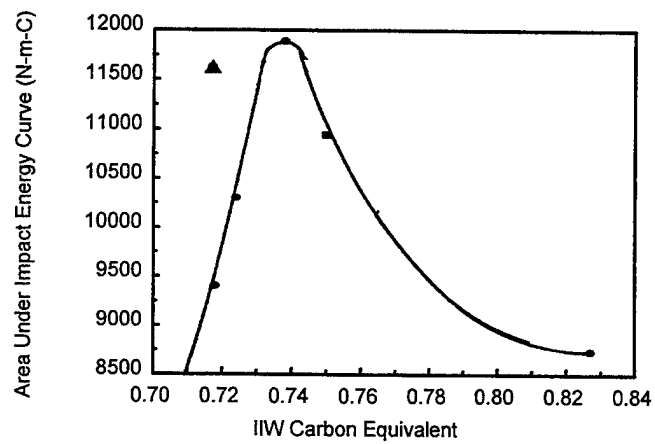


Figure 4-47. Impact Area vs. Hardenability.

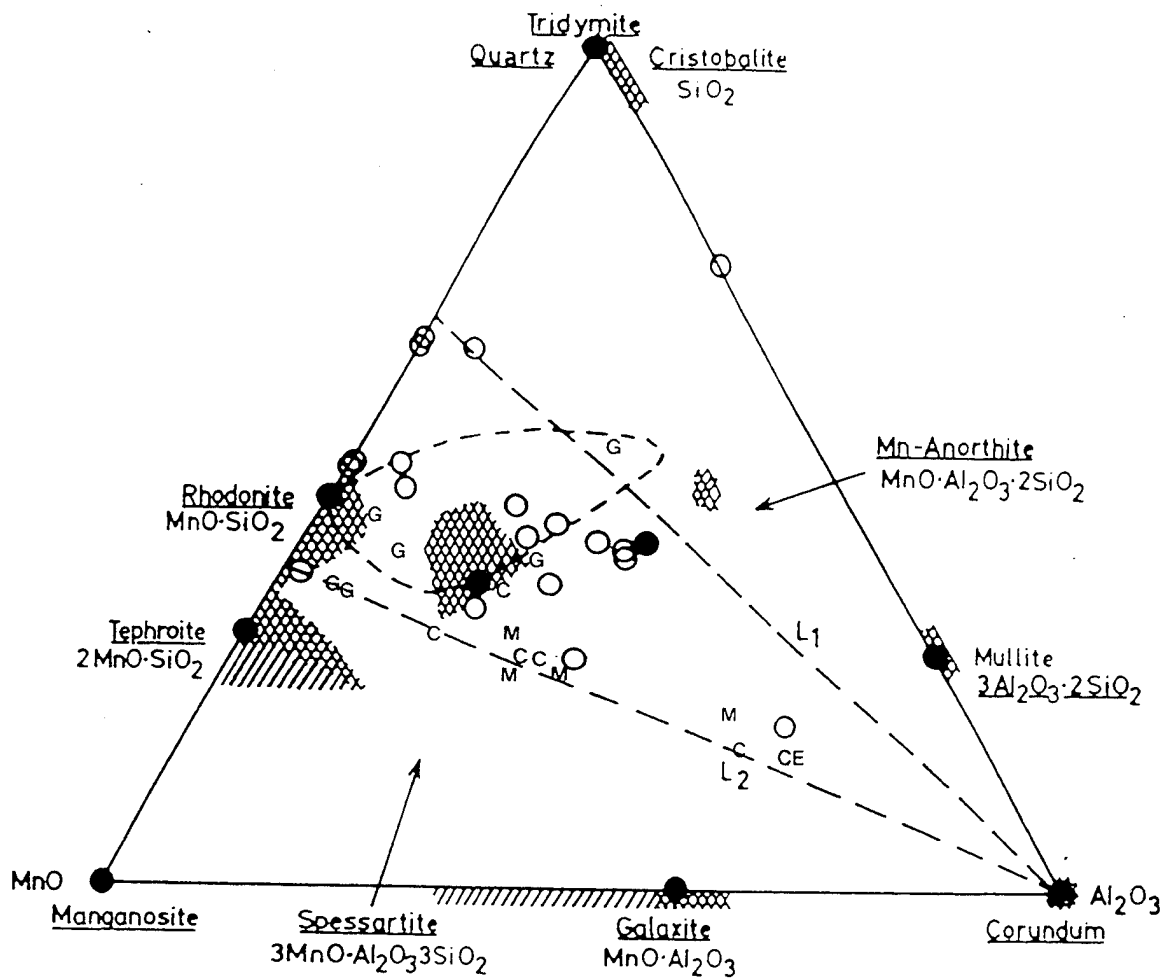


Figure 4-48. Position on Ternary Phase Diagram For Inclusions Analyzed at NPS.
Assumes All S in MnS and all Ti in $\text{MnO} \cdot \text{TiO}_2$ [After Ref. 49].

O = Ref. 49

M = MnO Series (F326-F329)

CE = CeO_2 (F330)

C = Commercial Flux Series [Ref. 3]

G = GMAW Series [Ref. 3]

V. SUMMARY

A. CONCLUSIONS

Performing an experiment in which only the manganese oxide content of the submerged arc welding flux used for HY-100 welds was changed resulted in the determination that the final stage of deoxidation in these welds is probably accomplished by the formation of a manganese silicate, possibly rhodonite or theproite. In either case, the manganese silicate formation dilutes the content of the previously formed oxides in the inclusions. After the deoxidation is complete, phase changes may occur both prior to or after inclusion solidification, making the actual phase of the deoxidation product both undeterminable and irrelevant, though the phase present at the inclusion surface during cooling through the bainite region of the CCT curve may be very important. The nature of the analysis performed led to no information supporting one proposed mechanism of acicular ferrite formation over another.

In the case of these welds, the mechanical properties were largely determined by the weld metal chemistry, which resulted in the microstructures and extent of the fully reaustenitized weld metal to differ vastly. The controlling feature for toughness appeared to be minimization of the bainite content in this portion of the weld, with the high strength of the 3% MnO weld, F329, making it run counter to this observation. The 2% MnO sample, F328, and the commercial flux experiment sample, F292, had a low bainite content because

some fine, possibly tempered martensite formed preferentially. The 0.5% cerium oxide sample, F330, apparently minimized bainite formation by the lowering of austenite grain boundary energy by the cerium, which resulted in the preferential formation of acicular ferrite. In all cases, more analysis is required, perhaps including fractography, to make a final determination. It must be noted again, that the large influence of hardenability on the mechanical properties of these welds is at least partially a reflection of the similar content of acicular ferrite in all of them. The base flux and welding parameters were chosen to result in a high acicular ferrite content, which was indeed achieved. Therefore, the differences in these welds was, by the nature of the experiment, something else. The something else was the manganese and silicon contents, and hence the hardenability.

B. RECOMMENDATIONS

The determination of the phases present in the inclusions of these welds remains one of the pressing issues in determining the mechanism of acicular ferrite formation, and as such must be pursued. Use of a TEM with higher accelerating potential and smaller beam size should improve the electron diffraction results. More consistent and reliable inclusion statistics can probably be obtained either by using carbon extractions to measure the size and number of inclusions in a selected area, or by using SEM image analysis equipment. Use of the CRT on this SEM in conjunction with the cursor is not recommended due to its low resolution and the resulting inability to identify small ($<0.25\text{ }\mu\text{m.}$) inclusions. In future joint

experiments between NSWC and NPS, broken tensile test and Charpy specimens should be provided to NPS in addition to weld samples. This would allow the investigation of fracture mechanisms, which should improve the ability to diagnose the microstructural features that control the mechanical properties.

It is not recommended that Oerlikon be urged to increase the MnO content of their OP121TT flux. The commercial flux experiment showed that the chemical variation from lot to lot could just as likely result in overshooting the desired MnO content as achieving it. Instead, flux manufacturers should be urged to investigate the cost of preparing fluxes from commercial or reagent grade chemicals, particularly for applications where acceptance testing results in a high proportion of failed welds. Use of individual chemicals should result in less variability between lots, and could eventually result in reduced acceptance testing and lower production costs. Lower production costs could result in consumers, like the Navy, being willing to pay more for the product itself. After all, it is lower welding costs which have resulted in the Navy abandoning the HY steels for the initially more expensive HSLA steels in future construction.

LIST OF REFERENCES

1. Kettell K.W., *Correlation of Flux Composition and Inclusion Characteristics With Submerged Arc Weld Metal Properties in HY-100 Steel*, Masters Thesis, Naval Postgraduate School, Monterey, CA., 1993.
2. Brothers D.G., *The Origin of Acicular Ferrite in Gas Metal Arc and Submerged Arc Welds*, Masters Thesis, Naval Postgraduate School, Monterey, CA., 1994.
3. Eakes M.W., *Correlation of Inclusion Size and Chemistry With Weld Metal Composition And Microstructure in Arc Weldments of High Strength Steels*, Masters Thesis, Naval Postgraduate School, Monterey, CA., 1994.
4. Fox A.G. and Brothers D.G., "The Role of Titanium in the Non-metallic Inclusions Which Nucleate Acicular Ferrite in the Submerged Arc Weld (SAW) Fusion Zones of Navy HY-100 Steel", pp. 1061-1066, *Scripta Metallurgica et Materialia*, 1995.
5. Fox A.G., Eakes M.W., and Franke, G.L., "The Effect of Small Changes in Flux Basicity on the Acicular Ferrite Content and Mechanical Properties of Submerged Arc Weld Metal of Navy HY-100 Steel", submitted, *Welding Research Supplement to The Welding Journal*, 1995.
6. Holsberg P.W., Gudas J.P., and Caplan, I.L., "Metallurgical Design and Processes in the U.S. Navy High Strength Steel Welding", pp. 593-605, *Proceedings of the 2nd International Conference on Trends in Welding Research*, ASM International, 1989.
7. Flax R.W., Keith R.E., and Randall M.D., "Welding the HY Steels", *ASTM Special Technical Publication 494*, 10 May 1971.
8. Department of the Navy Military Specification MIL-S-16216K(SH), *Steel Plate, Alloy, Structural, High Yield Strength (HY-80 and HY-100)*, 19 June 1987.
9. Kou S., *Welding Metallurgy*, John Wiley and Sons, 1987.
10. Department of the Navy Military Specification MIL-E-23765/2E(SH), *Electrodes and Rods - Welding, Bare, Solid, or Alloy Cored; and Fluxes, Low Alloy Steel*, 22 April 1994.

11. Bhadeshia H.K.D.H., *Bainite in Steels*, The Institute of Metals, 1992.
12. North T.H., Bell H.B., Nowicki A., and Craig I., "Slag/Metal Interaction, Oxygen and Toughness in Submerged Arc Welding", pp. 63s-74s, *Welding Research Supplement to The Welding Journal*, March 1978.
13. Babu S.S., David S.A., Vitek J.M., Mundra K., and Debroy T., "Development of Macro- and Microstructures of Carbon-Manganese Low Alloy Steel Welds: Inclusion Formation", pp. 186-199, *Materials Science and Technology*, 1995.
14. Dowling J.M., Corbett, J.M., and Kerr H.W., "Inclusion Phases and the Nucleation of Acicular Ferrite in Submerged Arc Welds in High Strength Low Alloy Steels", pp. 1611-1623, *Metallurgical Transactions A*, 1986.
15. Palm J.H., "How Fluxes Determine the Metallurgical Properties of Submerged Arc Welds", pp. 358s-360s, *Welding Research Supplement to The Welding Journal*, July 1972.
16. Chai C.S. and Eagar T.W., "Slag-Metal Equilibrium During Submerged Arc Welding", pp. 539-547, *Metallurgical Transactions B*, 1981.
17. Grong O., Siewert T.A., Martins G.P., and Olsen D.L., "A Model for the Silicon-Manganese Deoxidation of Steel Weld Metals", pp. 1797-1807, *Metallurgical Transactions A*, 1986.
18. Bhadeshia H.K.D.H., Svensson L.E., and Gretoft B., "A Model for the Development of Microstructure in Low-Alloy Steel (Fe-Mn-Si-C) Weld Deposits", pp. 1271-1283, *Acta Metallurgica*, 1985.
19. Sugden A.A.B. and Bhadeshia H.K.D.H., "The Nonuniform Distribution of Inclusions in Low-Alloy Steel Weld Deposits", pp. 669-674, *Metallurgical Transactions A*, 1988.
20. Grong O. and Matlock D.K., "Microstructural Development in Mild and Low-Alloy Steel Weld Metals", pp. 30-43, *International Metals Reviews*, v. 31, 1986.
21. Reynolds W.T., Aaronson H.I., and Spanos G., "A Summary of the Present Diffusionist Views on Bainite", pp. 737-746, *Materials Transactions, Japan Institute of Metals*, 1991.

22. Bhadeshia H.K.D.H. and Christian J.W., "Bainite in Steels", pp. 767-797, *Metallurgical Transactions A*, 1990.
23. Bhadeshia H.K.D.H., "Control of Weld Metal Microstructure and Properties", pp. 34-69, *The Metallurgy, Welding, and Qualification of Microalloyed (HSLA) Steel Weldments*, American Welding Society, 1990.
24. Spanos G., Fang H.S., and Aaronson H.I., "A Mechanism for the Formation of Lower Bainite", pp. 1381-1390, *Metallurgical Transactions A*, 1990.
25. Spanos G., "The Fine Structure and Formation Mechanism of Lower Bainite", pp. 1967-1994, *Metallurgical and Materials Transactions A*, 1994.
26. Yang J.R. and Bhadeshia H.K.D.H., "Thermodynamics of the Acicular Ferrite Transformation in Alloy-Steel Weld Deposits", pp. 187-191, *International Conference on Trends in Welding Research*, ASM International, 1989.
27. Strangwood M. and Bhadeshia H.K.D.H., "The Mechanism of Acicular Ferrite Formation in Steel Weld Deposits", pp. 209-213, *International Conference on Trends in Welding Research*, ASM International, 1989.
28. Yang J.R. and Bhadeshia H.K.D.H., "Orientation Relationships Between Adjacent Plates of Acicular Ferrite in Steel Weld Deposits", pp. 93-97, *Materials Science and Technology*, 1989.
29. Ricks R.A., Howell P.R., and Barritte G.S., "The Nature of Acicular Ferrite in HSLA Steel Weld Metals", pp. 732-740, *Journal of Materials Science*, 1982.
30. Babu S.S. and Bhadeshia H.K.D.H., "Stress and the Acicular Ferrite Transformation", pp. 1-9, *Materials Science and Engineering*, 1992.
31. Callister W.D., *Materials Science and Engineering: an Introduction*, John Wiley and Sons, 1991.
32. Harrison P.L. and Farrar R.A. "Applications of Continuous Cooling Transformation Diagrams for Welding of Steels", pp. 35-51, *International Metals Reviews*, v. 34, 1989.

33. Babu S.S. and Bhadeshia H.K.D.H., "Mechanism of the Transition from Bainite to Acicular Ferrite", pp. 679-688, *Materials Transactions, Japan Institute of Metals*, 1991.
34. Grong O., Kluken A.O., Nylund H.K., Dons A.L., and Hjelen J., "Catalyst Effects in Heterogeneous Nucleation of Acicular Ferrite", pp. 525-534, *Metallurgical and Materials Transactions A*, 1995.
35. Gregg J.M. and Bhadeshia H.K.D.H., "Titanium Rich Phases and the Nucleation of Bainite", pp. 1603-1611, *Metallurgical and Materials Transactions A*, 1994.
36. Gregg J.M. and Bhadeshia H.K.D.H., "Bainite Nucleation From Mineral Surfaces", pp. 3321-3330, *Acta Metallurgica et Materialia*, 1994.
37. Reed R.C. and Bhadeshia H.K.D.H., "A Simple Model for Multipass Steel Welds", pp. 3663-3678, *Acta Metallurgica et Materialia*, 1994.
38. Gibson H., *Influence of Shielding Gas Composition on Alloy Recovery During Gas Metal Arc Welding*, Masters Thesis, Massachusetts Institute of Technology, Cambridge, MA, 1993.
39. Widgery D.J., "Deoxidation Practice for Mild Steel Weld Metal", pp. 57s-65s, *Welding Research Supplement to the Welding Journal*, March 1976.
40. Hilliard J.E. and Cahn J.W., "An Evaluation of Procedures in Quantitative Metallography for Volume-Fraction Analysis", pp. 344-352, *Transactions of the Metallurgical Society of the AIME*, 1961.
41. ASTM Standard E 562 - 89, "Standard Test Method for Determining Volume Fraction by Systematic Manual Point Count", *Annual Book of ASTM Standards*, 1995.
42. Gladman T. and Woodhead J.H., "The Accuracy of Point Counting in Metallographic Investigations", pp. 189-193, *Journal of the Iron and Steel Institute*, February, 1960.
43. Lee J.L., "Evaluation of the Nucleation Potential of Intragranular Acicular Ferrite in Steel Weldments", pp. 3291-3298, *Acta Metallurgica et Materialia*, 1994.

44. Klucken A.O., Grong O., and Hjelen J., "SEM Based Automatic Image Analysis of Non-metallic Inclusions in Steel Weld Metals", pp. 649-654, *Materials Science and Technology*, 1988.
45. Bhadeshia H.K.D.H., and Svensson L.E., "The Microstructure of Submerged Arc-Weld Deposits for High Strength Steels", pp. 3180-3188, *Journal of Materials Science*, 1989.
46. Babu S.S. and Bhadeshia H.K.D.H., "Transition From Bainite to Acicular Ferrite in Reheated Fe-Cr-C Weld Deposits", pp. 1005-1020, *Materials Science and Technology*, 1990.
47. Fox A.G., Eakes M.W., and Wong R., "The Effect of Gas Composition on the Microstructure and Mechanical Properties of Gas-Metal-Arc Weld Metal of Navy HSLA-100 Steel", submitted, *Welding Research Supplement to The Welding Journal*, 1995.
48. Grong O., Siewert T.A., and Edwards G.R., "Effects of Deoxidation Practice on the Transformation Behavior and Toughness of Steel Welds", pp. 279s-288s, *Welding Research Supplement to The Welding Journal*, November 1986.
49. Kiessling R. and Lange N., *Non-metallic Inclusions in Steel*, The Metals Society, 1978.

INITIAL DISTRIBUTION LIST

		No. Copies
1.	Defense Technical Information Center 8725 John J. Kingman Rd., STE 0944 Ft. Belvoir, Virginia 22060-6218	2
2.	Library, Code 13 Naval Postgraduate School Monterey, California 93943-5101	2
3.	Naval Engineering Curricular Office, Code 34 Naval Postgraduate School Monterey, California 93940-5000	1
4.	Department Chairman, Code ME Department of Mechanical Engineering Naval Postgraduate School Monterey, California 93940-5000	1
5.	Dr. Alan Fox, Code ME/FX Department of Mechanical Engineering Naval Postgraduate School Monterey, California 93940-5000	2
6.	Mr. Gene Franke Naval Surface Warfare Center Carderock Division, Annapolis Detachment Code 615, 3A Leggett Circle Annapolis, Maryland 21402-5067	1
7.	Mr. Ivan Caplan Naval Surface Warfare Center Carderock Division, Annapolis Detachment Code 615, 3A Leggett Circle Annapolis, Maryland 21402-5067	1

8. Allen L. Clark
4901 Ferguson Valley Road
McVeytown, Pennsylvania 17051-9708

2